

**Discovery and Characterization of a new Higgs particle using
four-lepton events from the CMS experiment**

by

Christopher B. Martin

A dissertation submitted to The Johns Hopkins University in conformity with the
requirements for the degree of Doctor of Philosophy.

Baltimore, Maryland

July, 2015

© Christopher B. Martin 2015

All Rights Reserved

Abstract

A new particle decaying to a pair of vector bosons was discovered in 2012 by the ATLAS and CMS experiments at the Large Hadron Collider. In the wake of this discovery a rush of measurements was made to characterize this particle. The four-lepton final state has been instrumental in both the discovery and characterization of this new particle. With only about 20 events seen in the resonance peak at 125 GeV the CMS experiment has been able to make considerable progress in characterizing the Higgs-like boson using the wealth of information in this final state in concert with other decay modes. In addition to the search for this new boson we present three recent results in the study of the Higgs-like boson properties: studies of the production mode, total width, and spin-parity quantum numbers.

First we present the search for this new resonance using the $H \rightarrow ZZ \rightarrow 4\ell$ decay channel. Then we discuss the production mode measurement using this final state. Next, we present two results that provided breakthroughs in the study of the Higgs-like resonance. One is the measurement of the width from an interplay between the off-shell and on-shell production, setting a limit three orders of magnitude tighter

ABSTRACT

than previous limits. The other is the tensor structure measurement of the bosons interactions with pairs of vector bosons, leading to constraints on its spin-parity properties, where only limited measurements had been done before. All of these results provide further confirmation that CMS has discovered a Higgs boson near 125 GeV.

Primary Reader: Andrei Gritsan

Secondary Reader:

Acknowledgements

THANKS TO

Contents

Abstract	ii
Acknowledgements	iv
List of Tables	ix
List of Figures	xi
1 Introduction	1
1.1 Symmetries in Physics	2
1.1.1 Noether's Theorem	2
1.1.2 Angular Momentum and the Rotation Group	3
1.1.3 Inherent Spin and SU(2)	5
1.2 Scattering Amplitudes	7
1.2.1 Scattering Matrix	7
1.2.2 Amplitudes and Feynman Diagrams	8
1.3 The Standard Model	12

CONTENTS

1.3.1	Matter	14
1.3.1.1	Quarks	14
1.3.1.2	Leptons	16
1.3.2	Forces	17
1.3.3	Electroweak Symmetry Breaking	21
1.3.3.1	Implications of the Higgs field: Fermion Masses . . .	29
1.4	Limitations of the SM: Higgs boson as a tool	30
1.4.1	CP -violation: The Matter-Antimatter Asymmetry	31
1.4.2	The Graviton: An Unexplained Force	33
1.4.3	Beyond the SM: The Dark Matter, Hierarchy & Fermion Problems	34
2	The Experiment: LHC and CMS	36
2.1	The Large Hadron Collider (LHC)	37
2.2	The Compact Muon Solenoid (CMS)	42
2.2.1	The Magnet	46
2.2.2	The Inner Tracker System	49
2.2.2.1	Pixel Tracker	49
2.2.2.2	Strip Tracker	52
2.2.3	Electromagnetic Calorimeter	55
2.2.4	Hadronic Calorimeter	57
2.2.5	Muon System	60
2.3	Triggering and Particle Reconstruction	65

CONTENTS

2.3.1	CMS Trigger	66
2.3.2	Particle Flow	67
2.3.3	Electrons	68
2.3.4	Muons	73
2.3.5	Jets	75
2.4	CMS Tracker Alignment	76
2.4.1	Silicon Pixel Alignment in Prompt Calibration Loop	80
3	Higgs boson at the LHC: Phenomenology	83
3.1	Higgs boson production at LHC	84
3.2	Higgs boson decay to $ZZ \rightarrow 4\ell$	88
3.3	Higgs boson width: off resonance production and decay	92
3.4	Spin and Parity of a Single-Produced Resonance	99
3.4.1	Decay of a spin-zero resonance	100
3.4.2	Decay of a spin-one resonance	102
3.4.3	Decay of a spin-two resonance	104
4	$H \rightarrow ZZ \rightarrow 4\ell$ search & Production/Decay Fractions	107
4.1	General overview of $H \rightarrow ZZ \rightarrow 4l$	108
4.2	Object Selection	109
4.3	Event Selection, Simulation, & Categorization	112
4.3.1	Simulated Data Samples	112

CONTENTS

4.3.2	Selection & Categorization	113
4.3.3	Background estimation	115
4.4	Kinematic Distributions	119
4.4.1	4ℓ mass spectrum	120
4.4.2	Matrix Element Likelihood Approach (MELA) kinematic discriminant	122
4.4.3	$p_T^{4\ell}$ and Jet Kinematic Discriminant	129
4.5	Search Results	132
4.5.1	Quantifying the observation	138
4.5.2	Search for additional Higgs bosons	144
4.6	Production & Decay Fraction Results	146
5	Conclusions	149
Bibliography		151
Vita		169

List of Tables

1.1	First generation fermions and their different charges, grouped in left(right)-handed doublets(singlets).	17
1.2	List of Fundamental Forces their relative strengths and ranges.	21
2.1	Parameters of the CMS superconducting solenoid.	47
2.2	Detector types in the silicon strip tracker.	53
3.1	List of spin-two models with the decay couplings of an exotic X particle. The subscripts m (minimal couplings), h (couplings with higher-dimension operators), and b (bulk) distinguish different scenarios. . .	106
4.1	The number of observed candidate events compared to the mean expected background and signal rates for each final state. Uncertainties include statistical and systematic sources. The results are given integrated over the full mass measurement range $m_{4\ell} > 100$ GeV and for 7 and 8 TeV data combined.	119
4.2	The number of observed candidate events compared to the mean expected background and signal rates for each final state. Uncertainties include statistical and systematic sources. The results are integrated over the mass range from 121.5 to 130.5 GeV and for 7 and 8 TeV data combined.	133
4.3	The number of observed candidate events compared to the mean expected background and signal rates for the sum of the three final states for each of the two analysis categories. Uncertainties include statistical and systematic sources. The results are integrated over the mass range from 121.5 to 130.5 GeV and for 7 and 8 TeV data combined. The expected signal yield for a SM Higgs boson with $m_H = 126$ GeV is reported, broken down by the production mechanism.	135

LIST OF TABLES

- 4.4 Effect of systematic uncertainties on the yields of signal ($m_H = 126$ GeV) and background processes for the 8 TeV data set and 0/1-jet category. Uncertainties appearing on the same line are 100% correlated, with two exceptions: those related to the missing higher orders are not correlated, and those from the α_S + PDF (gg) in $t\bar{t}H$ are 100% anti-correlated. Uncertainties for the 7 TeV data set are similar. 137

List of Figures

1.1	Euler angles for three dimensional Cartesian coordinates.	4
1.2	Feynman diagram depicting electron-electron scattering via the electromagnetic interaction.	10
1.3	A comedic example of a complicated Feynman diagram designed to appear similar to a Jayhawk.	11
1.4	A Summary Infographic of The Standard Model.	13
1.5	A 2D illustration of the scalar potential, $V(\Phi)$, when $\mu^2 > 0$. The horizontal axes form the complex plane ϕ_1 vs ϕ_2 , while the vertical axis is $V(\Phi)$	23
1.6	A 1D illustration of the scalar potential, $V(\Phi)$, when $\mu^2 > 0$	24
1.7	A 2D illustration of the scalar potential, $V(\Phi)$, when $\mu^2 < 0$. The horizontal axes form the complex plane ϕ_1 vs ϕ_2 , while the vertical axis is $V(\Phi)$	25
1.8	A 1D illustration of the scalar potential, $V(\Phi)$, when $\mu^2 > 0$	25
1.9	A 2D illustration of oscillations in the the scalar potential, $V(\Phi)$, parameterized by χ and ψ	28
2.1	A cross section schematic of the LHC Dipole magnet showing the two center beam pipes, superconducting coils (red), and other supporting structures.	38
2.2	The peak luminosity delivered to the four main LHC experiments during the 2011 7 TeV (left) and 2012 8 TeV (right) runs.	40
2.3	This CERN accelerator complex. Showing the full chain of accelerators used for the LHC protons: LINAC2, Booster, PS, SPS, and LHC. Additionally, the four large experiments on the LHC are shown: ALICE, ATLAS, CMS, LHCb.	41
2.4	The integrated luminosity delivered and collected by the CMS experiment during the 2011 7 TeV (left) and 2012 8 TeV (right) runs.	43

LIST OF FIGURES

2.5	Sectional view of the CMS detector. The LHC beams travel in opposite directions along the central axis of the CMS cylinder colliding in the middle of the CMS detector.	44
2.6	Value of magnetic field $ B $ (left) and field lines (right) predicted on a longitudinal section of the CMS detector, for the underground model at a central magnetic flux density of 3.8 T. Each field line represents a magnetic flux increment of 6 Wb.	48
2.7	Schematic view of one quarter of the silicon tracker in the $r-z$ plane. The positions of the pixel modules are indicated within the hatched area. At larger radii within the lightly shaded areas, solid rectangles represent single strip modules, while hollow rectangles indicate pairs of strip modules mounted back-to-back with a relative stereo angle.	50
2.8	Layout of the pixel detectors in the CMS tracker.	51
2.9	Layout of the pixel sensor in the CMS tracker.	51
2.10	Predicted resolution of several track parameters for single muons with 1, 10, and 100 GeV: transverse momentum (left), transverse impact parameter (center), and longitudinal impact parameter (right).	54
2.11	Layout of the CMS electromagnetic calorimeter showing the arrangement of crystal modules, supermodules and end caps, with the preshower in front.	56
2.12	Effective momentum resolution σ_{eff}/p for electrons in the EB as a function of the momentum for the ECAL-only, the tracker-only, and the combined estimates.	57
2.13	A quarter slice of the CMS HCAL detectors. The right end of the beam line is the interaction point, HF (not pictured) would be located far to the left. In the diagram, the numbers on the top and left refer to segments in η , and the numbers on the right and the bottom refer to depth. Colors/shades indicate the combinations of layers that form the different depth segments, which are numbered sequentially starting at 1, moving outward from the interaction point. The outer calorimeter is assigned depth 4. Segmentation along ϕ is not shown.	59
2.14	The jet transverse energy resolution as a function of the simulated jet transverse energy for barrel jets ($ \eta < 1.4$), endcap jets ($1.4 < \eta < 3.0$) and very forward jets ($3.0 < \eta < 5.0$)	60
2.15	The muon momentum resolution versus p using the muon system only, the inner tracker only, or both (“full system”). (left) Barrel $ \eta < 0.2$ and (right) endcap $1.8 < \eta < 2.0$	61
2.16	Layout of one quarter of the CMS muon system for initial low luminosity running. The RPC system is limited to $ \eta < 1.6$ in the endcap, and for the CSC system only the inner ring of the ME4 chambers have been deployed	63

LIST OF FIGURES

2.17 Distribution of electron BDT output for training sample $W+\text{jets}$, test sample $Z+\text{jets}$ on 2012 data (fakes) and prompt electrons ($Z \rightarrow ee$ simulation) in the barrel (left) and endcap(right)	69
2.18 (left) Relative difference between the dilepton mass peak positions in data and simulation as obtained from Z , J/ψ and $\Upsilon(nS)$ resonances as a function of the transverse momentum of one of the electrons regardless of the second for dielectron events before p_T dependent correction. (right) Relative difference between the dilepton mass peak positions in data and simulation as obtained from Z , J/ψ and $\Upsilon(nS)$ resonances as a function of the transverse momentum of one of the electrons regardless of the second for dielectron events.	72
2.19 (left) Relative difference between the dilepton mass peak positions in data and simulation as obtained from Z , J/ψ and $\Upsilon(nS)$ resonances as a function of the average muon p_T^μ for dimuon events. (right) Relative difference between the dimuon mass resolutions in data and simulation as measured from Z , J/ψ and $\Upsilon(nS)$ decays as functions of the average muon	74
2.20 An example event of jets formed with the anti- k_T clustering algorithm.	76
2.21 Hierarchy of the CMS silicon pixel detector structures.	79
2.22 Hierarchy of the CMS silicon strip detector structures.	80
2.23 Day-by-day value of the relative longitudinal shift between the two half-shells of the BPIX as measured with the primary vertex residuals, for the last month of pp data taking in 2012. Red crosses show the shift observed using the data coming from the prompt reconstruction. The same events, re-reconstructed after the 2012 alignment campaign, which accounts for the major changes in the positions of the half-shells, are represented by black lozenges. A major displacement of the half-shells O(100) μm , occurred during the technical stop in the week of 20th of November, is recovered by the prompt alignment of the BPIX large structures that became active on the 30th November.	82
3.1 Standard Model Higgs boson production cross sections and relative uncertainties at $\sqrt{s} = 7 \text{ TeV}$ and $\sqrt{s} = 8 \text{ TeV}$. From top to bottom these are $pp \rightarrow H$, blue, $pp \rightarrow H + 2\text{jets}$, red, $pp \rightarrow H + W$, green, $pp \rightarrow H + Z$, grey, $pp \rightarrow H + t\bar{t}$, purple.	85
3.2 Feynman diagram depicting Higgs boson production through gluon-gluon fusion $gg \rightarrow H$. The fermion loop is dominated by top quarks, however all quarks contribute according to their masses.	85
3.3 Feynman diagram depicting Higgs boson production through vector boson fusion $qq \rightarrow H + 2\text{jets}$	86
3.4 Feynman diagram depicting Higgs boson production associated with a vector boson $qq \rightarrow H + W/Z$	87

LIST OF FIGURES

3.5	Feynman diagram depicting Higgs boson production in association with two top quarks $gg \rightarrow H + t\bar{t}$	87
3.6	(left) Standard Model Higgs boson decay branching ratios for selected decay modes, of specific interest for this thesis is the ZZ branching ratio. (right) Branching ratio times cross section for selected final states, of specific interest for this thesis is the $ZZ \rightarrow 4\ell (\ell^+\ell^-\ell^+\ell^-)$	89
3.7	Feynman diagram depicting Higgs boson decay into two Z bosons and subsequently into four leptons $H \rightarrow ZZ \rightarrow 4\ell$	90
3.8	Feynman diagram depicting the quark production of two Z bosons $qq \rightarrow ZZ$	91
3.9	Feynman diagram depicting the gluon production of two Z bosons $gg \rightarrow ZZ$	91
3.10	Total width of the SM Higgs boson as a function of its mass.	93
3.11	(top) Feynman diagram depicting Higgs boson production through gluon-gluon fusion and subsequent decay to two Z bosons $gg \rightarrow H \rightarrow ZZ$. (bottom) Feynman diagram depicting ZZ production through gluon-gluon fusion $gg \rightarrow ZZ$. These two diagrams will interfere with each other having an affect on the final number of events observed in the 4ℓ final state.	94
3.12	The NNLO ZZ (black) and WW (red) invariant mass distributions for $m_H = 125$ GeV.	95
3.13	The LO ZZ invariant mass distribution $gg \rightarrow ZZ$ for $m_H = 125$ GeV. Black is the total $gg \rightarrow \dots \rightarrow ZZ$ contribution once all interference effects are taken into account. Red is the $gg \rightarrow H^* \rightarrow ZZ$ signal only, and cyan is the $gg \rightarrow \dots \rightarrow ZZ$ contribution ignoring the interference between the two contributions. For scale, the $q\bar{q} \rightarrow ZZ$ contribution is shown in blue.	97
3.14	Distribution of the expected four-lepton reconstructed mass in full analysis mass range for the sum of the $4e$, 4μ , and $2e2\mu$ channels and for $gg + VV \rightarrow ZZ$ processes for a Higgs boson mass of 125.6 GeV. The expected distribution for a scenario corresponding to a scaling of the width by 25 is also shown. This illustrates the expected change in $gg + VV \rightarrow ZZ$ production when changing the Higgs boson width and at the same time constraining the peak cross section to the SM expectation.	98
4.1	Efficiency, as a function of the lepton p_T^ℓ , for reconstructing and selecting (left) electrons and (right) muons, measured with a $Z \rightarrow \ell\ell$ data sample by using a tag-and-probe method.	111

LIST OF FIGURES

4.2 Geometrical acceptance times selection efficiency for the SM Higgs boson signal as a function of m_H in the three final states for gluon fusion production. Points represent efficiency estimated from full CMS simulation; lines represent a smooth polynomial curve interpolating the points, used in the analysis. The vertical dashed line represents $m_H = 126$ GeV.	115
4.3 (left) Validation of the method using the SS control sample. The observed $m_{4\ell}$ distribution (black dots), prediction of the reducible background (dark green area), and expected contributions from ZZ (light blue area) are shown. (right) Prediction for the reducible background in all three decay channels together (black dots) fitted using an empirical shape (blue curve) with indicated total uncertainty (yellow band). The contributions from the 2P2F-like (solid green) and 3P1F-like (dashed red) processes are fitted separately.	118
4.4 Distribution of the four-lepton reconstructed mass in the full mass range $70 < m_{4\ell} < 1000$ GeV for the sum of the $4e$, $2e2\mu$, and 4μ channels. Points with error bars represent the data, shaded histograms represent the backgrounds, and the unshaded histogram represents the signal expectation for a mass hypothesis of $m_H = 126$ GeV. Signal and the ZZ background are normalized to the SM expectation; the $Z + \text{jets}$ background to the estimation from data. The expected distributions are presented as stacked histograms. No events are observed with $m_{4\ell} > 800$ GeV.	121
4.5 The $H \rightarrow ZZ \rightarrow 4\ell$ invariant mass distribution for $m_H = 126$ GeV in the (left) $4e$, (center) $2e2\mu$, and (right) 4μ channels. The distributions are fitted with a double-sided CB function and the fitted values of the CB width σ_{dCB} are indicated. The values of effective resolution, defined as half the smallest width that contains 68.3% of the distribution, are also indicated. The distributions are arbitrarily normalized.	122
4.6 Illustration of the production and decay of a particle H , $gg(q\bar{q}) \rightarrow H \rightarrow ZZ \rightarrow 4\ell$, with the two production angles θ^* and Φ_1 shown in the H rest frame and three decay angles θ_1 , θ_2 , and Φ shown in the Z_1 , Z_2 , and H rest frames, respectively.	123
4.7 Distributions of the eight kinematic observables used in the $H \rightarrow ZZ \rightarrow 4\ell$ analysis: m_{Z_1} , m_{Z_2} , $\cos \theta^*$, $\cos \theta_1$, $\cos \theta_2$, Φ , and Φ_1 . The observed data (points with error bars), the expectations for the SM background (shaded areas), the SM Higgs boson signal (open areas under the solid histogram), and the alternative spin-zero resonances (open areas under the dashed histograms) are shown, as indicated in the legend. The mass of the resonance is taken to be 125.6 GeV and the SM cross section is used. All distributions, with the exception of $m_{4\ell}$, are presented with the requirement $121.5 < m_{4\ell} < 130.5$ GeV.	125

LIST OF FIGURES

4.8 Distribution of the kinematic discriminant $\mathcal{D}_{\text{bkg}}^{\text{kin}}$ versus the four-lepton reconstructed mass $m_{4\ell}$ in the (left) low-mass and (right) high-mass regions. The color scale represents the expected relative density in linear scale (in arbitrary units) of background events. The points show the data and the measured per-event invariant mass uncertainties as horizontal bars. One $2e2\mu$ event with $m_{4\ell} \approx 220$ GeV and small $\mathcal{D}_{\text{bkg}}^{\text{kin}}$ has a huge mass uncertainty, and it is displayed as the horizontal line. No events are observed for $m_{4\ell} > 800$ GeV.	127
4.9 (left) Distribution of $\mathcal{D}_{\text{bkg}}^{\text{kin}}$ versus $m_{4\ell}$ in the low-mass range with colors shown for the expected relative density in linear scale (in arbitrary units) of background plus the Higgs boson signal for $m_H = 126$ GeV. The points show the data, and horizontal bars represent the measured mass uncertainties. (right) Distribution of the kinematic discriminant $\mathcal{D}_{\text{bkg}}^{\text{kin}}$ for events in the mass region $121.5 < m_{4\ell} < 130.5$ GeV. Points with error bars represent the data, shaded histograms represent the backgrounds, and the unshaded histogram the signal expectation. Signal and background histograms are stacked.	128
4.10 Main observables discriminating production mechanisms in 0/1 jet and Dijet categories in arbitrary units. $q\bar{q}H$ is used in these figures for VBF production. (top left) \mathcal{D}_{jet} Discriminant combining VBF discrimination variables. (top right) p_T of the four-lepton system. (bottom left) $\Delta\eta$ of the two leading jets. (bottom right) Invariant mass of the two jets.	130
4.11 (left) Distribution of $p_T^{4\ell}$ versus $m_{4\ell}$ in the low-mass-range 0/1-jet category with colors shown for the expected relative density in linear scale (in arbitrary units) of background plus the Higgs boson signal for $m_H = 126$ GeV. No events are observed for $p_T^{4\ell} > 150$ GeV. The points show the data, and horizontal bars represent the measured mass uncertainties. (right) Distribution of $p_T^{4\ell}$ in the 0/1-jet category for events in the mass region $121.5 < m_{4\ell} < 130.5$ GeV. Points with error bars represent the data, shaded histograms represent the backgrounds, and the red histograms represent the signal expectation, broken down by production mechanism. Signal and background histograms are stacked.	131
4.12 (left) Distribution of \mathcal{D}_{jet} versus $m_{4\ell}$ in the low-mass-range dijet category with colors shown for the expected relative density in linear scale (in arbitrary units) of background plus the Higgs boson signal for $m_H = 126$ GeV. The points show the data and horizontal bars represent the measured mass uncertainties. (right) Distribution of \mathcal{D}_{jet} in the dijet category for events in the mass region $121.5 < m_{4\ell} < 130.5$ GeV. Points with error bars represent the data, shaded histograms represent the backgrounds, and the red histograms represent the signal expectation, broken down by production mechanism. Signal and background histograms are stacked.	132

LIST OF FIGURES

4.13 Distribution of the four-lepton reconstructed mass for the sum of the $4e$, $2e2\mu$, and 4μ channels for the mass region $70 < m_{4\ell} < 180$ GeV. Points with error bars represent the data, shaded histograms represent the backgrounds, and the unshaded histogram represents the signal expectation for a mass hypothesis of $m_H = 126$ GeV. Signal and the ZZ background are normalized to the SM expectation, the $Z + \text{jets}$ background to the estimation from data.	134
4.14 Observed and expected 95% C.L. upper limit on the ratio of the production cross section to the SM expectation. The expected $\pm 1\sigma$ and $\pm 2\sigma$ C.L. ranges of expectation for the background-only model are also shown with green and yellow bands, respectively.	141
4.15 (left) Significance of the local excess with respect to the SM background expectation as a function of the Higgs boson mass in the full mass range 110–1000 GeV. Results obtained using the 1D fit, 2D fit, and the nominal 3D fit. (right) Significance of the local excess with respect to the SM background expectation as a function of the Higgs boson mass for the 1D fit, 2D fit, and the nominal 3D fit. Results are shown for the full data sample in the low-mass region only.	142
4.16 Signal to background ratio's for expected and observed events, computed from the 1D (left), 2D (left), and 3D (right) likelihoods. These plots are made from the $m_{4\ell} \in 121.5$ – 130.5 GeV region to study the observed peak. The signal used as the Higgs boson hypothesis corresponds to $m_H = 126$ GeV. These plots are preliminary and unpublished.	143
4.17 (left) Observed and expected 95% C.L. upper limit on the ratio of the production cross section to the SM expectation where a 126 GeV Higgs boson is added as background. The expected $\pm 1\sigma$ and $\pm 2\sigma$ C.L. ranges of expectation for the background-only model are also shown with green and yellow bands, respectively. (right) Significance of the local excess with respect to the SM background + 126 GeV Higgs boson expectation as a function of the BSM Higgs boson mass and compared to the expected and observed significance of the SM Higgs boson. These results were obtained from a preliminary version of the 4ℓ analysis and are unpublished.	145
4.18 (left) Values of μ for the two categories. The vertical line shows the combined μ together with its associated $\pm 1\sigma$ uncertainties, shown as a green band. The horizontal bars indicate the $\pm 1\sigma$ uncertainties in μ for the different categories. The uncertainties include both statistical and systematic sources of uncertainty. (right) Likelihood contours on the signal-strength modifiers associated with fermions ($\mu_{ggH,t\bar{t}H}$) and vector bosons ($\mu_{VBF,VH}$) shown at a 68% and 95% C.L.	147
5.1 This is a sample figure	150

Chapter 1

Introduction

In this document we outline the search for and characterization of the last undiscovered particle predicted by the Standard Model of Particle Physics. This model presents explanations for matter and energy in the universe. It has been tested and verified at the smallest distance scales and highest energies in the universe. To present the ideas outlined in this thesis, it is necessary to start with a collection of definitions. Some will be given here, while others are left to references or outside sources.

The natural starting point of this discussion is to present a useful example of symmetries that are observed in the world and how these are classified in physics. Next, a basic discussion of quantum field theory and scattering amplitudes will be presented. From these examples, the discussion will expand to a categorization of the particles, fields, and symmetries that make up the Standard Model of Particle Physics, including an introduction of Electroweak Symmetry Breaking. Equipped

CHAPTER 1. INTRODUCTION

with these ideas an outline of Limitations of the Standard Model are presented using the Higgs boson as a tool for understanding them.

1.1 Symmetries in Physics

Symmetry is one of, if not the, most important features in the physics of the natural world. As we pull together the various pieces needed to present the state of the art in particle physics, we will define multiple symmetries that exist in nature and how we use them to test our current and hypothetical models.

1.1.1 Noether's Theorem

To begin, let us define the *symmetry group* of the system, G , as the local group that transforms solutions into other solutions. If x is a solution and g is a group element, then $g \cdot x$ will also be a solution. In Physics, the solutions that we consider either that maximize or minimize the action:

$$\mathcal{S} = \int d^4x \mathcal{L}, \tag{1.1}$$

where the integrand, \mathcal{L} , is the *Lagrangian* of the system, $\mathcal{L} = T - V$. The T and V are the kinetic and potential energy, respectively. So a symmetry group of a physical system would be the set of transformations that leave the Lagrangian invariant. This concept became one of most important in physics after Emmy Noether

CHAPTER 1. INTRODUCTION

proved that these symmetries of the action correspond to conserved quantities that do not change as the system evolves [1].

1.1.2 Angular Momentum and the Rotation Group

To demonstrate the importance of Noether's Theorem, let us consider the group of rotations in 3 dimensional space, the special orthogonal group in 3 dimensions, $\text{SO}(3)$. Given any unit vector $\hat{\mathbf{n}}$ a rotation about this vector by an angle ψ is denoted by $R_{\hat{\mathbf{n}}}(\psi)$. Here we will use the Euler Angles to parameterize R , where the rotations about the (x, y, z) axis are given by (α, β, γ) respectively. It will also be useful to note that performing a rotation R_1 followed by another rotation R_2 is equivalent to a single rotation R_3 , or that the set of rotations is closed.

A arbitrary rotation $R(\alpha, \beta, \gamma)$ can be decomposed into rotations about the fixed axes, $R(\alpha, \beta, \gamma) = R_x(\alpha)R_y(\beta)R_z(\gamma)$. Figure 1.1 shows these angles for the transformation of vector N from (x, y, z) to (X, Y, Z) . At this point it is useful to express the rotations $R_{x,y,z}$ in terms of their matrix formulation, equations (1.2), (1.3), (1.4). Where the angle of rotation must satisfy $0 \leq \psi \leq 2\pi$.

$$R_z(\gamma) = \begin{pmatrix} \cos \gamma & -\sin \gamma & 0 \\ \sin \gamma & \cos \gamma & 0 \\ 0 & 0 & 1 \end{pmatrix} \quad (1.2)$$

CHAPTER 1. INTRODUCTION

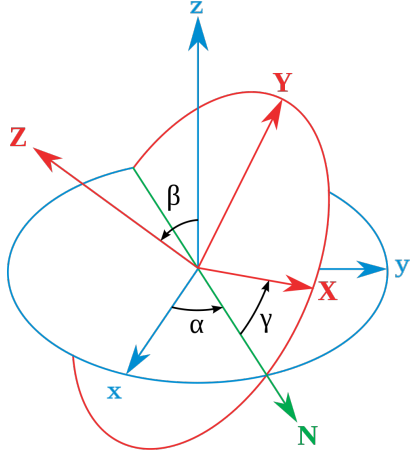


Figure 1.1: Euler angles for three dimensional Cartesian coordinates. [2]

$$R_y(\beta) = \begin{pmatrix} \cos \beta & 0 & \sin \beta \\ 0 & 1 & 0 \\ -\sin \beta & 0 & \cos \beta \end{pmatrix} \quad (1.3)$$

$$R_x(\alpha) = \begin{pmatrix} 1 & 0 & 0 \\ 0 & \cos \alpha & -\sin \alpha \\ 0 & \sin \alpha & \cos \alpha \end{pmatrix} \quad (1.4)$$

The reader should note that a vector along the z -axis direction will be left unchanged due to a R_z rotation. More generally, we can apply Noether's Theorem when the Lagrangian for a physical system does not depend on infinitesimal rotations about any axis, $\mathcal{L} - \mathcal{L}(\delta\alpha, \delta\beta, \delta\gamma) = 0$. This symmetry corresponds to the classical

CHAPTER 1. INTRODUCTION

conservation of angular momentum, \mathbf{J} , when the Lagrangian has spherical symmetry. This symmetry will become important as we discuss the kinematics of the particles we use to study new discoveries.

1.1.3 Inherent Spin and $SU(2)$

If one fixes a direction in equations (1.2), (1.3), and (1.4) then the rotations about that direction will form a subgroup of $SO(3)$. This becomes clear when you consider the closure, identity, and inverse group axioms for the subset of rotations R_z . Specifically, the subgroup is isomorphic to the special unitary group of rotations in two dimensions, $SU(2)$. One way to write this new transformation is:

$$R(\phi) = \begin{pmatrix} \cos \phi & -\sin \phi \\ \sin \phi & \cos \phi \end{pmatrix} \quad (1.5)$$

The simplest way to represent a group is to find the elements that all other elements of the group can be made from. To find these elements for $SU(2)$ start with equation (1.5) and consider an infinitesimal rotation $d\phi$. Since $R(\phi)$ is differentiable one can derive an equation to write all possible rotations in terms of the operator matrix \mathbf{J} which we will call the *generator* of $SU(2)$. Explicitly, $R(\phi)$ can be written as:

$$R(\phi) = e^{-i\frac{\phi}{2}\mathbf{J}}, \quad (1.6)$$

CHAPTER 1. INTRODUCTION

where $J_i = \tau_i$ and τ_i is one of the Pauli matrices:

$$\tau_1 = \begin{pmatrix} 0 & 1 \\ 1 & 0 \end{pmatrix}, \tau_2 = \begin{pmatrix} 0 & -i \\ i & 0 \end{pmatrix}, \tau_3 = \begin{pmatrix} 1 & 0 \\ 0 & -1 \end{pmatrix} \quad (1.7)$$

In this formulation $R(\phi)$ operates on states that are linear combinations of *two-component spinors* given by equation (1.8). These spinor eigenstates have an inherent conserved spin of $\pm \hbar/2$.

$$\chi_+ = \begin{pmatrix} 1 \\ 0 \end{pmatrix}, \chi_- = \begin{pmatrix} 0 \\ 1 \end{pmatrix} \quad (1.8)$$

These states can be expressed as linear combinations of these two component spinors, but we will find it more useful to transform the basis so that they can be rewritten in terms of the two component spinors ψ_R (right-handed) and ψ_L (left-handed) that are eigenstates of the parity transformation¹.

$$\psi = \begin{pmatrix} \psi_R \\ \psi_L \end{pmatrix} \quad (1.9)$$

These states, called *fermions*, and the group SU(2) will be two of the major building blocks that are used when we discuss the Standard Model of particle physics. Before we describe this model we will take some time to discuss Scattering Amplitudes.

¹As position transforms from $\vec{x} \rightarrow -\vec{x}$ the momentum transforms as $\vec{p} \rightarrow -\vec{p}$

1.2 Scattering Amplitudes

Particle physics research at its core is not very different from pre-school; we want to see what is inside of something but can't get our hands in the tiny spaces, so we smash it apart. The complexity that is swept under the rug in this statement is that we can map what is happening in these small spaces to what we observe using scattering amplitudes, which tell us the behavior of particles as they "break away" from the things we are trying to study. More generally, a scattering matrix tells us how a system of particles will evolve over time, either because of collisions between particles or other natural processes.

1.2.1 Scattering Matrix

To explain how particle physics explains the evolution of a system over time, we will follow a procedure outlined in [3]. Let us consider a set of particle fields with certain characteristics denoted $|\psi\rangle(t)$. The system at a time t is given in Dirac notation [4]. We will denote the initial state of the system as $|\psi_i\rangle = |\psi\rangle(t_i)$, and the final state as $|\psi_f\rangle = |\phi\rangle(t_f)$. These states can be single or multiple particle states and typically quantities like momentum, spin, or helicity² are used to specify them in this notation.

²Projection of spin onto momentum, $\vec{S} \cdot \hat{p}$

CHAPTER 1. INTRODUCTION

The evolution of a system from state $|\psi_i\rangle$ to $\langle\psi_f|$ is given by

$$\langle\psi_f| S |\psi_i\rangle, \quad (1.10)$$

where S is a quantum mechanical operator associated with the scattering matrix.

To give a concrete example you can consider a plane wave evolving over time.

In this case, $S = e^{-iH(t-t_i)}$. For this explanation, we use a Hamiltonian H instead of a Lagrangian, but a Hamiltonian is simply the Legendre transformation of a Lagrangian, so they are equivalent for our purpose. In this case, equation (1.10) becomes

$$\langle\psi_f| e^{-iH(t_f-t_i)} |\psi_i\rangle. \quad (1.11)$$

In the limit that $t_f - t_i \rightarrow \infty$ the operator between the states is the *scattering matrix* and maps some initial state to a final state at some other time.

1.2.2 Amplitudes and Feynman Diagrams

Each of the states outlined in the previous section, $|\psi\rangle(t)$, will have specific properties. For example, the initial state may be in eigenstate a for some commuting operator, while the final state may be in eigenstate b of the same operator. Then the evolution of the system from $|a\rangle$ to $|b\rangle$ will be through a specific *matrix element*, \mathcal{M}_{ab} .

CHAPTER 1. INTRODUCTION

$$\mathcal{M}_{ab} = \langle b | S | a \rangle \quad (1.12)$$

These matrix elements can be used to describe the evolution of the system through very specific transitions. These matrix elements are also called *scattering amplitudes*, A , for a specific process.

$$A_{ab} = \mathcal{M}_{ab} = \langle b | S | a \rangle \quad (1.13)$$

These amplitudes can also be expressed in a pictorial form, called *Feynman diagrams*, that we will use extensively in this document. These diagrams are used to do the calculations through rules mapping vertex points, internal, and external lines to terms in the matrix element pieces.

To use a concrete example, we will describe the interaction of electrons through the electromagnetic interaction. The Lagrangian for two fermions interacting electromagnetically is given by

$$\mathcal{L}_{EM} = \bar{\psi} (i\gamma^\mu (\partial_\mu + ieA_\mu) - m) \psi. \quad (1.14)$$

In this equation, the electromagnetic interaction terms are represented by the vector potential, A_μ , with e as the coupling constant of the particle to the electromagnetic field. The 4×4 Dirac matrices γ^μ are defined by the 2×2 Identity matrix (1) and the Pauli-matrices we have already seen

CHAPTER 1. INTRODUCTION

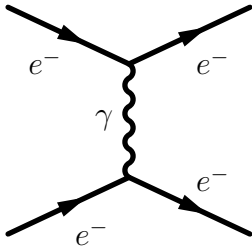


Figure 1.2: Feynman diagram depicting electron-electron scattering via the electro-magnetic interaction.

$$\gamma^0 = \begin{pmatrix} 1 & 0 \\ 0 & -1 \end{pmatrix}, \gamma^i = \begin{pmatrix} 0 & \tau^i \\ -\tau^i & 0 \end{pmatrix}. \quad (1.15)$$

In the amplitude notation this can be written as

$$A = \langle \psi_1 \psi_2 | e^{\bar{\psi}(i\gamma^\mu(\partial_\mu + ieA_\mu) - m)\psi} | \psi_1 \psi_2 \rangle \quad (1.16)$$

The equivalent representation lowest order terms of equation (1.14) as Feynman diagrams will be figure 1.2. These diagrams can be used to quickly and simply represent complex interactions of particles and range from very simple, figure 1.2, to extremely complex, as in the comedic example 1.3. Relevant and practical examples will be presented in section 3.

In this example we can see the properties of another group that will be important for the Standard Model. The electromagnetic interaction requires U(1) gauge symmetry. The conserved quantity for this group is the electric charge of the fermion, given by e in the equations above. Now that we have introduced many of the pieces

CHAPTER 1. INTRODUCTION

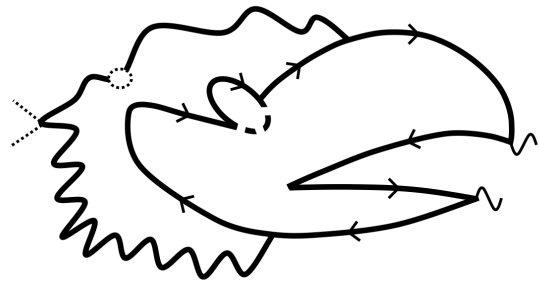


Figure 1.3: A comedic example of a complicated Feynman diagram designed to appear similar to a Jayhawk [5].

we need we will discuss the Standard Model of particle physics.

1.3 The Standard Model

So far we have considered very simple Lagrangians that describe very specific processes. These ideas are the basis for the construction of the *Standard Model* (SM) [6–9] of particle physics. This model attempts to describe and categorize the particles and interactions that make up the quantum world. The glaring omission is gravity, which is extremely weak compared to the other processes that are occurring at sub-atomic distance scales. Before we can discuss how the model describes the fundamental interactions we need to describe and categorize the material that the universe is made from.

CHAPTER 1. INTRODUCTION

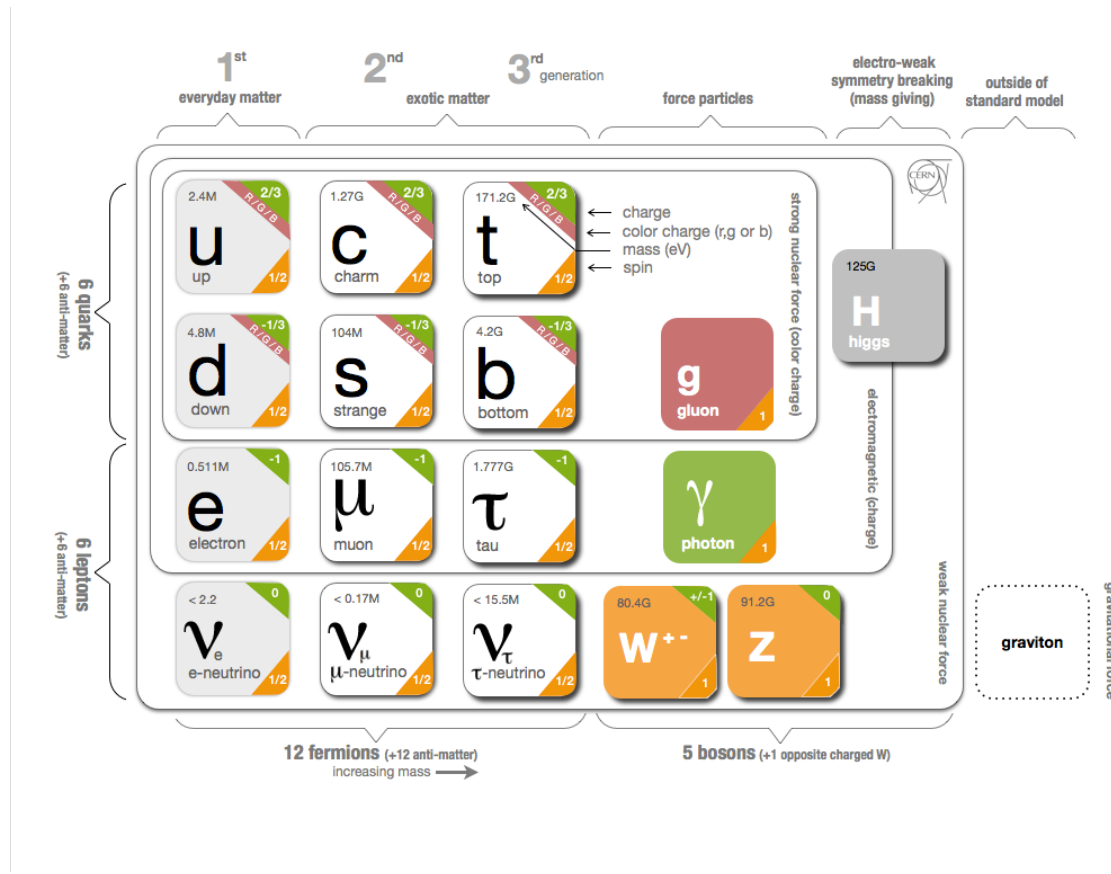


Figure 1.4: A Summary Infographic of the Standard Model. This is a modified version of original found at [10].

CHAPTER 1. INTRODUCTION

1.3.1 Matter

The SM provides a categorization of all the matter that makes up the universe. This categorization started with the first experiments attempting to describe atoms distinguishing the particles in the nucleus of an atom from the electrons that orbit around them. Today we know of matter in two categories, *quarks* and *leptons*, both of which are fermions with spins of $\hbar/2$, noted $1/2$ from now on³. For each of these categories there are three generations of particles, each generation consisting of two quarks (q), two leptons (ℓ) and their antiparticles⁴ ($\bar{q}, \bar{\ell}$). The heavier second and third generation fermions typically decay quickly into the first generation particles that make up the world we live in⁵.

1.3.1.1 Quarks

Quarks are the fundamental pieces that make up the nucleus of atoms. The protons and neutrons that are used to classify an atom are themselves built from combinations of quarks. The name “quark” was coined by Gell-Mann who credits the term to a passage from *Finnegans Wake* by James Joyce. Quarks come in six *flavors* arranged by mass into three generations of doublets, this flavor is preserved in electromagnetic and strong interactions. The first letter of the quark name is often used to designate them so up (u), down (d), charm (c), strange (s), top (t), and

³Here we have moved to the convention of natural units where $\hbar = c = 1$

⁴The antiparticle of a fermion is the C transform of the particle state. C transforms discussed more in section 1.4.1

⁵The neutrino’s being the exception to this.

CHAPTER 1. INTRODUCTION

bottom (b). Each flavor has a different mass ranging from \sim MeV (u and d) to ~ 170 GeV (t), the best knowledge of these masses is outlined in figure 1.4.

Everyday matter consists mainly of the first generation quarks, u and d , grouped into the protons and neutrons. Quarks are never observed alone due to a *color charge* that each possesses⁶. This will be discussed more in section 1.3.2, but for now we will refer to it as a charge that can be “red” (r), “blue” (b), or “green” (g). To be stable, a particle must be seen as “white” (w) to the outside world. Because matter must appear white, quarks group themselves into sets called *hadrons*. Hadrons come in classifications based on the number of valence quarks they have. Two quark states are quark-antiquark pairs called *mesons*, $(\text{r}\bar{\text{r}} + \text{b}\bar{\text{b}} + \text{g}\bar{\text{g}}) / \sqrt{3} = \text{w}$. Common examples of mesons are pions (π^0, π^\pm) that come from cosmic rays. Three quark states are called *baryons*, $\text{r} + \text{b} + \text{g} = \text{w}$, everyday examples being protons and neutrons. Recent observations also suggest tetraquark states [11] consisting of four quarks.

Each quark generation doublet has one particle with electromagnetic charge⁷ of $+2/3e$ and another with charge $-1/3e$. These will be combined so that all observable hadrons will have integer charges. The top-left section of figure 1.4 summarizes the properties and categorization of the quarks.

One additional item that will prove relevant is that quarks can be both right-handed and left-handed eigenstates of the parity transform. This will distinguish

⁶The property has nothing to do with optical color, but maps nicely to the mixing fundamental colors.

⁷“ e ” is used as the fundamental unit of electromagnetic charge. “ $-e$ ” is defined as the charge of an electron.

CHAPTER 1. INTRODUCTION

their interactions when we discuss the weak force in section 1.3.2.

1.3.1.2 Leptons

Unlike the quarks, leptons carry no property that stops them from existing by themselves. All leptons are neutral to color charge preventing them from interacting via the strong nuclear force. The most common lepton again belongs to the first generation, the electron. Electrons orbiting the nucleus of an atom are the most common leptons. Similar to the heavier generations of the quarks, the electron also has corresponding heavier generation flavors, the muon (μ) and tau (τ) leptons. All three of these leptons carry an electromagnetic charge of “ $-e$ ”, range in mass from $\sim 0.5 \text{ MeV}(e)$ to $\sim 1.7 \text{ GeV}(\tau)$, and can exist both as left or right-handed.

Each of these three leptons has a corresponding doublet partner as well, the neutrinos (ν_e, ν_μ, ν_τ). These particles are neutral in both color and electromagnetic charge, and are almost massless. Further complicating the story, they only exist as left-handed particles. They are extremely hard to interact with and detect since the electromagnetic and strong forces are invisible to them allowing them to only interact via the weak nuclear force. Additionally, unlike the quarks and the other leptons, they oscillate between different flavors without interacting with the environment because their mass eigenstates are not the same as their weak interaction eigenstates. In 1.4 the leptons occupy the bottom left portion of the table. A summary of the first generation fermion fields that are given in table 1.1 where the doublets are grouped

CHAPTER 1. INTRODUCTION

Fermion Field	EM charge (Q)	Weak Isospin (T_3)	Hypercharge (Y)	Color Charge
$L_L = \begin{pmatrix} \nu_L \\ e_L^- \end{pmatrix}$	$\begin{pmatrix} 0 \\ -1 \end{pmatrix}$	$\begin{pmatrix} +1/2 \\ -1/2 \end{pmatrix}$	-1	no
e_R^-	-1	0	-2	no
$Q_L = \begin{pmatrix} u_L \\ d_L \end{pmatrix}$	$\begin{pmatrix} +2/3 \\ -1/3 \end{pmatrix}$	$\begin{pmatrix} +1/2 \\ -1/2 \end{pmatrix}$	+1/3	yes
u_R	+2/3	0	+4/3	yes
d_R	-1/3	0	-2/3	yes

Table 1.1: First generation fermions and their different charges, grouped in left(right)-handed doublets(singlets).

together and the distinction between left and right-handed particles has been made.

While the only leptons in everyday matter are electrons, muons and neutrinos are also quite common. These particles exist as cosmic rays that are constantly bombarding us from the upper atmosphere and outer space. Muons offer a particularly interesting case because they are moving at relativistic speeds so that in our frame of reference they appear as long lived particles.

1.3.2 Forces

Now that we have introduced the building blocks of matter we can discuss how these particles interact. This description starts with a Lagrangian of terms describing

CHAPTER 1. INTRODUCTION

particles and their interactions with each other, however this Lagrangian needs to preserve specific symmetries that we observe in nature. Specifically the SM Lagrangian should have $U(1) \times SU(2) \times SU(3)$ local symmetry⁸. Each of these symmetries correspond to physical interactions between the particles in the theory. Mathematically it is extremely similar to equation (1.14), however the $(\partial_\mu + ieA_\mu)$ is replaced by the more complicated covariant derivative \mathcal{D}_μ .

$$\mathcal{D}_\mu = \partial_\mu - ig_1 \frac{Y}{2} B_\mu - ig_2 \frac{\tau^i}{2} W_\mu^i - ig_3 \frac{\lambda^a}{2} G_\mu^a \quad (1.17)$$

Each of these additional terms are present to preserve one of the local symmetries that we observe in the world. Each of the g_i variables are coupling constants that can be measured by experimental results. These new fields map to the fundamental forces and in turn *gauge bosons* that mediate each of the forces. They are called bosons because they have an integer unit of inherent spin, as apposed to the matter particles that all have half-integer spin. Particle physics models fermions interacting with each other as the exchange of these bosons between particles.

A rather glaring omission from both equation (1.14) and the extension using equation (1.17) is how these new fields (bosons) interact with themselves and each other. We will not take the time to introduce all of these terms but the relevant pieces will be used in section 1.3.3.

⁸The difference between a local and global symmetry has not been outlined in this document, but the author again refers you to [12–15] and many other places.

CHAPTER 1. INTRODUCTION

The term associated with g_1 is introduced to preserve local gauge invariance, $U(1)$, introducing a spin-1 field B_μ . The generator, Y (*hypercharge*), will be a constant for every particle. This term, intertwined with the g_2 term, describes the *electromagnetic force*. The g_2 term, along with the g_1 term, describes the *weak nuclear force*. The details of their combination will be described in section 1.3.3.

The g_2 term preserves rotations in flavor space, $SU(2)$, introducing three new vector fields W_μ^i where $i \in \{1, 2, 3\}$ and the generators τ^i (the Pauli matrices we have already seen). Similar to the case of angular momentum we have already seen, the $i = 3$ projection, T_3 , is a conserved quantity called *weak isospin* that is useful in computations.

Additionally, the W_μ^i bosons are exclusively left-handed, meaning it can only interact with left-handed particles (right-handed antiparticles). For now, it is useful to note that both the B_μ and the W_μ^3 terms represent interactions that preserve the original flavor of the fermions they act on. In the framework of equation (1.14) and figure 1.2 this means that the photon field, A_μ , is some linear combination of B_μ and W_μ^3 and the electroweak charge, e , is a linear combination of $g_1 \frac{Y}{2}$ and $g_2 \frac{\tau^3}{2}$.

The final term associated with g_3 represents the *strong nuclear force* and preserves rotations in the color charge space, $SU(3)$. This term introduces eight new vector fields G_μ^a with $a \in \{1, 2, 3, 4, 5, 6, 7, 8\}$ and eight generators λ^a which are the analog of the Pauli matrices in 3 dimensions. Each of these fields corresponds to a *gluon* that mediates the strong force. These interactions are described by Quantum

CHAPTER 1. INTRODUCTION

Chromodynamics (QCD), the quantum field theory for how particles with color charge (quarks & gluons) interact with each other. The conserved charge in this theory is the color; “redness”, “blueness”, and “greenness”. Each of the eight gluons in this theory is a superposition of color charge states and “holds” quarks of specific colors together into colorless hadrons. An explicit listing of the gluon states is not provided here, but a basic introduction can be found in [16].

Before going through the details of the electromagnetic and weak forces, a quick note on the relative strength of these interactions. The electromagnetic force is common in every day life because it is a relatively strong interaction and operates over long distances, for example the light from a distant star can be seen at night. The strongest of the forces is the strong nuclear force which keeps the quarks grouped in hadrons and hadrons together in a nucleus is much stronger but only impacts particles that are very close together. At larger distances the weakest of the forces considered in particle physics is the creatively named weak nuclear force, which governs the decay of higher generation fermions into lower generation fermions. In table 1.2 you can find a summary of the different forces and their relative strengths and interaction ranges.

Included in this table is the gravitational force. There are theoretical models for describing quantum gravity in the same framework as these other forces, that will be discussed more in later sections but as yet these have not been confirmed with observations.

Force	Bosons	Relative Strength	Range (m)
Strong	gluons (g)	1	10^{-15}
Electromagnetic	photon (γ)	$\frac{1}{137}$	∞
Weak	W^\pm, Z bosons	10^{-6}	10^{-18}
Gravity	graviton (G)	10^{-39}	∞

Table 1.2: List of Fundamental Forces their relative strengths and ranges.

1.3.3 Electroweak Symmetry Breaking

As eluded to above, the weak and electromagnetic forces are deeply connected. In their combined form they are referred to as the *Electroweak force*. In the description we outlined, this means that the SM has $SU(2) \times U(1)$ symmetry, giving rise to four gauge bosons that would mediate these two forces; B_μ , W_μ^1 , W_μ^2 , and W_μ^3 . In the mathematical construction that we have presented all of these W_μ^i bosons would be massless, but this would contradict the observed range of the weak force outlined in Table 1.2. To give these bosons mass, the symmetry of the system must be broken. The *Higgs Mechanism* [17–22] has been proposed as the source of the *Electroweak Symmetry Breaking* [23].

To see how this happens, focus on the kinetic energy terms of the W_μ^i and B_μ fields that we neglected previously. These are given by equation (1.18) following the Weinberg-Salam Model of electroweak interactions [6–9]. This equation is the

CHAPTER 1. INTRODUCTION

first appearance of the Field Tensors, these take the form $B_{\mu\nu} = \partial_\nu B_\mu - \partial_\mu B_\nu$ and

$$W_{\mu\nu}^i = \partial_\nu W_\mu^i - \partial_\mu W_\nu^i + g\epsilon^{ijk}W_\mu^j W_\nu^k.$$

$$\mathcal{L}_{KE} = -\frac{1}{4}W_{\mu\nu}^i W^{\mu\nu i} - \frac{1}{4}B_{\mu\nu} B^{\mu\nu} \quad (1.18)$$

When one adds an additional complex scalar SU(2) doublet, Φ , to this theory we find the key to giving some of these fields mass. We write this new scalar field in terms of its components shown in equation (1.19).

$$\Phi = \begin{pmatrix} \phi^+ \\ \phi^0 \end{pmatrix} = \begin{pmatrix} \phi^1 + i\phi^2 \\ \phi^3 + i\phi^4 \end{pmatrix} \quad (1.19)$$

What makes this new field the key is the special potential energy term that accompanies it. This potential, given in equation (1.20), and its parameters, λ and μ , define how the field interacts with itself and will be vital in our discussion.

$$V(\Phi) = \mu^2 |\Phi^\dagger \Phi| - \lambda (|\Phi^\dagger \Phi|)^2 \quad (1.20)$$

Putting all of the pieces together we can write a toy Lagrangian for the electroweak part of the SM⁹ as

$$\mathcal{L}_{EW} = -\frac{1}{4}W_{\mu\nu}^i W^{\mu\nu i} - \frac{1}{4}B_{\mu\nu} B^{\mu\nu} + |\mathcal{D}_\mu \Phi|^2 - V(\Phi). \quad (1.21)$$

⁹In what follows we omit QCD terms, while fermion terms are left for later discussion.

CHAPTER 1. INTRODUCTION

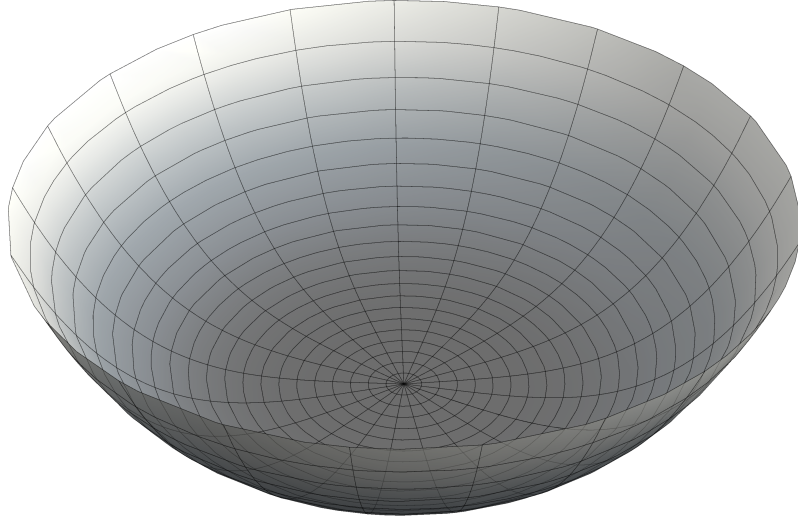


Figure 1.5: A 2D illustration of the scalar potential, $V(\Phi)$, when $\mu^2 > 0$. The horizontal axes form the complex plane ϕ_1 vs ϕ_2 , while the vertical axis is $V(\Phi)$. Created with [24].

When one investigates the behavior of this system as the total energy approaches zero¹⁰ the fields will approach their ground state. Focusing on the scalar potential one can see the behavior depends on the sign of the parameters μ^2 and λ . We assume that $\lambda > 0$ so that a minimum state exists at all. If $\mu^2 > 0$ then the system will have a natural minimum where $\Phi = 0$ that preserves all of the symmetries that we have already outlined. This can be seen in the natural two-dimensional form and in the one-dimensional projection in figures 1.5 and 1.6 respectively.

The more interesting case is when $\mu^2 < 0$. In this case the potential has a minimum that is not at $\Phi = 0$ but the minimum energy state will occur at what we call the *vacuum expectation value* (VEV) given in equation (1.22). This means

¹⁰A stable minimum energy state being analogous to the current state of the universe.

CHAPTER 1. INTRODUCTION

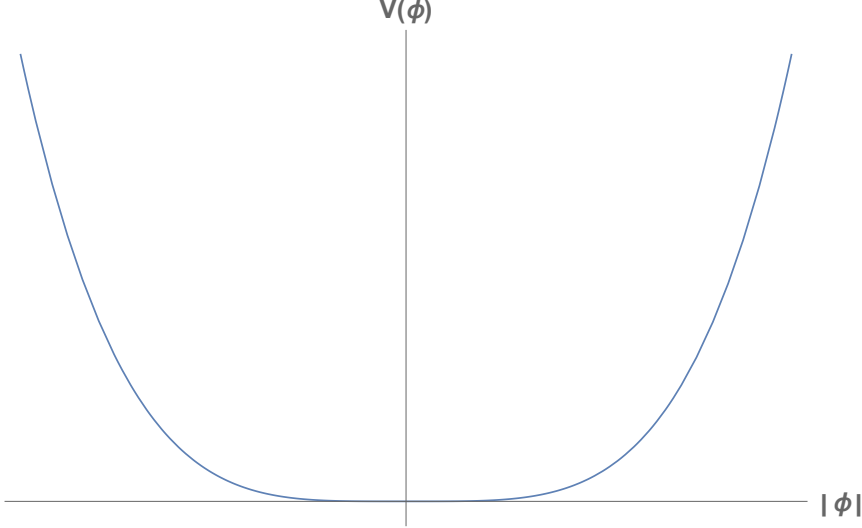


Figure 1.6: A 1D illustration of the scalar potential, $V(\Phi)$, when $\mu^2 > 0$. Created with [24].

that in the ground state, the scalar field will not go to zero but will have some amount of energy defined as $\frac{v}{\sqrt{2}}$ breaking the U(1) symmetry. Figures showing the natural two-dimensional potential and one-dimensional projection are seen in 1.7 and 1.8 respectively.

$$\langle \Phi \rangle = \sqrt{-\frac{\mu^2}{2\lambda}} \begin{pmatrix} 0 \\ 1 \end{pmatrix} \equiv \frac{1}{\sqrt{2}} \begin{pmatrix} 0 \\ v \end{pmatrix} \quad (1.22)$$

The choice of the VEV contribution to the ϕ^1, ϕ_2, ϕ_3 or ϕ_4 component in SU(2) space is arbitrary but we have chosen the conventional notation here, giving the new doublet a hypercharge of $Y_\Phi = 1$ and a electromagnetic charge $Q_{EM} = \frac{\tau^3 + Y}{2}$. This gives an electromagnetically neutral ground state, even though the field retains its VEV. So, by giving the scalar field a non-zero expectation value in the ground state we have broken the $SU(2) \times U(1)$ symmetry to give a local $U(1)_{EM}$ symmetry of the

CHAPTER 1. INTRODUCTION

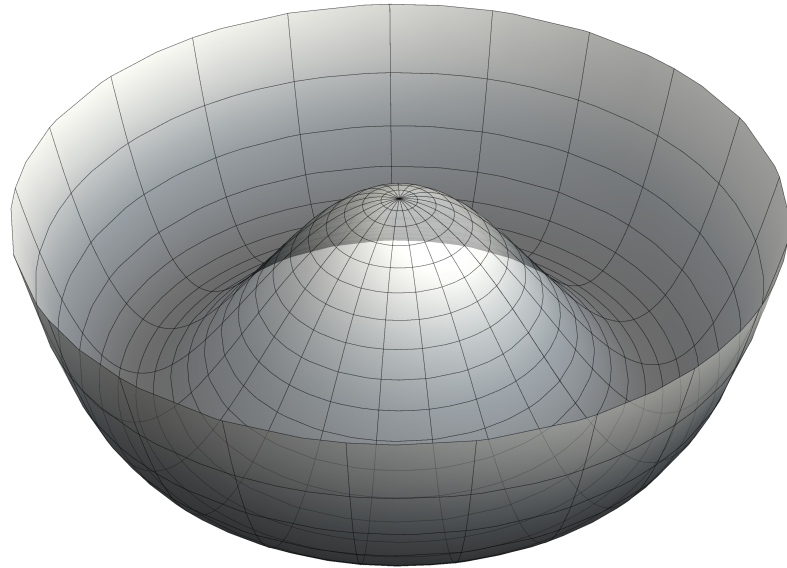


Figure 1.7: A 2D illustration of the scalar potential, $V(\Phi)$, when $\mu^2 < 0$. The horizontal axes form the complex plane ϕ_1 vs ϕ_2 , while the vertical axis is $V(\Phi)$. Created with [24].

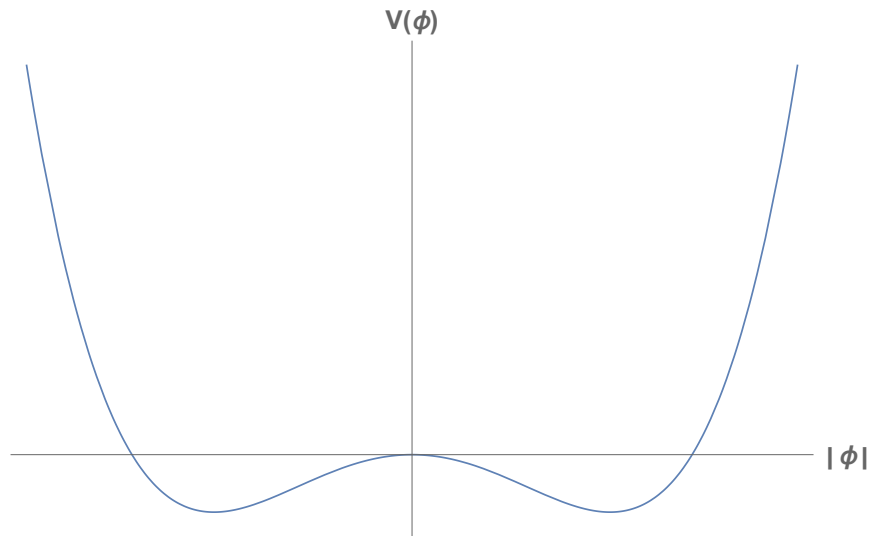


Figure 1.8: A 1D illustration of the scalar potential, $V(\Phi)$, when $\mu^2 > 0$. Created with [24].

CHAPTER 1. INTRODUCTION

electromagnetic force¹¹.

We can see the difference between the masses of the original bosons by using the gauge invariance of the field to formulate our original scalar field Φ in terms of the VEV, v , and a remaining real scalar field, h , in equation (1.23).

$$\Phi = \frac{1}{\sqrt{2}} \begin{pmatrix} 0 \\ v + h \end{pmatrix} \quad (1.23)$$

To see how these terms generate mass, it is convenient to perform a change of basis from τ^1, τ^2, τ^3 to the τ^+, τ^-, τ^3 representation given by equation (1.24). This change of basis also will change the $W_\mu^1, W_\mu^2, W_\mu^3$ to $W_\mu^+, W_\mu^-, W_\mu^3$ given by equation (1.25).

$$\tau^\pm = \frac{1}{\sqrt{2}} (\tau^1 \pm i\tau^2) \quad (1.24)$$

$$W_\mu^\pm = \frac{1}{\sqrt{2}} (W_\mu^1 \mp iW_\mu^2) \quad (1.25)$$

Looking at the scalar kinetic term of equation (1.21), $|\mathcal{D}_\mu \Phi|^2$, more explicitly we can write the boson terms in the form equation (1.26), dropping terms that represent the dynamics and interactions of the h field.

$$\frac{v^2}{4} (g_2 W_\mu^3 - g_1 B_\mu)^2 + \frac{g_2^2 v^2}{2} W_\mu^+ W_\mu^- \quad (1.26)$$

¹¹As required by the Lorentz invariance of the electromagnetic force

CHAPTER 1. INTRODUCTION

After another change of basis, we can recast the first term in equation (1.26) as the physical gauge fields we observe in nature. In equations (1.27) and (1.28), we see the Z and γ fields we are looking for and the masses of the bosons respectively.

$$\begin{aligned} Z_\mu &= \frac{g_2 W_\mu^3 - g_1 B_\mu}{\sqrt{g_1^2 + g_2^2}} \\ A_\mu &= \frac{g_2 W_\mu^3 + g_1 B_\mu}{\sqrt{g_1^2 + g_2^2}} \end{aligned} \quad (1.27)$$

$$\begin{aligned} m_W &= \frac{v}{\sqrt{2}} g_2 \\ m_Z &= \frac{v}{\sqrt{2}} \sqrt{g_2^2 + g_1^2} \\ m_\gamma &= 0 \end{aligned} \quad (1.28)$$

Thus we have broken the electroweak symmetry, giving the W^\pm and Z bosons mass while keeping the γ massless. This provides a theory that predicts a new field, h , called the *Higgs field*, and allows us to describe the behavior of the weak and electromagnetic forces to fantastic accuracy.

To investigate the ramifications of this new field, we can formulate the h field as small permutations about the VEV. This gives a potential of the form $\phi(x) = v + \frac{1}{\sqrt{2}}(\chi(x) + i\psi(x))$. These permutations are illustrated in figure 1.9. From the

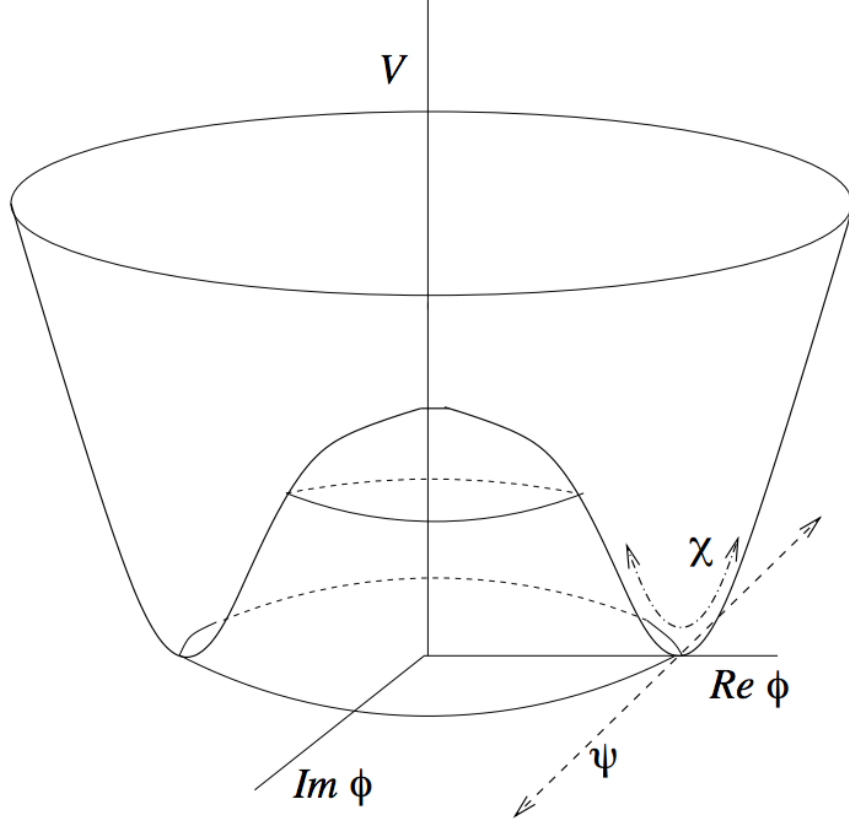


Figure 1.9: A 2D illustration of oscillations in the scalar potential, $V(\Phi)$, parameterized by χ and ψ [25].

figure it is clear that a small displacement in ψ does not cost energy, while oscillations in χ do cost energy. Thus χ corresponds to a new massive boson is called the *Higgs Boson* in common literature. Everything about this new boson can be predicted from the SM, except the two parameters, μ^2 and λ , or equivalently the VEV given in equation (1.29) and the mass of the Higgs Boson in equation (1.30).

$$v^2 = -\frac{\mu^2}{2\lambda} \quad (1.29)$$

$$m_h^2 = 2v^2\lambda \quad (1.30)$$

1.3.3.1 Implications of the Higgs field: Fermion Masses

When we first started our discussion of Fermions we simply wrote the mass of a fermion as $-m\bar{\psi}\psi$ in equation (1.14). However, this term would explicitly break the electroweak gauge invariance we have just spent so much time constructing. It turns out that the new scalar field h could also be responsible for the fermion masses in addition to the W^\pm and Z masses. The term can be created by considering a Yukawa coupling between the scalar field and a fermion field. For the down quark this term follows equations (1.31)¹².

$$\begin{aligned} \mathcal{L}_{d\text{-mass}} &= -\lambda_d \bar{Q}_L \Phi d_R + h.c. \\ &= \frac{-\lambda_d}{\sqrt{2}} \begin{pmatrix} \bar{u}_L & \bar{d}_L \end{pmatrix} \begin{pmatrix} 0 \\ v+h \end{pmatrix} d_R + h.c. \\ &= \frac{-\lambda_d v}{\sqrt{2}} \bar{d}_L d_R + h.c. \end{aligned} \quad (1.31)$$

Where the final equality comes from focusing on the terms that remain in the ground state of the scalar potential. From here its easy to see that the mass of the down quarks can be obtained from the vacuum expectation value of the scalar field

¹²In these equations h.c. stands for the hermitian conjugate term.

CHAPTER 1. INTRODUCTION

and the down coupling to the Higgs field, λ_d .

$$m_d = \frac{\lambda_d v}{\sqrt{2}}$$

The masses of the other fermions follow from equations similar to (1.31) where the Higgs field, h , interacts with all the fermions. This will be the key to generating Higgs bosons at the LHC, particularly Higgs couplings to top quarks.

It seems that the Higgs Mechanism and the Higgs boson solve many of the issues that the SM has with describing the world we observe. However, there are many other unexplained phenomena in the universe and detailed study of the Higgs mechanism could lead unearth the origin of these discrepancies. The next subsection is an outline some of these discrepancies that will be discussed in this document.

1.4 Limitations of the SM: Higgs boson as a tool

The SM has been one of the most successful scientific theories ever proposed. The predictive power of the model is unparalleled, yet some questions remain. The first limitation we will discuss in this section will be the matter-antimatter asymmetry seen in the universe around us. Secondly, a discussion of the SM's inability to accurately

CHAPTER 1. INTRODUCTION

describe gravity is presented. Finally, generalizations of the SM are discussed. These models that could generate the dark matter seen in astronomical measurements, solve the hierarchy problem, or explain more about fermions. The Higgs field could offer keys to understanding all of these issues and the tests presented in this document are intended to address these questions.

1.4.1 *CP*-violation: The Matter-Antimatter Asymmetry

Outside of specific particle physics experiments, the universe we live in is dominated by matter. It seems that only a very small fraction of antimatter exists in the universe. However, within specific tests of SM no process is observed to generate this large of a discrepancy between matter and antimatter. Under the assumption that matter and antimatter started in equal amounts, after the Big Bang, matter and antimatter should still exist in relatively equal densities and amounts. The SM does not predict, nor has any experiment seen, a process that could generate enough *CP*-violation to create a universe that is so overwhelmingly dominated by matter.

So far we have only eluded to *CP* transformations when introducing the antiparticles that exist in the SM. In the most basic terms this is the combination of two discrete symmetries *charge conjugation* and *parity symmetry* (spatial inversion). The parity operation, P , is the spatial inversion through the origin. We saw the projec-

CHAPTER 1. INTRODUCTION

tions of a fermion onto the eigenstates of this operation at the end of section 1.1.3.

If $\psi(x)$ describes a fermion field at point x , then $P\psi(x) \rightarrow \psi(-x)$. This transformation will take $x \rightarrow -x$ and the momentum $p \rightarrow -p$ but leave the inherent spin and other quantum numbers unchanged. The charge conjugation operation, C , is the transformation of a particle to its antiparticle or vice versa. We used this transformation extensively in 1.3 but never wrote out the transformations explicitly. As an example, given an electron, e^- , then $Ce^- \rightarrow e^+$. This transformation will reverse the sign of all quantum numbers associated with the particle (inherent spin, weak isospin, charge, hypercharge, etc...). Particles that are their own antiparticle (π^0 meson, ν 's, ...) remain unchanged under this operator (aside from a possible factor of -1).

Not all interactions allowed by the standard model will preserve these symmetries. The most explicit example is the weak interaction. Given that the weak force only interacts with left-handed particles, it is maximally parity violating¹³. However, in most cases CP together is a symmetry of the interactions. The notable exceptions to this are the decays of B mesons and Kaons [26]. These decays highlight the necessity for a CP -violating component in the SM described by the Cabibbo-Kobayashi-Moskawa Model [27]. The specifics of this model are beyond the scope of this document. However, the observed magnitudes of the terms in the CKM model cannot account for the large discrepancy that we observe in the universe.

One proposed solution to this asymmetry is the presence of more than one Higgs

¹³Imagine a stationary pseudoscalar π^+ decaying into back-to-back μ^+ and ν_μ states via the weak interaction. Perform the parity operation on the initial and final states. The result requires a right-handed neutrino, which are unobserved.

CHAPTER 1. INTRODUCTION

field, resulting in multiple Higgs bosons. The number of fields and bosons predicted varies depending to the model and any observed boson could have varied spin (J), charge (C), and parity (P) transformation properties. It could be charged, neutral, pure scalar, pure pseudoscalar, vector, pseudovector or a mixed vector-pseudovector state. In this document we outline tests proposed and performed to test the J^{CP} nature of a boson to see if a Higgs boson can offer any insights into the nature of the matter-antimatter asymmetry.

1.4.2 The Graviton: An Unexplained Force

Gravity would be the weakest of all the forces we know of but it is not yet included in the SM. There are many possible theories of gravity at small scales and its corresponding boson, the *graviton*. In Table 1.2 you can find a summary of the different forces and their relative strengths and interaction ranges, including gravity. Since gravity is so intimately connected with the mass of an object in relativistic mechanics it is expected to have similar couplings to the SM particles as the Higgs boson, but to match general relativity most theories claim that it must be a spin-2 particle. Generally, most theories predict that a graviton would be a massless particle to have an infinite interaction range. There is always the possibility of new physics spoiling our expectations so a detailed study of any new scalar particle found should be performed to determine if the spin is zero (as predicted by Higgs boson) or two (as predicted by a Beyond SM graviton).

CHAPTER 1. INTRODUCTION

In this analysis, we study a few possibilities for a graviton-like particle. This is discussed in more detail in section 3.4.3, but generally we consider a Kaluza-Klein theories where a closed fifth dimension could give rise to a massive spin two graviton [28]. Exact definitions of the models tested, and references motivating them can be found in section 3.4.3.

1.4.3 Beyond the SM: The Dark Matter, Hierarchy & Fermion Problems

It has not been explicitly expressed in our discussion of SM phenomena but everything that we understand about the universe is really only valid at masses up to a certain scale ($\sim m_{W/Z}$). Using current models of the early universe, at early times we know that the energies are many orders of magnitude larger than what our SM theory can describe [29]. Many extensions of the SM to these high energies have been proposed and generally we will call them Beyond SM (BSM) theories in this document. These theories predict varied and wide ranging possibilities for new particles and physics and could be tested by examining a Higgs boson. Some BSM theories predict particles that could exist in relative obscurity on Earth but could be the *dark matter* observed in astronomical experiments [30].

Currently there is no explanation for why gravity is so much weaker, table 1.2, than the other forces. The SM requires a very specific values in order to explain this

CHAPTER 1. INTRODUCTION

difference without theoretical motivation. This is called the *hierarchy problem* of the SM. BSM theories offer natural solutions to this problem sometimes simultaneously with explanations for the dark matter abundance. Other issues that can be explained through BSM theories include the number of fermion generations and their masses. In principle, there is no preference for only three generations of fermions and not motivation for the specific masses of these particles.

Generally, BSM theories can come in almost any type imaginable. If these new particles interact with the scalar Φ field, then they could be seen as a deviation from the expected couplings (interactions) with SM particles. These deviations could take many forms, but those tested in this document include: Unusual production mechanisms, unexpected spin-parity behavior, and enhanced non-resonant production.

Chapter 2

The Experiment: LHC and CMS

In order to answer questions about the Standard Model (SM) we need to observe processes that are extremely rare in the universe. Many measurements to test the limits of the SM can be performed by observing nature. However, to test questions about the Higgs boson, waiting for events to happen naturally would take an extremely long time¹. To study these processes, labs around the world create particle colliders to generate interesting phenomenon more frequently than nature would. The rate that any physics process will occur (at a collider or otherwise) is given by the effective area of the process, *cross section* (σ), and rate those reagents pass through the same area, *luminosity* (\mathcal{L}); equation (2.1).

$$\frac{dN}{dt} = \mathcal{L} \cdot \sigma \quad (2.1)$$

¹In many cases much longer than the age of the universe.

CHAPTER 2. THE EXPERIMENT: LHC AND CMS

The cross section for a process is the effective area of the reagents to interact in a specific way. A cross section can describe a particular number of final particles, or a specific boson used for the interaction, etc. Cross sections change depending on the energy of the interacting particles, and are usually given in units of *barns* ($b = 10^{-24} \text{ cm}^{-2}$). They can be computed using the scattering amplitudes we have already introduced in section 1.2.

The luminosity is a measure characterizing the source of the reagents, with units that are typically $\text{cm}^{-2}\text{s}^{-1}$. We will discuss the particulars of this quantity for colliders, but generally luminosity is a measure of the flux of particles at a particular point in space and time.

When a particle physics experiment is designed, first numerous factors dictate what kind of particles you will accelerate and collide together. Once you have decided this, two properties define its ability to test the limits of the SM; the luminosity and the center of mass energy. With specific center of mass energies we can probe cross sections that are typically small at everyday energies. Using a higher luminosity we can increase the rate of rare events by generating interactions more often.

2.1 The Large Hadron Collider (LHC)

The Large Hadron Collider (LHC) is the largest and most powerful of these experiments in the world. It is located on the border between France and Switzerland

CHAPTER 2. THE EXPERIMENT: LHC AND CMS

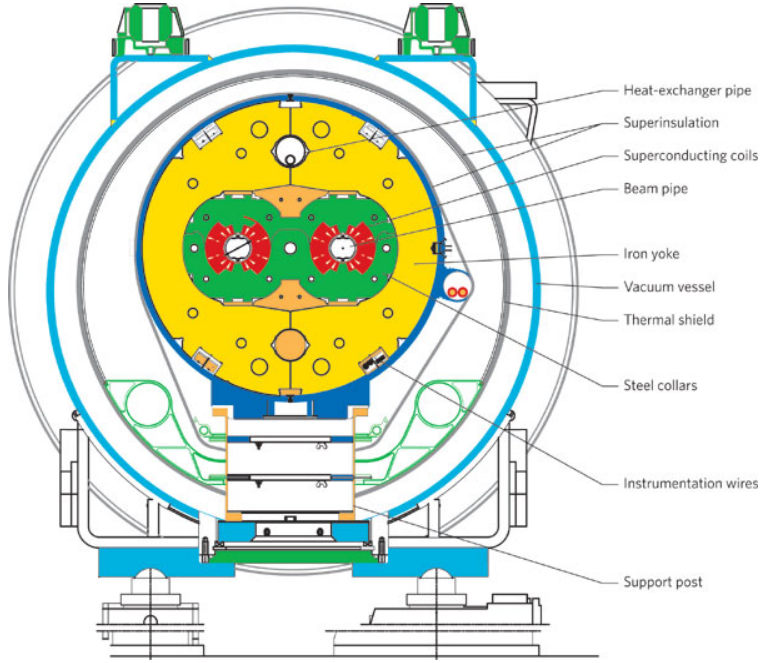


Figure 2.1: A cross section schematic of the LHC Dipole magnet showing the two center beam pipes, superconducting coils (red), and other supporting structures [31].

just outside the city of Genvève at CERN². The LHC is a superconducting proton accelerator and collider measuring 27 km in circumference, approximately ~ 100 m underground. It first accelerates, then collides two beams of protons circulating the ring in opposite directions³. These protons are circulated using 1232 dipole ‘bending’ superconducting magnets and a series of other quadrupoles, sextupoles, octupoles, decapoles, etc. used for controlling and focusing the beams. The layout of the dipole magnets is shown in figure 2.1 where the two beam pipes are shown along with the other magnetic, vacuum, and shielding structures.

²European Organization for Nuclear Research or Conseil Européen pour la Recherche Nucléaire

³The LHC also collides Lead ions with each other and protons, but those studies are beyond the scope of this document.

CHAPTER 2. THE EXPERIMENT: LHC AND CMS

The LHC probes small cross sections by smashing two beams of high energy protons into each-other giving large center of mass energies. In the original design, each proton beam would have 7 TeV of energy giving 14 TeV in the center of mass frame. However, these studies will focus on the early years of LHC operation where the center of mass energies were 7 TeV (2011) and 8 TeV (2012).

The luminosity of the LHC depends on the geometrical and electrodynamic parameters of the beam. For a beam of particles that are Gaussian distributed, the luminosity is given by the product of the beam current ($f_{\text{rev}}n_bN_b$), brightness $\left(\frac{N_b}{\epsilon_N}\right)$, energy $\left(\frac{\gamma}{\beta^*}\right)$ and a geometric reduction factor (F):

$$\mathcal{L} = \frac{1}{4\pi} \cdot (f_{\text{rev}}n_bN_b) \cdot \frac{N_b}{\epsilon_N} \cdot \frac{\gamma}{\beta^*} \cdot F. \quad (2.2)$$

In this equation (2.2) the relevant factors that determine the beam current are the revolution frequency, (f_{rev}), the number of proton bunches in each beam, (n_b), and the number of protons in each bunch, (N_b). Generally, the LHC tries to maximize this beam current so that the number of protons in each beam is as large as possible. The brightness of the beam determines how likely two protons are to interact when one bunch crosses another. It is determined by the number of protons in a bunch and the normalized transverse beam emittance, (ϵ_n), which is a measure of the area of the beam in the position-momentum phase space. The energy of the beam is determined by the relativistic γ factor and the value of the beta function at the collision point, (β^*). The beta function describes transverse size of the beam and $*$ denotes that

CHAPTER 2. THE EXPERIMENT: LHC AND CMS

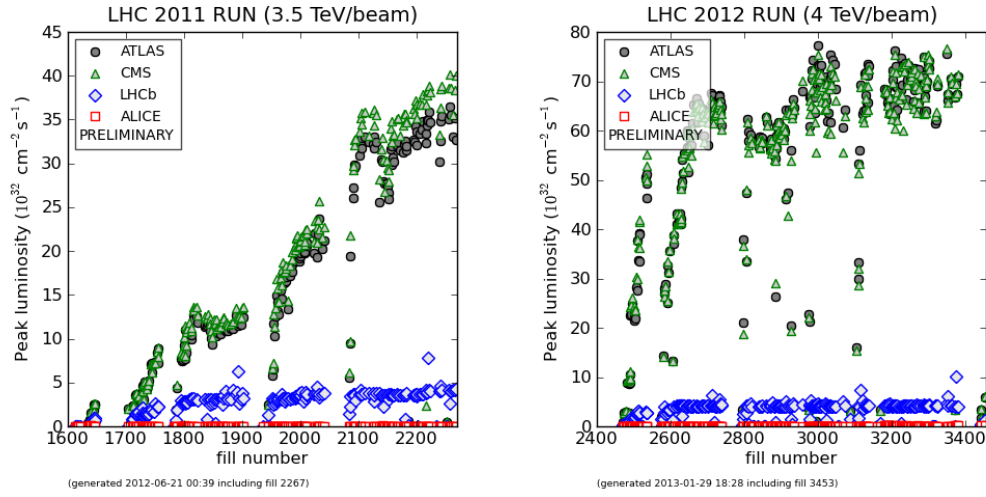


Figure 2.2: The peak luminosity delivered to the four main LHC experiments during the 2011 7 TeV (left) and 2012 8 TeV (right) runs [32].

this function should be evaluated at the collision point. The final term, (F), is the geometrical factor that describes the reduction in luminosity because the two beams cross each-other with some non-zero angle between them.

For the experiments that require the highest luminosities, the LHC was designed to provide $10^{34} \text{ cm}^{-2}\text{s}^{-1}$. The machine ran at lower luminosities for the first few years of operation as seen in the figures 2.2 [32].

To get the protons up to the necessary energies, protons are accelerated through a series of smaller accelerators which are pictured in figure 2.3. The process starts with the 50 MeV LINAC2 which shoots the protons into a multi-ring booster synchrotron that accelerates them up to 1.4 GeV. Next the protons are directed to the Proton Synchrotron (PS) machine which accelerates them up to 26 GeV and generates the bunching and spacing that the LHC uses. To accelerate the beam from 26 GeV up

CHAPTER 2. THE EXPERIMENT: LHC AND CMS

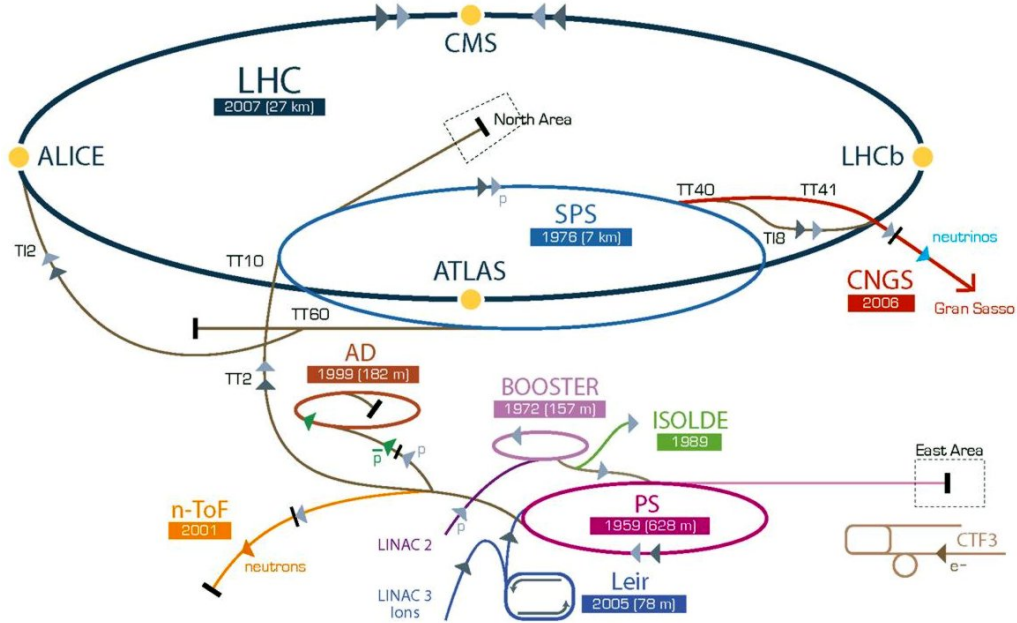


Figure 2.3: This CERN accelerator complex. Showing the full chain of accelerators used for the LHC protons: LINAC2, Booster, PS, SPS, and LHC. Additionally, the four large experiments on the LHC are shown: ALICE, ATLAS, CMS, LHCb [33].

to 450 GeV the beam is fed into the Super Proton Synchrotron (SPS). From the SPS the protons are fed into one of the LHC rings. Before the LHC accelerates these protons up to their final energies, this process is repeated 24 times, 12 to fill each of the two rings. Once the LHC has accelerated these proton bunches to their final energies, the beams are gradually brought together so that they will collide inside the four experiments.

The particle physics community built detectors to observe and categorize the particles that are produced when these protons (ions) are collided with each-other. Currently there are four experiments at the LHC: A Toroidal LHC ApparatuS (ATLAS), the Compact Muon Solenoid (CMS), A Large Ion Collider Experiment (ALICE), and

CHAPTER 2. THE EXPERIMENT: LHC AND CMS

Large Hadron Collider beauty (LHCb). The ATLAS and CMS detectors are high luminosity, multi-purpose detectors designed to test many different aspects of the SM, including the Higgs boson. LHCb looks specifically at bottom (beauty) quark interactions, while ALICE is designed for ion collisions. This work took place at the CMS experiment, described in the next sections.

2.2 The Compact Muon Solenoid (CMS)

The Compact Muon Solenoid (CMS) experiment is one of the two largest experiments on the LHC. The general goal of the CMS experiment is to collect and study as many interesting events from LHC collisions as possible. To do this, CMS must identify interesting physics events and reconstruct these events as accurately as possible. At the designed energy and luminosity the LHC is expected to create ~ 1 billion collision events per second. It would not be possible to reconstruct all of these events, so CMS has an extensive online event selection process, called the ‘Trigger’, that reduces this to about 100 events per second. Some details of this process are presented in section 2.3, but we will first have a discussion of the different CMS subdetectors.

To quantify how much data CMS has collected we use *integrated luminosity*, which is the time integral of the luminosity, $\int \mathcal{L} dt$. This value tells experimenters how many events to expect for the specific processes they study, $N = \sigma \cdot \int \mathcal{L} dt$, and allows them to test smaller and smaller cross sections. Over the 2011 and 2012 runs⁴ of the CMS

⁴A run is a period of time denoting specific conditions for the detector or LHC.

CHAPTER 2. THE EXPERIMENT: LHC AND CMS

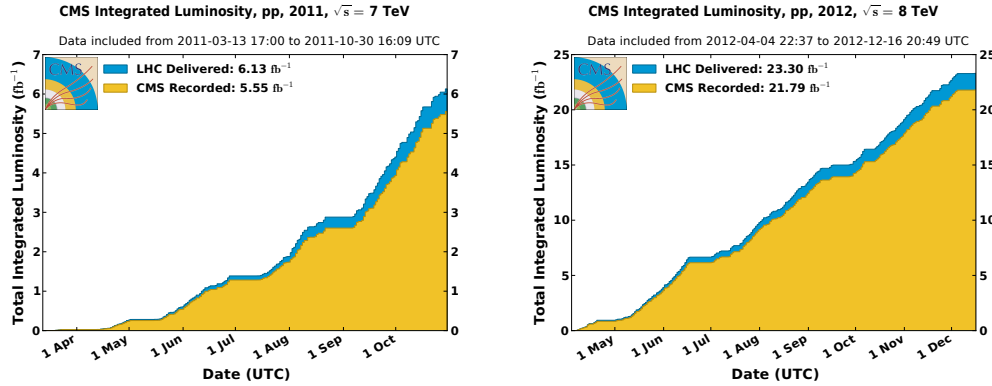


Figure 2.4: The integrated luminosity delivered and collected by the CMS experiment during the 2011 7 TeV (left) and 2012 8 TeV (right) runs, [34].

detector collected 5.1 fb^{-1} and 19.7 fb^{-1} of integrated luminosity respectively, shown in figure 2.4.

To maximize the physics results that can be pulled from this data, CMS was designed with key features that give credence to its name. While it may seem oxymoronic to call a 21.6 m long and 15 m in diameter experiment ‘compact’, the name is fitting because it is designed to put the sub-detectors within CMS close together. This compact design is a result of the 4 T magnetic field that is the heart of the CMS detector. The Magnet, discussed more in section 2.2.1, causes the charged particles generated in collisions to bend as they flow out from the interaction point so identifying particles and measuring their momentum requires detectors that are close together. Working in concert with this field, the CMS detectors are designed to fit together as a ‘cylindrical onion’. The layers of detectors and sub-detectors radiate outward from the point where the proton collisions take place. Each layer is designed to maxi-

CHAPTER 2. THE EXPERIMENT: LHC AND CMS

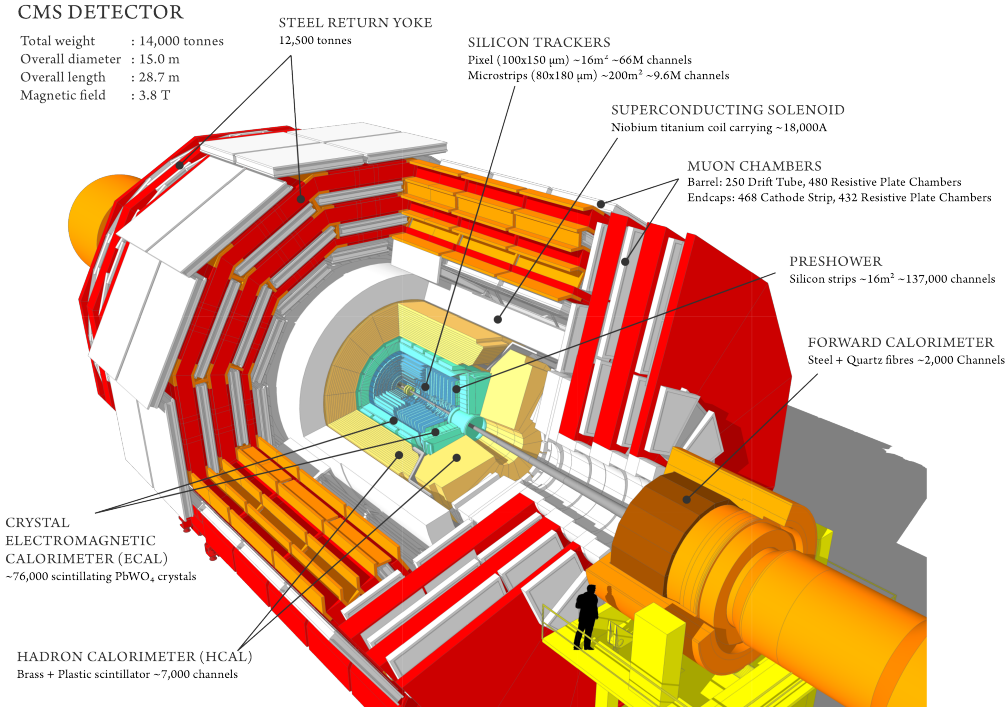


Figure 2.5: Sectional view of the CMS detector. The LHC beams travel in opposite directions along the central axis of the CMS cylinder colliding in the middle of the CMS detector [36].

mize the physics information that can be obtained at different distances from these collisions. The majority of the information in this section follows [35].

A sectional view of the CMS detectors can be seen in figure 2.5. From this image you can see a summary of the different subdetectors that we discuss from inside out. The innermost detector is the Silicon tracker, discussed in section 2.2.2, this detector is designed to give good momentum resolution for charged particles and high reconstruction efficiency requiring precise alignment of the tracking system. Additionally, this tracker needs to be able to efficiently tag τ 's and b's, which will have a displaced vertex due to their long lifetimes. This requires pixel detectors close

CHAPTER 2. THE EXPERIMENT: LHC AND CMS

to the interaction point.

Just outside of the tracking system is the Electromagnetic calorimeter (ECAL), discussed in section 2.2.3, which gives good energy and mass resolution for photons and electrons and wide geometric coverage. Further, the high segmentation of the system allows for great directional discrimination to determine the origin of the particles and to determine how isolated they are from other particles.

The final detector that still lies inside the bore of the solenoid is the Hadronic Calorimeter (HCAL), described in section 2.2.4. This detector allows for accurate measurements of quark-jet mass resolution and the lateral segmentation gives directional information that is key to determine any imbalance in the transverse energy of a collision, E_T^{miss} .

Outside of the solenoid magnet lies the Muon System, described in section 2.2.5, and the large Iron return yokes. This is the largest and heaviest part of the CMS detector⁵. This system gives good muon identification and good momentum resolution over a wide range of angles and energies for high momentum muons.

As we describe the CMS detector we will need to define a set of spacial coordinates so that we can locate ourselves within the detector. The coordinate system is defined to put the origin at the nominal collision point inside the experiment, the y-axis pointing vertically upward, the x-axis pointing along the radius of the LHC, and the z-axis pointing along the beam direction. The geometry of the detector is already

⁵When combined with the magnet and other subdetectors the full CMS detector weighs $\sim 14,000$ tonnes.

CHAPTER 2. THE EXPERIMENT: LHC AND CMS

cylindrical, so a modified form of cylindrical units are used for most studies. The azimuthal angle ϕ , is given by the angle from the x-axis in the x-y plane. The polar angle, θ (from the z-axis), normally used in cylindrical coordinates, is replaced by the pseudorapidity, $\eta = -\ln \tan(\theta/2)$. The z-axis is the same as the cartesian definition. Often, interesting physics events will show distinct features in the momentum or energy transverse to the beam direction, p_T and E_T respectively.

2.2.1 The Magnet

The defining feature of CMS is the superconducting solenoid magnet, the parameters are given in table 2.1. The large bending power that CMS is designed for is obtained from a reasonably-sized superconducting solenoid where the bending for charged particles starts at the primary vertex. The strong field is needed to give good momentum resolution. It bends muons tightly so that the charge is unambiguous and giving a momentum resolution of $\Delta p/p \sim 10\%$ at $p = 1 \text{ TeV}/c$. This design also leads to a reasonable field in the forward region where many of the detected particles will be.

The magnet itself is constructed from high-purity aluminum-stabilized conductor and is indirectly cooled using a thermosiphon method. While this type of magnet has been used at other experiments, it was a large step up in many aspects from previous magnets. To create a solenoid with the field and dimensions, a four-layer conductive winding with a large diameter wire was used so it could withstand the

CHAPTER 2. THE EXPERIMENT: LHC AND CMS

Field	4 T
Inner Bore	5.9 m
Length	12.9 m
Number of Turns	2168
Current	19.5 kA
Stored Energy	2.7 GJ
Hoop stress	64 atm

Table 2.1: Parameters of the CMS superconducting solenoid, [35].

large outward pressure (hoop stress). The conductor carries a 19.5 kA current and is co-extruded with pure and alloy aluminum to stabilize it thermally and mechanically. The conductor was manufactured in twenty continuous lengths, each of 2.65 km. Four of these lengths were used to make each of the five coil modules within the magnet.

Working in concert with the magnet is the iron return yoke of the muon system. As can be seen in figure 2.6, the superconducting magnet generates a large magnetic field inside the solenoid while the return flux of the field concentrates itself in the large iron structures that house the different muon detectors. These performance predictions were later confirmed by both monitors installed in the detector and with data collected from cosmic rays [37].

CHAPTER 2. THE EXPERIMENT: LHC AND CMS

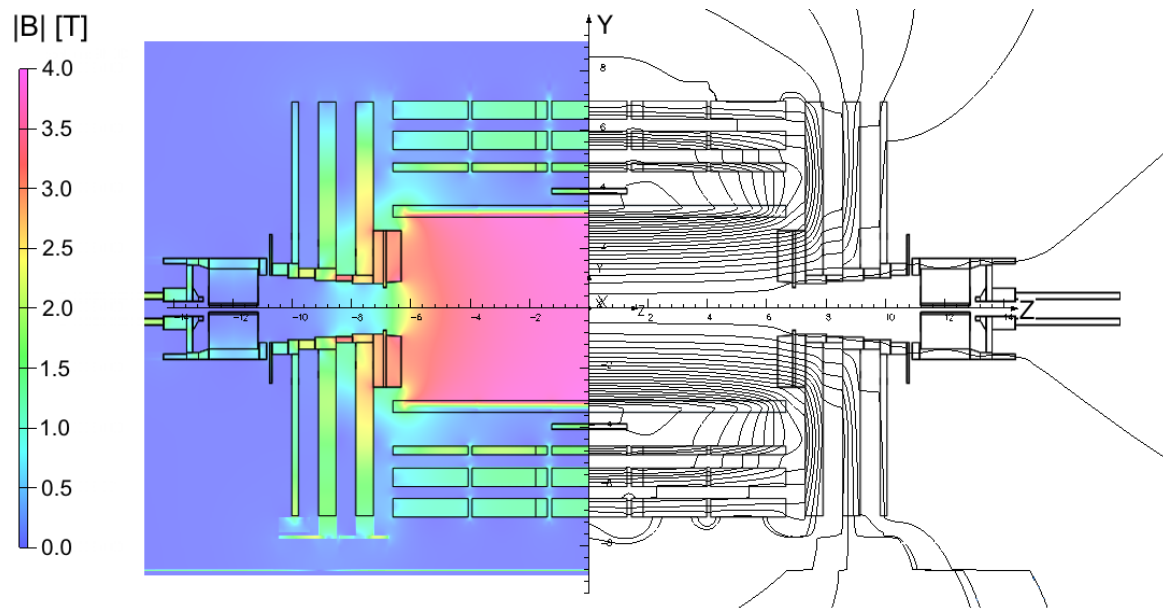


Figure 2.6: Value of magnetic field $|B|$ (left) and field lines (right) predicted on a longitudinal section of the CMS detector, for the underground model at a central magnetic flux density of 3.8 T. Each field line represents a magnetic flux increment of 6 Wb [37].

2.2.2 The Inner Tracker System

The inner tracker system is the first detector that a particle generated from an LHC collision will encounter. At the LHC, determining the origin of these particles is key and made more difficult due to the small gaps between proton bunches. The spatial resolution of the silicon tracker detector allows a particle to be mapped to the primary collision vertex (*primary vertex*), secondary vertices, or identify them as *pileup events*. At the designed luminosity, the LHC is expected to generate about 20 collisions⁶ that will all be superimposed on an event of interest. This means that ~ 1000 charged particles will appear in the detector for every interesting event. The job of the inner tracker is to measure the charge and momentum of these particles, and determine which of these originate from what vertex. To do this, the tracker has two distinct types of detectors; the 66 million *silicon pixels* and 9.6 million *silicon strips*. It is also vital that the positions of these detectors is accurately known at all times so that the system can operate at its ideal level. The process of determining the positions of these detectors is called *Tracker Alignment* and an overview of work performed for this task is presented.

2.2.2.1 Pixel Tracker

Close to the interaction vertex the tracker consists of three layers of silicon pixel modules in the barrel region and two layers of silicon pixel modules in each forward

⁶We expect more moving forward.

CHAPTER 2. THE EXPERIMENT: LHC AND CMS

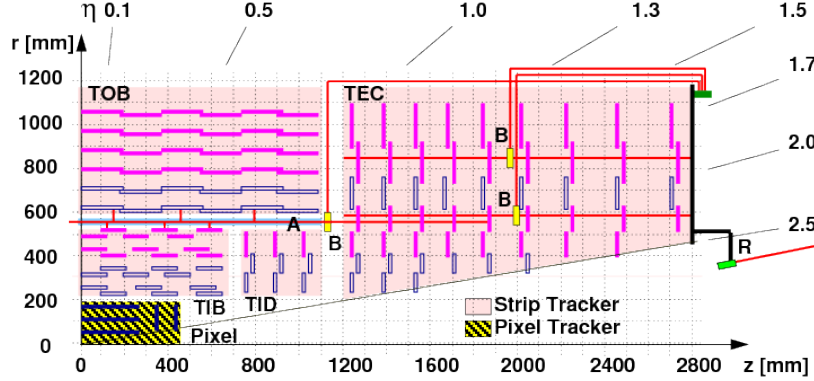


Figure 2.7: Schematic view of one quarter of the silicon tracker in the r - z plane. The positions of the pixel modules are indicated within the hatched area. At larger radii within the lightly shaded areas, solid rectangles represent single strip modules, while hollow rectangles indicate pairs of strip modules mounted back-to-back with a relative stereo angle [38].

region. The layout of the pixel detector is shown in figure 2.8. Each of the three barrel layers are located at radii 4.4 cm, 7.3 cm, and 10.2 cm from the nominal interaction point and each is 53 cm long. On either side of the three barrel layers are two end disks placed at $|z| = 34.5$ cm and 46.5 cm.

All of the pixel modules start from the same base array (52 column \times 80 row) of pixels (size: $100 \mu\text{m} \times 150 \mu\text{m}$) bump-bonded to a readout chip (ROC). Each pixel is connected to its own amplifier, shaper, and comparator (including an individual 3-bit DAC threshold) which is connected to a ‘double-column’ group shown in figure 2.9. The periphery of each double-column contains a data buffer, timestamp, and corresponding control and readout electronics. ROC’s are grouped into modules. Each module has a different number of ROCs depending on the geometry of the region where the detectors are placed.

CHAPTER 2. THE EXPERIMENT: LHC AND CMS

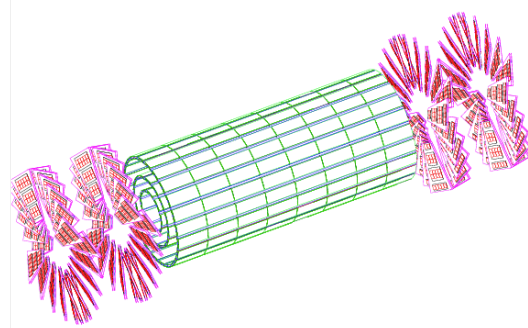


Figure 2.8: Layout of the pixel detectors in the CMS tracker [35].

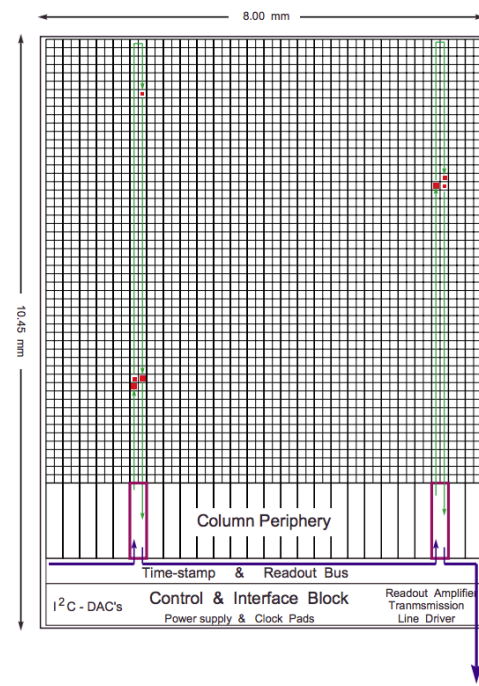


Figure 2.9: Layout of the pixel sensor in the CMS tracker [39].

CHAPTER 2. THE EXPERIMENT: LHC AND CMS

The pixel barrel (BPIX) contains 768 modules grouped into three layers⁷ and two *half-barrels*⁸. While the forward pixel detectors (FPIX) are made from 672 modules grouped into two layers of turbine-like blades. The forward structures are also grouped into *half-cylinders* similar to the barrel region⁹. Both the barrel layers and the blades are oriented to benefit from the large Lorentz effect (charge drift in a magnetic field) that increases the resolution through charge sharing between the pixels.

In the end, the inner tracker comprises 66 million individual pixel channels readout using approximately 16000 ROCs, giving a spatial resolution of about $\sim 10 \mu\text{m}$ in $r\text{-}\phi$ and $20 \mu\text{m}$ in z . This high resolution allows for precise momentum determination for particles as they curl in the high magnetic field. It is also key to determining the origin of the particles that CMS measures. The $\sim 1 \text{ m}^2$ silicon pixel detector provides coverage up to $|\eta| < 2.4$.

2.2.2.2 Strip Tracker

Much larger than the pixel tracker is the $\sim 200 \text{ m}^2$ silicon strip tracker. The strip tracker is divided into four parts: TIB (tracker inner barrel), TID (tracker inner disks), TOB (tracker outer barrel), and TEC (tracker end cap). The CMS tracker is the largest silicon detector ever built. Different regions of the strip tracking system have different module types summarized in table 2.2. All together, the Silicon Strip

⁷There are smaller substructures within each layer.

⁸All three layers together make one half-barrel.

⁹Again, the two layers together make the half-cylinders.

CHAPTER 2. THE EXPERIMENT: LHC AND CMS

part	No. detectors	thickness (μm)	mean pitch (μm)
TIB	2724	320	81/118
TOB	5208	500	81/183
TID	816	320	97/128/143
TEC(inner)	2512	320	96/126/128/143
TEC(outer)	3888	500	143/158/183

Table 2.2: Detector types in the silicon strip tracker, [35].

Tracker has complete coverage up to $|\eta| < 2.4$.

In the barrel region the coverage for the TIB and TOB is very different. The TIB has four layers and covers $|z| < 65$ cm with silicon sensor of a thickness of 320 μm . The first two layers are made with “stereo” modules in order to provide both $r\text{-}\phi$ and $r\text{-}z$ measurements. These stereo modules are made with a stereo angle of 100 mrad giving the TIB single-point resolution of 23-34 μm in $r\text{-}\phi$ and 23 μm in z . The TOB has six layers covering $|z| < 110$ cm with silicon sensor of a thickness of 500 μm . The first two layers of the TOB are also stereo modules with a stereo angle of 100 mrad. This gives the whole TOB a resolution of 35-52 μm in $r\text{-}\phi$ and 52 μm in z .

The each of the two TECs comprises nine disks that cover the $120 \text{ cm} < |z| < 280 \text{ cm}$ forward region. While the TID covers the gap between the TIB and the TEC. Both the TID and TEC modules are arranged in rings centered at the beam line. The strips in these sensors radiate outward from the beam line so the pitch is different for each strip. The first two rings of the TID and the first, second, and fifth rings of the TEC are stereo modules as well allowing for more precise resolution. The TID

CHAPTER 2. THE EXPERIMENT: LHC AND CMS

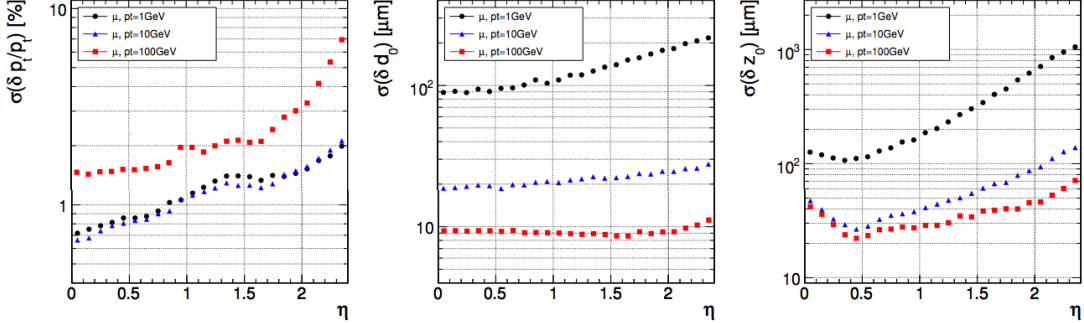


Figure 2.10: Predicted resolution of several track parameters for single muons with 1, 10, and 100 GeV: transverse momentum (left), transverse impact parameter (center), and longitudinal impact parameter (right). [40].

and first three rings for the TEC have 320 μm sensors while the rest of the TEC has 500 μm sensors.

All of these structures (BPIX, FPIX, TIB, TOB, TID, TEC) are mounted in carbon-fiber structures and are cooled to ensure they operate correctly for a long time¹⁰. Using the precise position information that the tracker provides CMS is able to determine with very high confidence the momentum and impact parameter (How close a particle's path is to the origin.) of particles, see figure 2.10. Careful consideration is taken when these detectors are moved and installed but precise determination of the exact location of all components is key to keep the optimal resolution of these detectors. This process is not only vital during the LHC startup but care needs to be taken as the detector takes data to ensure no loss in performance.

¹⁰Because of technical problems during run 1 the detectors were not kept as cold as originally designed.

2.2.3 Electromagnetic Calorimeter

The CMS Electromagnetic Calorimeter (ECAL) is composed of 61200 lead tungstate (PbWO_4) crystals mounted in the barrel part of the detector and 7324 crystals in each of the two end caps. Together the barrel and end caps make a homogeneous and hermetic scintillating layer surrounding the Inner Tracker. The crystals were chosen to have short radiation and Moliere lengths while being fast radiation hard scintillators. Due to the low light yield of the crystal, silicon avalanche photo diodes (barrel) or vacuum phototriodes (end cap) are used because they can operate in the magnetic field. Additionally, to stabilize the response of the crystals and photo diodes a cooling system is used to maintain temperature stability. Thus, the ECAL is a compact calorimeter that is fast, has fine granularity, and is radiation resistant.

The ECAL barrel section (EB) has an inner radius of 129 cm and constructed as 36 identical “supermodules” each covering half the barrel length and covering a range of $0 < |\eta| < 1.479$. The crystals are installed to be quasi-projective (axis tilted 3°) to the nominal vertex arranged in an $\eta\text{-}\phi$ grid. They have a front face cross-section of $22 \times 22 \text{ m}^2$ and a length of 230 mm.

The ECAL end caps (EE) lie at a distance of 314 cm from the vertex and cover a range of $1.479 < |\eta| < 3.0$. The end cap crystals, like the barrel, are off-point from the nominal vertex but are arranged in an $x\text{-}y$ grid. They have a larger face size than the barrel crystals, $28.6 \times 28.6 \text{ m}^2$ and a length of 220 mm. Additionally, a preshower detector is placed in front of the EE consisting of two planes of silicon strip detectors

CHAPTER 2. THE EXPERIMENT: LHC AND CMS

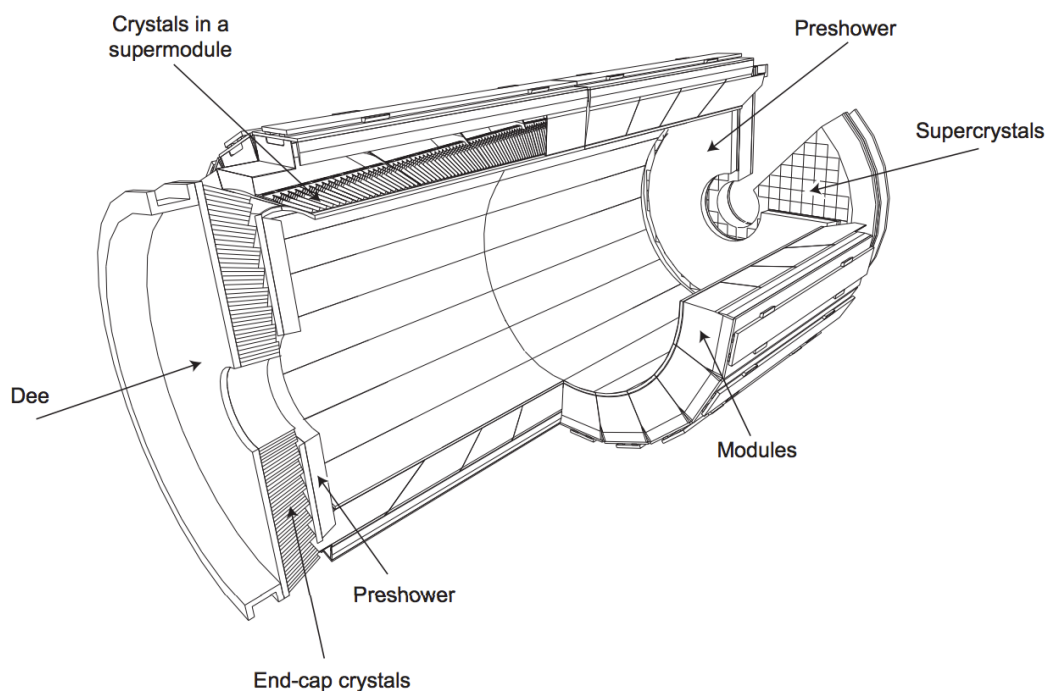


Figure 2.11: Layout of the CMS electromagnetic calorimeter showing the arrangement of crystal modules, supermodules and end caps, with the preshower in front. [40].

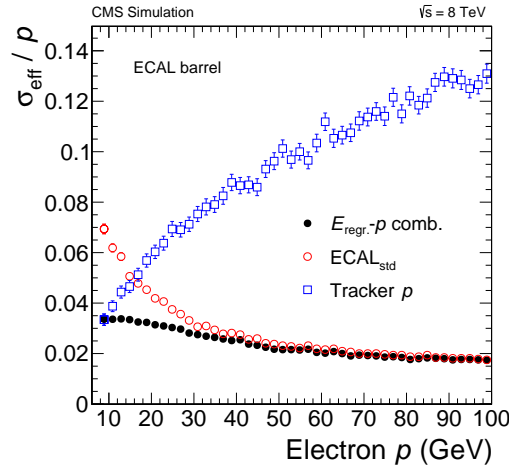


Figure 2.12: Effective momentum resolution σ_{eff}/p for electrons in the EB as a function of the momentum for the ECAL-only, the tracker-only, and the combined estimates. [41].

each placed behind a layer of lead absorber disks.

While the specifics of particle reconstruction are discussed in section 2.3, figure 2.12 shows the electron resolution of the EB system compared to and then combined with the inner tracker system.

2.2.4 Hadronic Calorimeter

The design of the hadron calorimeter (HCAL) is strongly influenced by the choice of magnet parameters because most of the system is located inside the magnet coil and surrounds the ECAL system [35]. The HCAL system consists of a set of sampling calorimeters. The barrel (HB) and endcap (HE) calorimeters utilize alternating layers of brass as absorber and plastic scintillator as active material. The scintillation light

CHAPTER 2. THE EXPERIMENT: LHC AND CMS

is converted by wavelength-shifting fibers embedded in the scintillator and channeled to hybrid photodiode detectors via clear fibers. The outer calorimeter (HO) uses the CMS magnet and return yoke as the absorber while using the same active material and readout system as HB and HE. The HO system serves as a “tail-catcher” after the magnet oil, thus reducing the tails in the energy resolution function.

The HCAL is segmented into individual calorimeter cells along three coordinates, η , ϕ , and depth. The depth is an integer coordinate that enumerates the segmentation longitudinally, along the direction from the venter of the nominal interaction region. The layout of the system can be seen in figure 2.13. The HB system covers the region $-1.4 < \eta < 1.4$ constructed in 2 half barrels. The HE covers the region $1.3 < |\eta| < 3.0$, the segmentation is not uniform in order to maintain coverage and resolution.

Coverage between $3.0 < |\eta| < 5.0$ is provided by the steel/quartz fiber hadron forward (HF) calorimeter. HF is unique in that it preferentially samples the neutral component of the hadron shower. This design leads to narrower showers and hence is ideally suited for the congested environment of the forward region. The HF detector is located outside of the muon system, 11.2 m from the interaction point. Unlike the scintillator that is used in the other HCAL systems, HF uses Cerenkov light emitted in the quartz fibers lay parallel to the beam and are placed in a square grid inside steel plates.

What is actually measured by the HCAL system are particle jets. This is a result of

CHAPTER 2. THE EXPERIMENT: LHC AND CMS

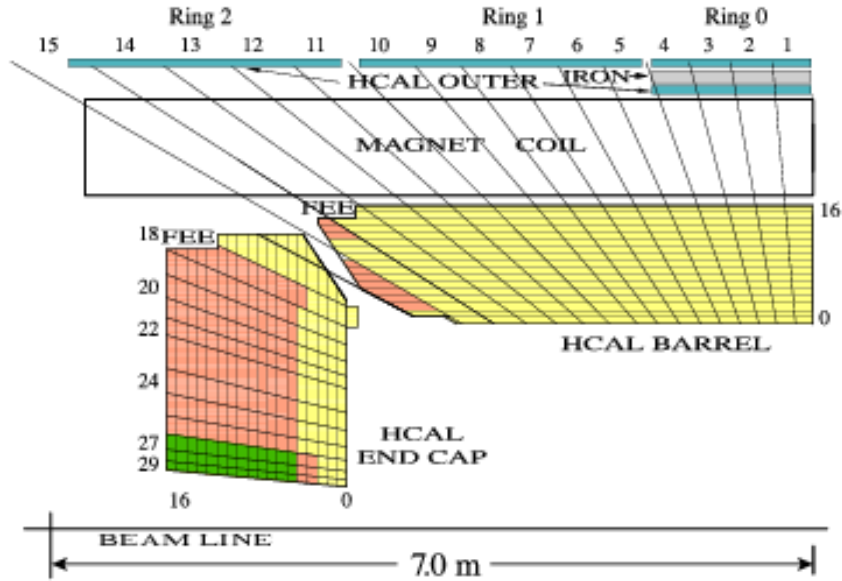


Figure 2.13: A quarter slice of the CMS HCAL detectors. The right end of the beam line is the interaction point, HF (not pictured) would be located far to the left. In the diagram, the numbers on the top and left refer to segments in η , and the numbers on the right and the bottom refer to depth. Colors/shades indicate the combinations of layers that form the different depth segments, which are numbered sequentially starting at 1, moving outward from the interaction point. The outer calorimeter is assigned depth 4. Segmentation along ϕ is not shown [42].

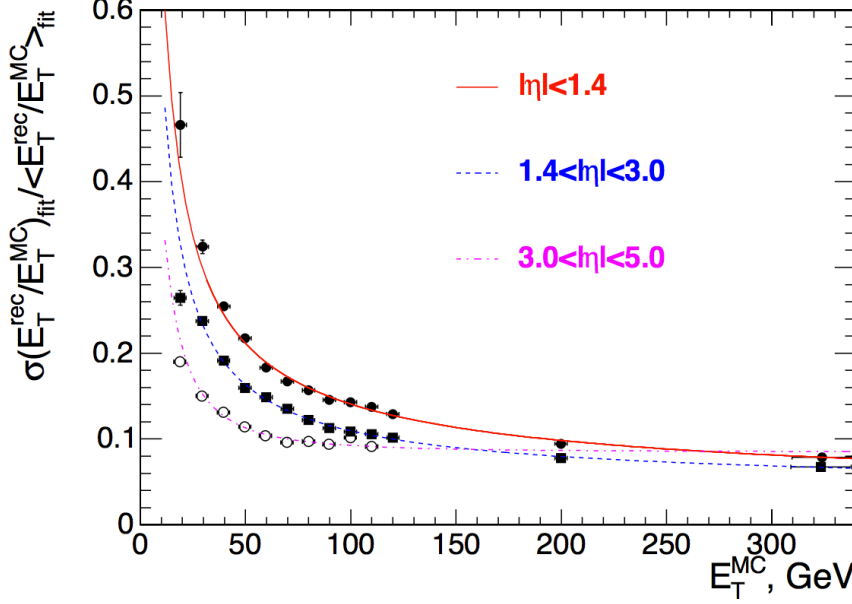


Figure 2.14: The jet transverse energy resolution as a function of the simulated jet transverse energy for barrel jets ($|\eta| < 1.4$), endcap jets ($1.4 < |\eta| < 3.0$) and very forward jets ($3.0 < |\eta| < 5.0$) [35].

the QCD that was discussed in previous sections and is outlined a bit more in section 2.3. The granularity and sampling of the different components of the HCAL system have been chosen so that the jet energy resolution is similar in all three regions (HB, HE, HF). This is illustrated in figure 2.14 where the jet energy resolution is plotted as a function of the transverse energy. More details on this plot can be found in [35].

2.2.5 Muon System

Muons at CMS are measured three times: in the inner tracker, after the magnet coil, and in the return flux. The muon system is designed to measure the path of the muons once they exit the magnet coil and as they traverse the return yoke.

CHAPTER 2. THE EXPERIMENT: LHC AND CMS

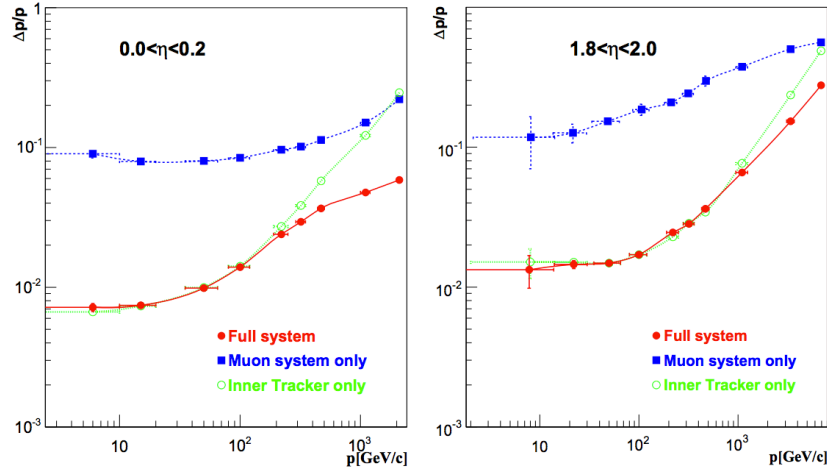


Figure 2.15: The muon momentum resolution verses p using the muon system only, the inner tracker only, or both (“full system”). (left) Barrel $|\eta| < 0.2$ and (right) endcap $1.8 < |\eta| < 2.0$ [35].

The momentum of the muons is measured by the bending angle of the muon’s path as they exit the 4 T coil taking the interaction point as the origin of the muon. The resolution at the origin of this measurement (hereafter referred to as “muon system only”) is dominated by multiple scatter in the material before the first muon station. This applies up to $p_T \sim 200 \text{ GeV}/c$, at which point the spatial resolution of the chamber states to dominate. For low-momentum muons, the best momentum resolution is determined by the silicon tracker (“inner tracker only”). However both systems contain information about the momentum and origin of muons, so CMS uses both of them (“full system”) in concert to determine the momentum of muons produced in collisions. The momentum resolution can be seen in figure 2.15.

The muon system contains three types of gaseous detectors designed to cover the very large surface and the different radiation environments. The barrel region

CHAPTER 2. THE EXPERIMENT: LHC AND CMS

($|\eta| < 1.2$) is characterized by low neutron induced background, low muon rate, and low residual magnetic field in the chambers. For these reasons, drift tube (DT) chambers are used. In contrast the endcap region has high muon rates, neutron induced backgrounds, and residual magnetic field. So in the endcaps cathode strip chambers (CSC) are used to cover the region up to $|\eta| < 2.4$. Both the endcap and barrel regions also use resistive plate chambers (RPC) which provide a fast response with good time resolution but lower position resolution than the DT and CSC systems. Taking the time information from the RPCs in concert with the position information from the CSCs and DTs provide necessary and complementary measurements. The whole system provides a precise and flexible detector that can be used for triggering and measurements.

The layout of one quarter of the CMS muon system is shown in figure 2.16. In the barrel region, four stations of detectors are arranged in cylinders interlayered with the iron return yoke. The segmentation follows the five wheels of the yoke. In each of the endcaps, the CSC and RPC detectors are arranged with four disks perpendicular to the beam in concentric rings. In total, the muon system contains $\sim 25000 \text{ m}^2$ of active detection planes with ~ 1 million electronic channels.

The barrel detectors consist of 250 chambers organized in four layers inside the magnet return yoke, at radii of approximately 4.0, 4.9, 5.9, 7.0 m from the beam axis. Each DT chamber in the three innermost stations consists of 12 layers of drift tubes divided into three groups of four consecutive layers, hereafter called SuperLayers (SL).

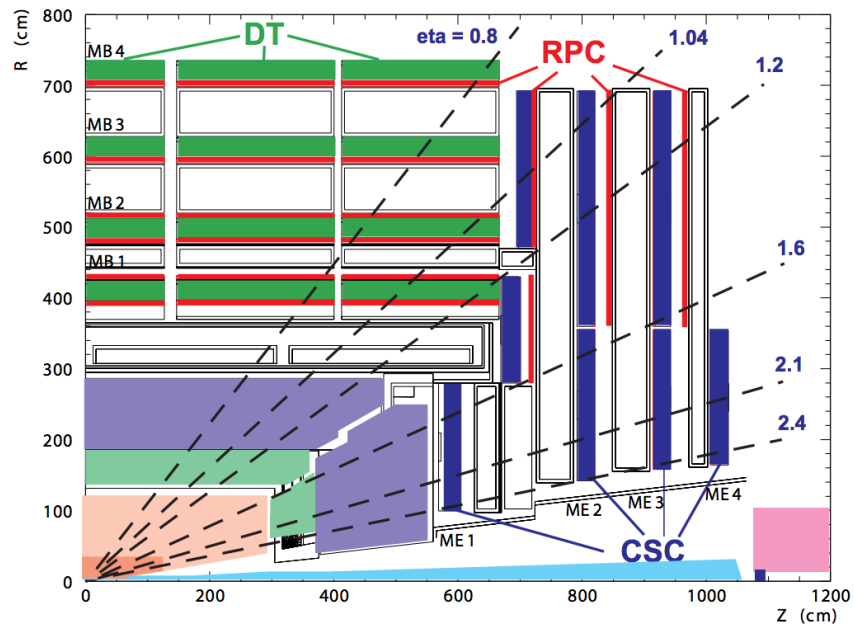


Figure 2.16: Layout of one quarter of the CMS muon system for initial low luminosity running. The RPC system is limited to $|\eta| < 1.6$ in the endcap, and for the CSC system only the inner ring of the ME4 chambers have been deployed [35].

CHAPTER 2. THE EXPERIMENT: LHC AND CMS

The tubes inside each SL are staggered by half a tube. Two SLs measure the $r - \phi$ coordinate in the bending plane (they have wires parallel to the beam line), and the third SL measures the z -coordinate running parallel to the beam. In the outermost station each DT chamber has only the two SLs that measure the $r - \phi$ coordinate. The two innermost stations consist of sandwiches made of a DT chamber placed between 2 RPCs. The two outermost stations consist of packages of a DT chamber coupled to a layer made of 1, 2, or 4 RPCs, depending on the sector and station, placed on the innermost side of the station. The maximum drift length in the barrel is 2.0 cm and the single-point resolution is $\sim 200 \mu\text{m}$, giving a ϕ precision better than $100 \mu\text{m}$ in position and approximately 1 mrad in direction.

In the two endcaps, 468 CSCs arranged in four stations of chambers which are mounted in disks enclosing the CMS magnet, perpendicular to the beam direction. Each CSC is a trapezoidal in shape and consists of six gas gaps, each gap having a plane of radial cathode strips and plane of anode wires running almost perpendicularly to the strips. Most CSCs are overlapped in ϕ to avoid gaps in the muon acceptance¹¹. Each ring station consists of 36 chambers, except for the innermost ring of the second, third, and fourth disks which have 18 chambers. A precise position measurement is made by determining the center-of-gravity of the charge distribution induced on the cathode strips with a spatial resolution $\sim 200 \mu\text{m}$ and angular resolution in $\phi \sim 10$ mrad. Like in the Barrel, there are layers of double-gap RPCs in the endcaps,

¹¹The exception being the third ring of the first endcap disk.

however, for the initial low-luminosity run there are RPCs only in the outer rings of each station, while they are staged in the internal rings. The RPC endcap system is thus limited to $\eta < 1.6$ for the first period of data taking.

2.3 Triggering and Particle Reconstruction

At the designed specifications the LHC would lead to $\sim 10^9$ interactions/sec. Data from only about 10^2 crossings/sec can be written to archival media; hence, the trigger system has to achieve a rejection factor 10^6 . This is performed by the CMS trigger and data acquisition system which consists of four parts: the detector electronics, the Level-1 trigger, the readout network, and an online event filter system (processor farm) that executes the software for the High-Level Triggers (HLT).

Once the data is archived, CMS must analyze this data and reconstruct the individual particles that make up the event. A particle flow event-reconstruction algorithm (PF) has been successfully deployed in the CMS experiment and is nowadays used by most of the analyses. It aims at identifying and reconstructing individually each particle arising from the LHC proton-proton collision, by combining the information from all the subdetectors. Using this algorithm individual particles can be identified as photons, electrons, muons, or charged/neutral hadrons.

2.3.1 CMS Trigger

The size of the LHC detectors and the underground caverns that they reside in imposes a minimum transit time for the signals from the front-end electronics to reach the services cavern which houses the Level-1 trigger logic. A signal must pass from the various subdetectors we have discussed to this Level-1 system and back again to signal a readout of the full detector. The total time allocated for the transit and for reaching a decision to keep or discard data from a particular beam crossing is 3.2 μs . During this time, the detector data is held in buffers while trigger data is collected from the front-end electronics and decisions reached that discard a large fraction of events while regaining the small fraction of interactions of interest (approx. 1 in 1000). Of the total latency, the time allocated to the Level-1 trigger calculations is less than 1 μs .

Custom hardware processors form the Level-1 decision. The Level-1 triggers involve the calorimetry and muons systems, as well as some correlation of the information between these systems. These Level-1 decisions are based on the presence of “trigger primitive” objects such as photons, electrons, muons, and jets above a set of E_T and p_T thresholds that have reduced granularity and resolution. It also employs global sums of E_T and E_T^{miss} . The designed Level-1 pass rate is 100 kHz, but was limited to 50 kHz at startup.

Upon receipt of a Level-1 trigger, the data from the pipelines are transferred to front-end readout buffers. After further signal processing, zero-suppression and/or

CHAPTER 2. THE EXPERIMENT: LHC AND CMS

data-compression each event will have a size of about 1.5 MB for proton-proton interactions. Data from a given event are then transferred to a processor that runs the high-level trigger (HLT) software to reduce the Level-1 output rate of 100 kHz down to 100 Hz for mass storage. Rather than reconstruct all possible objects in an event for HLT, whenever possible only those objects and regions of the detector that are actually needed for the decision are reconstructed. In that way events are discarded as soon as possible, events that still pass are then stored across the “LHC Computing Grid”¹² for later software analysis by individuals searching for specific physics phenomenon.

2.3.2 Particle Flow

The particle-flow event reconstruction aims at reconstructing and identifying all stable particles in the event, i.e., electrons, muons, photons, charged hadrons and neutral hadrons, with a thorough combination of all CMS sub-detectors towards an optimal determination of their direction, energy and type. This list of individual particles is then used to build jets (from which the quark and gluon energies and directions are inferred), to determine the missing transverse energy E_T^{miss} (which gives an estimate of the direction and energy of the neutrinos and other invisible particles), to reconstruct and identify taus, τ , from their decay products, to quantify charged lepton isolation with respect to other particles, to tag b jets, etc [43].

¹²Specifics of this vast and complex GRID computing network are not discussed here.

CHAPTER 2. THE EXPERIMENT: LHC AND CMS

While this algorithm is extremely versatile we will focus our discussion on the pieces that are relevant for this analysis: electrons, muons, and jets. A small discussion will also be made of photons which are used in this analysis as well.

2.3.3 Electrons

The electron reconstruction combines ECAL and tracker information. Electron candidates are reconstructed from clusters of energy deposits in the ECAL, which are then matched to hits in the silicon tracker and silicon tracker seeds that are mapped to ECAL clusters. This dual approach improves the reconstruction efficiency for the very low p_T electrons. The CMS electron reconstruction algorithm is described in [41, 44].

For this physics analysis, the electron candidates are required to have transverse momentum $p_T^e > 7 \text{ GeV}/c$ and a reconstructed $|\eta| < 2.5$. The reconstruction efficiency for isolated electron is expected to be above 90% over the full ECAL acceptance, apart from some narrow “crack” regions.

The identification of electrons relies on a Boosted Decision Tree (BDT) multivariate technique that combines observables sensitive to the amount of bremsstrahlung along the electron trajectory, the geometrical and momentum matching between the electron trajectory and associated clusters, as well as shower-shape observables. The distribution of expected and observed electron BDT output is shown in figure 2.17. The selection is optimized in six regions of the electron p_T^e and $|\eta^e|$ to maximize the

CHAPTER 2. THE EXPERIMENT: LHC AND CMS

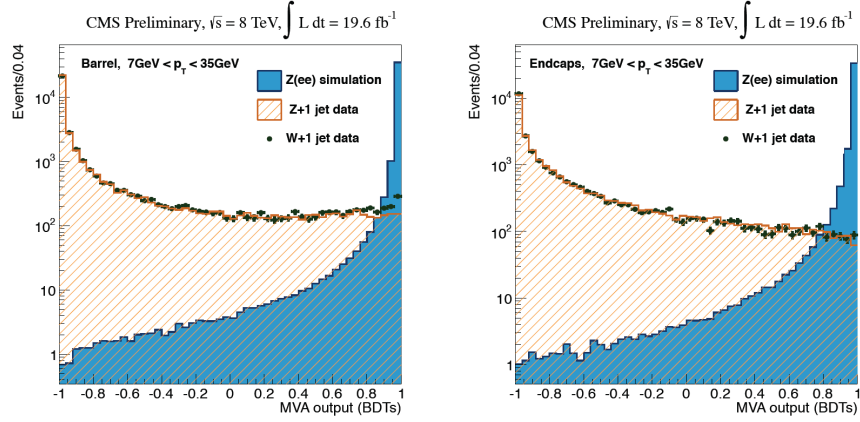


Figure 2.17: Distribution of electron BDT output for training sample $W+\text{jets}$, test sample $Z+\text{jets}$ on 2012 data (fakes) and prompt electrons ($Z \rightarrow ee$ simulation) in the barrel (left) and endcap(right) [45].

expected sensitivity for a low-mass Higgs boson. These regions correspond to two p_T^e ranges, 7–10 GeV and > 10 GeV, and three pseudorapidity regions, corresponding to two regions in the barrel with different material in front of the ECAL, the central barrel ($|\eta^e| < 0.8$) and the outer barrel ($0.800 < |\eta^e| < 1.479$), in addition to the endcap, $1.479 < |\eta^e| < 2.500$.

The quality of the momentum measurement for electrons can substantially vary depending on the electron characteristics. The resolution is mainly dominated by the fluctuations of the measured energy due to bremsstrahlung in the tracker material. This entails that the 4ℓ mass resolution varies broadly, by as much as a factor of 2-3. Therefore, mixing together events with well and poorly measured 4ℓ masses dilutes the Higgs boson search sensitivity, and mass measurement. The analysis uses the propagation of the lepton uncertainty to estimate the 4ℓ mass to proper

CHAPTER 2. THE EXPERIMENT: LHC AND CMS

accounting for the signal mass resolutions for individual events. In order to have a good determination of this uncertainty, but above all to have a description of the resolution of the signal model which corresponds to the data, we need to measure it on high statistics control samples, depending on the electron kinematics and quality, which is done with $Z \rightarrow ee$ sample. The absolute scale has also to be calibrated on data, because the measurement of the Higgs boson mass depends crucially on the uncertainty that we can assign to the leptons in the full phase space of the analysis for a 125 GeV Higgs boson, so covering from 7–100 GeV, which can be covered with $Z \rightarrow ee$ and low mass resonances.

For electrons, the calibration procedure consists of three steps. First, a set of corrections for the momentum scale is obtained by comparing the displacement of the peak position in the distributions of the Z-boson mass in the data and in the simulation in different η regions and in two categories depending on the amount of bremsstrahlung. The corrections are derived as a function of time in order to account for the time-dependent crystal transparency loss. Second, a linearity correction to the momentum scale is applied to account for the p_T -dependent differences between data and simulation by comparing the dielectron mass distributions, binned in p_T^e of one of the two electrons, in data and in simulated $Z \rightarrow ee$ events. The $J/\psi \rightarrow ee$ and $\Upsilon(1S) \rightarrow ee$ events are used as validation for electron $p_T^e < 20$ GeV. All the corrections on the electron momentum scale from the first two steps are applied to data. The left of figure 2.18 shows the residual momentum scale difference before

CHAPTER 2. THE EXPERIMENT: LHC AND CMS

the linearity correction but after the time dependent corrections. Third, the energies of single electrons in the simulation are smeared by applying a random Gaussian multiplicative factor of mean 1 and width $\Delta\sigma$, in order to achieve the resolution observed in the data Z-boson sample. The result of this resolution correction is shown on the right of figure 2.18.

After the electron calibration, the relative momentum scale between data and simulation is consistent within 0.6% in the central barrel and up to $\sim 1.5\%$ in the forward part of the ECAL endcaps. The residual dependence at low momentum is due to the use of wide bins in measured electron p_T^e in evaluating the Z-peak mass shift. The resulting shift of 0.3% (0.1%) for the $4e$ ($2e2\mu$) channel is assigned as a systematic uncertainty in the signal mass scale.

CHAPTER 2. THE EXPERIMENT: LHC AND CMS

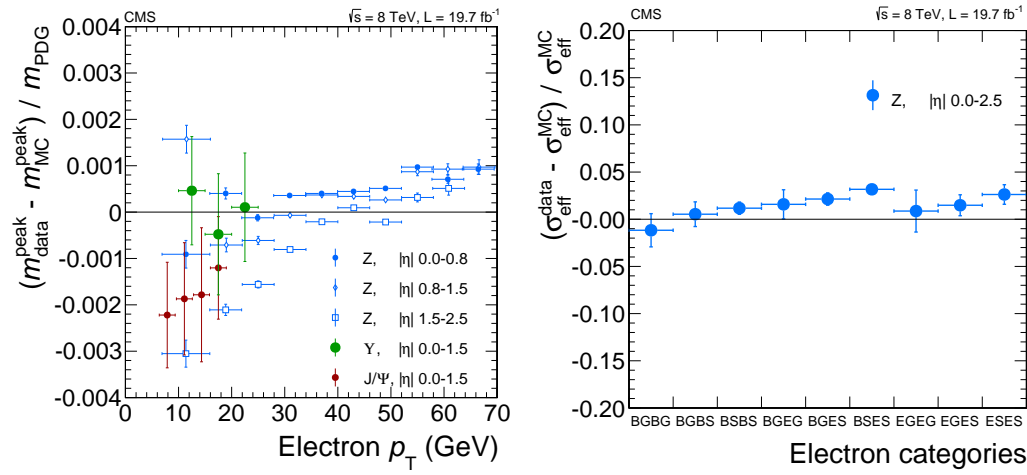


Figure 2.18: (left) Relative difference between the dilepton mass peak positions in data and simulation as obtained from Z , J/ψ and $\Upsilon(nS)$ resonances as a function of the transverse momentum of one of the electrons regardless of the second for dielectron events before p_T dependent correction. (right) Relative difference between the dilepton mass peak positions in data and simulation as obtained from Z , J/ψ and $\Upsilon(nS)$ resonances as a function of the transverse momentum of one of the electrons regardless of the second for dielectron events [41].

2.3.4 Muons

Muon candidates are required to have a transverse momentum $p_T^\mu > 5 \text{ GeV}$ and be within the geometrical acceptance, defined by $|\eta^\mu| < 2.4$. The reconstruction combines information from both the silicon tracker and the muon system. The matching between track segments is done either outside-in, starting from a track in the muon system, or inside-out, starting from a track in the silicon tracker. The muons are selected among the reconstructed muon track candidates by applying minimal requirements on the track segments in both the muon system and inner tracker system and taking into account compatibility with small energy deposits in the calorimeters [41].

For muons, an absolute measurement of momentum scale and resolution is performed by using a reference model of the Z line shape convolved with a Gaussian function. The bias in the reconstructed muon p_T is determined from the position of the Z mass peak as a function of muon kinematic variables, and a correction is derived for the data. A correction for the resolution is also derived for the simulation from a fit to the $Z \rightarrow \mu\mu$ mass spectrum. The large event sample based on low-mass dimuon resonances provides an additional calibration source for the momentum resolution in a similar manner. For muons, the agreement between the observed and simulated mass scales is within 0.1% in the entire pseudorapidity range of interest and assigned as a systematic.

A Z-boson decay into a lepton pair can be accompanied by final-state radiation,

CHAPTER 2. THE EXPERIMENT: LHC AND CMS

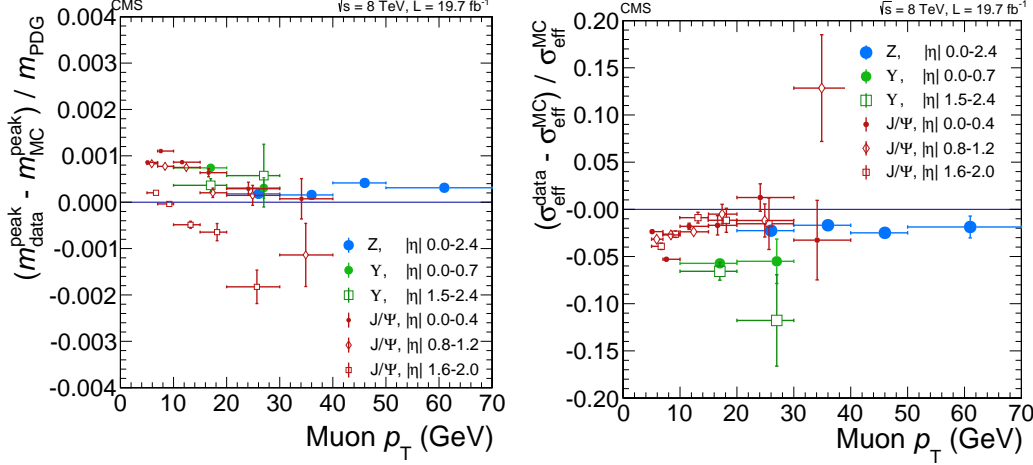


Figure 2.19: (left) Relative difference between the dilepton mass peak positions in data and simulation as obtained from Z , J/ψ and $\Upsilon(nS)$ resonances as a function of the average muon p_T^μ for dimuon events. (right) Relative difference between the dimuon mass resolutions in data and simulation as measured from Z , J/ψ and $\Upsilon(nS)$ decays as functions of the average muon p_T^μ [41].

in which case it is desirable to identify and associate the radiated photon to the corresponding lepton to form the Z -boson candidate. Low-energy photons are identified and reconstructed with the PF reconstruction with a dedicated clustering algorithm designed to identify ECAL energy deposits near global muon tracks. Final-state radiated photons are mostly produced with a direction nearly collinear with the parent lepton and have a harder spectrum than background photons from initial-state radiation or pileup interactions. Therefore, to be identified as FSR, a reconstructed photon must be close to the muon they would be associated with and must make the lepton-pair mass closer to the nominal Z -boson mass. This FSR procedure is applied to muons but not to electrons because the measured electron energies, by

CHAPTER 2. THE EXPERIMENT: LHC AND CMS

construction, already include a large fraction of these photons.

2.3.5 Jets

A jet is a narrow cone of hadrons and other particles produced by a quark or gluon as it emanates from a collision. When a quark or gluon is produced in a collision event the vacuum will generate particles and antiparticles because of the effects of QCD. This generates many particles that may leave tracks or energy deposits in the CMS detector. In the analysis the presence of jets is used as an indication of vector-boson fusion (VBF) or associated production with a weak boson, VH , with $V = W$ or Z , where the V decays hadronically.

In this analysis, jets are reconstructed using the anti- k_T clustering algorithm [46]. The inputs to this algorithm are charged hadrons identified by the PF algorithm by matching calorimeter energy clusters to tracks and PF neutral hadrons identified by calorimeter clusters without tracks¹³.

The anti- k_T algorithm takes these particle tracks and evaluates the distances between particles and combines them into jets by merging together the objects with smallest separation distances. Once a merging has been applied the distances are recalculated and the procedure repeats. The unique part of the anti- k_T algorithm is that the distances are inversely weighted by the momentum (k_T) of the particles. This results in low momentum particles clustering with large momentum ones before

¹³The PF algorithm also has muon and electron pre-identification to omit them from hadron track construction.

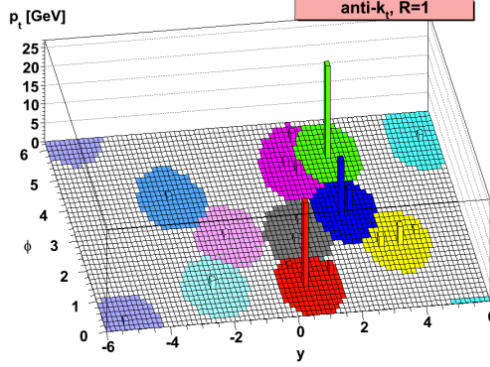


Figure 2.20: An example event of jets formed with the anti- k_T clustering algorithm [46].

many low momentum particles cluster with themselves. Figure 2.20 shows the jets that result from an example event.

In this analysis jets are only considered if they have $p_T^{\text{jet}} > 30 \text{ GeV}$ and $|\eta^{\text{jet}}| < 4.7$. Corrections and calibrations to the individual components of a jet according to its p_T^{jet} and η^{jet} following [47].

2.4 CMS Tracker Alignment

The precise alignment of the silicon sensors in the CMS Tracker is a necessary and challenging task. While external measurements of the positions of sub-detectors¹⁴ can be a good start, they are woefully inadequate in determining the exact position, tilt angle, and deformation of an individual module. In order to maximize the performance in the complex hardware that is used in the tracker the position of each module

¹⁴Using laser rays for example.

CHAPTER 2. THE EXPERIMENT: LHC AND CMS

must be known to extreme precision.

The goal of track-based alignment procedures is to determine the module positions from a large sample of reconstructed charge particle trajectories. Each trajectory is built from charge depositions on individual detectors. Using this method, the residual resolution is now below 10 μm [35]. This optimization problem can be formulated in the context of linear least squares. Module position corrections \mathbf{p} are determined by minimizing an objective function

$$\chi^2(\mathbf{p}, \mathbf{q}) = \sum_j^{\text{tracks}} \sum_i^{\text{hits}} \mathbf{r}_{ij}^T(\mathbf{p}, \mathbf{q}_j) \mathbf{V}_{ij}^{-1} \mathbf{r}_{ij}(\mathbf{p}, \mathbf{q}_j), \quad (2.3)$$

which can be expressed as a sum over all hits i on all tracks j and track parameters \mathbf{q}_j , assuming negligible correlations between hits. Track residuals $\mathbf{r}_{ij} = \mathbf{m}_{ij} - \mathbf{f}_{ij}(\mathbf{p}, \mathbf{q}_j)$ are defined as the difference between the measured hit position and the estimated impact point from the trajectory without the hit in question. These residuals are given as either one- or two-dimensional vectors, and \mathbf{V}_{ij} is either the squared error or the covariance matrix respectively [48].

In order to determine the 200000 different parameters, *alignment parameters*, that describe the locations of the 1440 silicon pixel and 15148 silicon microstrip modules two methods of minimizing track residuals are used, **MILLEPEDE II** and **HIP**. A *track* is a fit to the series of consecutive signals that a charged particle will leave in each layer of silicon as it passes through the CMS tracker. Each of the two algorithms minimizes the residual difference between the hits that make up a track and the

CHAPTER 2. THE EXPERIMENT: LHC AND CMS

position of the track created without that hit.

The main difference between the two algorithms lies in how this minimization is done. **MILLEPEDE II** simultaneously determines the solutions of a complete matrix equation for global and local parameters using all tracks [49]. **HIP**, Hit and Impact Point, determines these parameters iteratively to solve for correlations between modules. The algorithm repeatedly fits a track and then changes a parameter, eventually minimizing the χ^2 for the fit [50].

Vital to the work done as part of this thesis is the connection between the global and local parameters. The tracks and hits are defined on the module level. However these modules are connected to each other and to other subdetectors through mechanical structures that can be used to constrain the system for minimization. In figures 2.21 and 2.22 we map the different structures that can be used to define the locations and constraints that should be used for a given track.

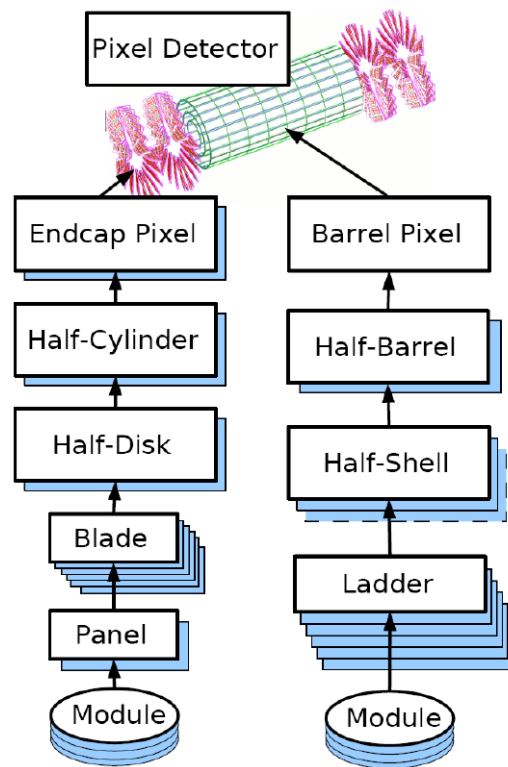


Figure 2.21: Hierarchy of the CMS silicon pixel detector structures [51].

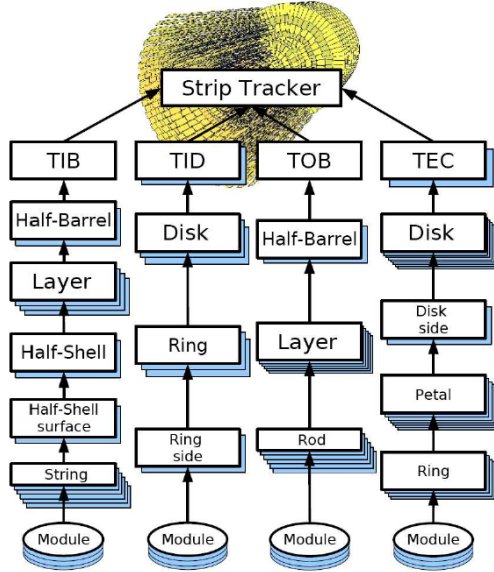


Figure 2.22: Hierarchy of the CMS silicon strip detector structures [52].

2.4.1 Silicon Pixel Alignment in Prompt Calibration Loop

Once a set of alignment parameters is determined, it is not valid forever. As the detector operates the different components may shift. A prime example of this is the pixel barrel, which is not in a fixed position. This is problematic because the CMS magnet may turn on and off, resulting in natural shifts in the positions of different detectors. Part of this thesis work was to develop and implement an active alignment algorithm that would detect and automatically update the detector positions as the CMS experiment takes data.

This active alignment algorithm was implemented in the CMS tracker Prompt

CHAPTER 2. THE EXPERIMENT: LHC AND CMS

Calibration Loop for the start of the 2015 run of the LHC. The Prompt Calibration Loop is a collection of routines that are designed to monitor and automatically adjust parameters to optimize the performance of the the CMS tracking system. The alignment routine developed during this thesis work monitors and adjusts the 36 alignment parameters that describe the pixel detector global parameters. The monitored parameters are the positions (x, y, z) and rotations ($\theta_x, \theta_y, \theta_z$) of the two BPIX half-barrels and the four half-cylinders of the FPIX system¹⁵. If a sufficient shift in one of these parameters is seen¹⁶ then the database of tracker conditions is updated. These consistent updates allow CMS to continue operating at peak performance and avoids rerunning computationally expensive data processing routines to correct the data after the fact.

The effectiveness of this project is illustrated from similar algorithm that was used at the end of the 2012 run after a large shift in the pixel barrel position was seen. Figure 2.23 shows the longitudinal shift between the two half-shelf of the BPIX as measured with the primary vertex residuals. The previous monitoring procedure was implemented farther ‘downstream’ in the computing chain than the current implementation.

¹⁵Two half-cylinders each for FPIX+ and FPIX-.

¹⁶In this case, “sufficient” implies the parameter shifts between a pre-set minimum and maximum window and the significance of that shift is larger than a pre-set amount.

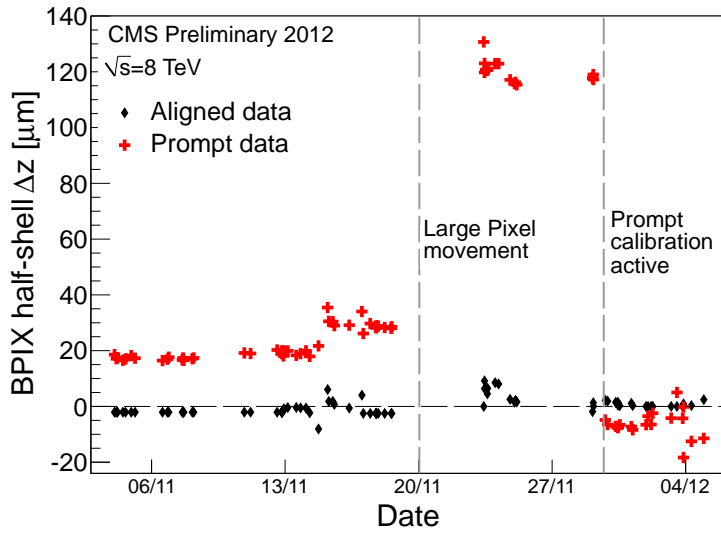


Figure 2.23: Day-by-day value of the relative longitudinal shift between the two half-shells of the BPIX as measured with the primary vertex residuals, for the last month of pp data taking in 2012. Red crosses show the shift observed using the data coming from the prompt reconstruction. The same events, re-reconstructed after the 2012 alignment campaign, which accounts for the major changes in the positions of the half-shells, are represented by black lozenges. A major displacement of the half-shells O(100) μm , occurred during the technical stop in the week of 20th of November, is recovered by the prompt alignment of the BPIX large structures that became active on the 30th November [53].

Chapter 3

Higgs boson at the LHC:

Phenomenology

In this section we discuss specific phenomenological details that are studied for this thesis. First, we discuss the different modes of producing a Higgs boson at the LHC, and different features of these different production modes. Next, we will present the decay of a Higgs boson into two Z bosons and subsequently four leptons. Using this information we will present the implications of off resonance production and decay on the Higgs boson lifetime. Finally, we will discuss the spin and parity of a single-produced resonance and how we can use these relations to characterize a new particle found at the LHC.

3.1 Higgs boson production at LHC

In proton-proton collisions a SM Higgs boson can be produced through the coupling of a Higgs boson to either bosons or fermions. Each of these two categories of Higgs boson production will be dominated by specific production modes. Fermionic production of a Higgs boson can happen either through *gluon-gluon fusion* $gg \rightarrow H$ (ggH) and much less frequently through production in *association with two top quarks* $gg \rightarrow H + t\bar{t}$ ($t\bar{t}H$). Bosonic production of a Higgs boson can occur through *vector boson fusion* (VBF), where two quarks radiate vector bosons which produce the boson in association with two quark jets $qq \rightarrow H + 2\text{jets}$ or through production *associated with a vector boson* $qq \rightarrow H + W/Z$ (VH).

The cross sections of these different production mechanisms as a function of the Higgs boson mass at the LHC are shown in figure 3.1 for the two center of mass energies used in this thesis; $\sqrt{s} = 7$ TeV and $\sqrt{s} = 8$ TeV [54, 55]. Notable features of these cross sections are the order of magnitude difference between gluon-gluon fusion and the bosonic production modes which are all much larger than the $H + t\bar{t}$ production. Additionally, one can see the boost in the gluon-gluon fusion production at $2m_t$, which corresponds to the top quark in the production loop going becoming on shell (explained in more detail below).

The main production mechanism at the LHC is gluon-gluon fusion. The Feynman diagram for this process is shown in figure 3.2. While the Higgs boson does not couple directly to gluons (because they are massless) this mode of production relies on the

CHAPTER 3. HIGGS BOSON AT THE LHC: PHENOMENOLOGY

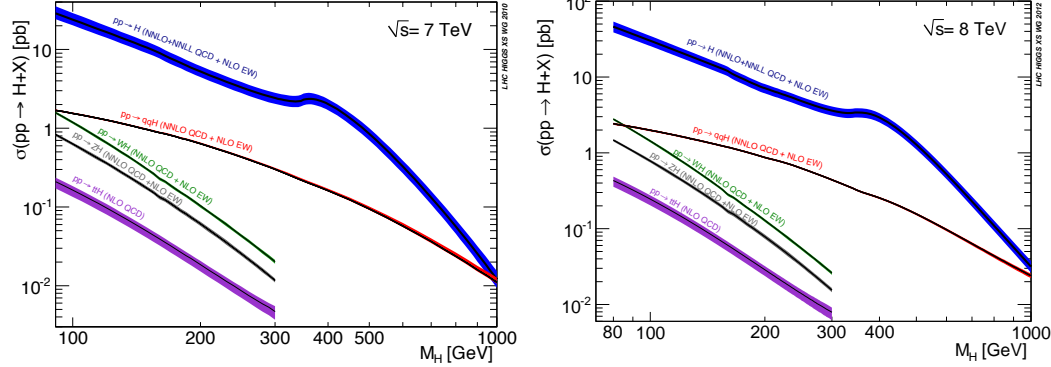


Figure 3.1: Standard Model Higgs boson production cross sections and relative uncertainties at $\sqrt{s} = 7$ TeV and $\sqrt{s} = 8$ TeV. From top to bottom these are $pp \rightarrow H$, blue, $pp \rightarrow H + 2\text{jets}$, red, $pp \rightarrow H + W$, green, $pp \rightarrow H + Z$, grey, $pp \rightarrow H + t\bar{t}$, purple [54, 55].

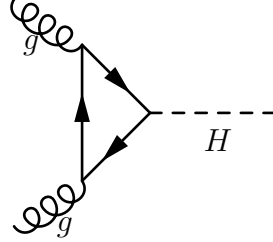


Figure 3.2: Feynman diagram depicting Higgs boson production through gluon-gluon fusion $gg \rightarrow H$. The fermion loop is dominated by top quarks, however all quarks contribute according to their masses.

Higgs boson coupling to fermions generated by the incoming gluons. Because the coupling of the Higgs boson is proportional to the mass of the fermion the dominant contribution is the Higgs boson – top coupling. This leads to a boost in the cross section when the mass of the Higgs boson is twice the top mass because the top in the loop shown is no longer virtual. For the entire mass range that is considered in this analysis this is the most common way to produce a Higgs boson at the LHC.

The second most likely way to produce a Higgs boson at the LHC is through

CHAPTER 3. HIGGS BOSON AT THE LHC: PHENOMENOLOGY

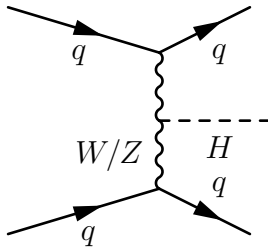


Figure 3.3: Feynman diagram depicting Higgs boson production through vector boson fusion $qq \rightarrow H + 2\text{jets}$.

vector boson fusion. To produce a Higgs boson this way two quarks each radiate a W or Z boson which fuse into the Higgs boson. This production mode relies on the Higgs boson coupling to the vector bosons, making it distinct compared to gluon-gluon fusion. the distinguishing feature of this production mode is the presence of two quark jets in the final state in addition to the Higgs boson. These jets contain information about the Higgs boson and can be exploited to refine searches and study the properties of a new particle. The Feynman diagram for this process is shown in figure 3.3.

Sub-dominant to these two production modes are processes that produce a Higgs boson in association with vector bosons or top quarks. This thesis does not tune the analysis to separate these modes from the dominant ones, instead they are grouped with the dominant modes by how the Higgs boson couples to the other standard model particles. VBF is grouped with VH because the Higgs boson is produced through a coupling to vector bosons while $t\bar{t}H$ is grouped with ggH because it relies on the Higgs boson coupling to fermions.

CHAPTER 3. HIGGS BOSON AT THE LHC: PHENOMENOLOGY

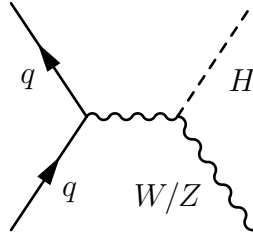


Figure 3.4: Feynman diagram depicting Higgs boson production associated with a vector boson $qq \rightarrow H + W/Z$.

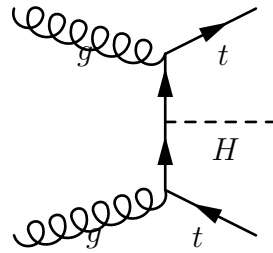


Figure 3.5: Feynman diagram depicting Higgs boson production in association with two top quarks $gg \rightarrow H + t\bar{t}$.

Producing the Higgs boson in association with a W or Z boson is conceptually similar to VBF production. Two quarks interact, producing a vector boson which radiates away a Higgs boson, shown in figure 3.4. Unique to this final state is that in addition to the Higgs boson you will also have the particles associated with the subsequent decay of a W or Z boson. The $t\bar{t}H$ production mode is the smallest of those considered here and is similar to ggH in that it relies on the Higgs boson coupling to top quarks. While the rates of $t\bar{t}H$ are very low, Higgs bosons produced in this way can be distinguished by the presence of two top quarks in addition to the decay product of the Higgs boson, as shown in figure 3.5.

More details are presented in section 4.6, this thesis uses the different properties of

CHAPTER 3. HIGGS BOSON AT THE LHC: PHENOMENOLOGY

ggH and VBF production modes to measure how often a Higgs boson is produced in each mode at the LHC. This work resulted in the first measurement of the production mechanism of Higgs bosons in the 4ℓ final state.

3.2 Higgs boson decay to $ZZ \rightarrow 4\ell$

The SM Higgs boson is an unstable particle that will decay before it can be detected with the CMS detector. However, we can search for this particle by looking at its decay products. To determine which decay products will be the most fruitful to use for a search, we look at the *branching ratio* $BR_X = \frac{N_X}{N_{tot}}$ of the Higgs boson decay for a specific final state in relation to the total number of Higgs bosons we expect. Thus, a high branching ratio will result in a larger number of signal events. In figure 3.6 we plot some of the interesting branching ratios as a function of the Higgs boson mass. To decide if a search is valuable we compare the number of events we expect from a specific decay mode (given by the luminosity times branching ratio times the cross section $\mathcal{L} \cdot BR_X \cdot \sigma_{tot}$) to the number of background events we expect in the search range.

Of specific interest for this thesis is the Higgs boson decay to the $ZZ \rightarrow 4\ell$ final state, shown in figure 3.7. Where we consider $\ell = e, \mu$ because these leptons will be long lived enough to be detected directly by CMS, making them distinct from τ leptons which often decay because of their high mass. The ZZ branching ratio

CHAPTER 3. HIGGS BOSON AT THE LHC: PHENOMENOLOGY

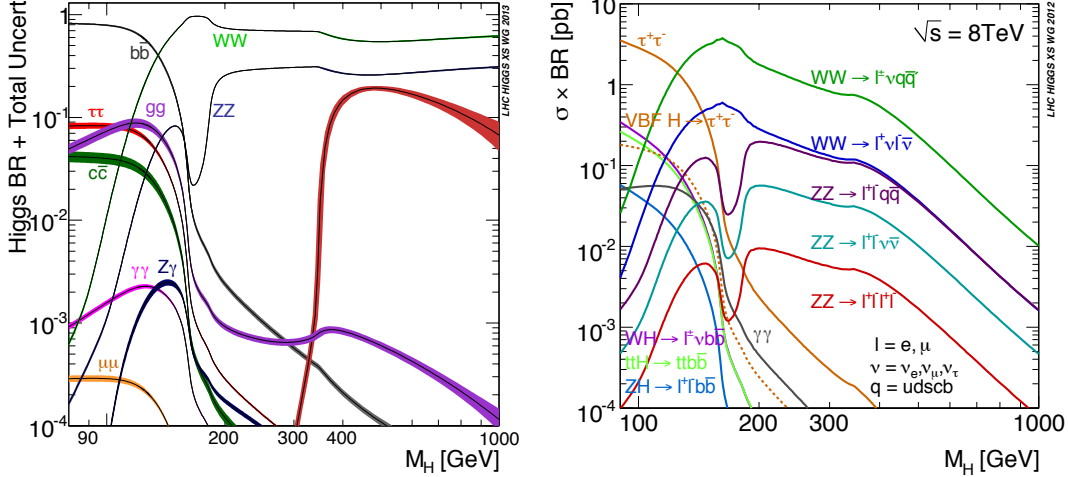


Figure 3.6: (left) Standard Model Higgs boson decay branching ratios for selected decay modes, of specific interest for this thesis is the ZZ branching ratio. (right) Branching ratio times cross section for selected final states, of specific interest for this thesis is the $ZZ \rightarrow 4\ell (\ell^+\ell^-\ell^+\ell^-)$ [55, 56].

is one of the highest across a wide range of possible Higgs boson masses, making it advantageous for search and characterization studies. The 4ℓ final state is used not because it has a particularly high cross section times branching ratio (seen in figure 3.6 right), but because there are low SM background contributions and because all of the final particles are directly detected by the CMS detector.

This thesis considers all of the data collected by CMS during run 1 of the LHC proton-proton collisions. This corresponds to an integrated luminosity of 5.1 fb^{-1} collected at a center of mass energy of $\sqrt{s} = 7 \text{ TeV}$ and 19.7 fb^{-1} collected at $\sqrt{s} = 8 \text{ TeV}$. The search for and later characterization of a Higgs boson requires that there be two pairs of same-flavor, opposite-charge, well-identified isolated leptons ($e^+e^-e^+e^-$, $\mu^+\mu^-\mu^+\mu^-$, or $e^+e^-\mu^+\mu^-$) compatible with an intermediate state of ZZ .

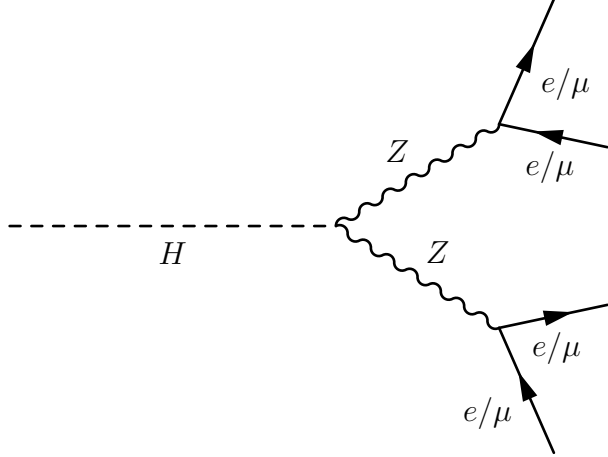


Figure 3.7: Feynman diagram depicting Higgs boson decay into two Z bosons and subsequently into four leptons $H \rightarrow ZZ \rightarrow 4\ell$.

Computability with ZZ is defined such that one or both of the Z 's can be off the mass resonance of the Z -boson.

In this case, a Higgs boson signal will appear as a narrow mass peak on top of a smooth background when observing the four lepton mass distribution. The search is conducted in a mass range of $m_{4\ell} \in 110 - 1000$ GeV. For low-mass Higgs bosons ($m_H < 400$ GeV), the width of the resonance in $m_{4\ell}$ is very well peaked and described with a Breit-Wigner distribution. For higher mass Higgs bosons ($m_H > 400$ GeV), the width of the $m_{4\ell}$ mass peak is much broader and described in the complex pole scheme [54–56]. Detailed analysis of the width of the Higgs boson will be discussed in section 3.3.

The background in the 4ℓ final state is dominated by the SM $q\bar{q} \rightarrow ZZ \rightarrow 4\ell$ production, shown in figure 3.8. This background is not particularly large but it cannot be reduced with quality cuts on the leptons or tuning of phase space without

CHAPTER 3. HIGGS BOSON AT THE LHC: PHENOMENOLOGY

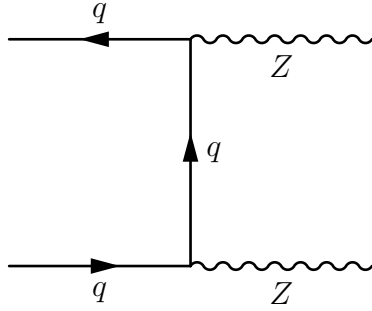


Figure 3.8: Feynman diagram depicting the quark production of two Z bosons $qq \rightarrow ZZ$.

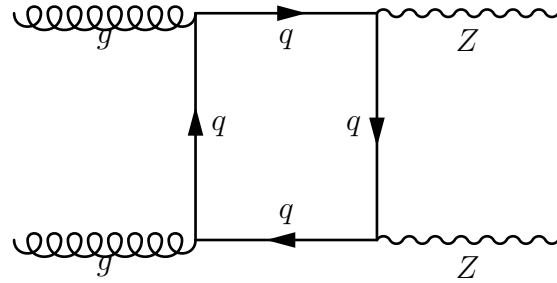


Figure 3.9: Feynman diagram depicting the gluon production of two Z bosons $gg \rightarrow ZZ$.

significant losses to the expected signal. Additionally, there will be SM $gg \rightarrow ZZ \rightarrow 4\ell$, shown in figure 3.9. Z boson production from gluons is also irreducible, but this contribution is about 10% of the dominant $qq \rightarrow ZZ \rightarrow 4\ell$ production. As discussed in the next section, this $gg \rightarrow ZZ$ contribution can actually be exploited to study the properties of any new resonance. There will also be background contributions from collisions that produce a Z boson in addition to other jets or particles that are mis-identified as leptons. This background is reducible by tuning the analysis to remove as much of this noise as possible. This tuning is done by adjusting the quality requirements on the leptons and requirements about where the events fall in phase space. This process is described more in section 4.3.3.

3.3 Higgs boson width: off resonance production and decay

When a new particle is observed, one of the fundamental properties that we would like to understand is the width of the mass resonance. From Einstein's mass–energy equivalence we know that the mass of a particle is equal to the amount of energy it has (in natural units). So by measuring the width of a resonance's mass spectrum (Γ) we have a measure of the natural spread in energies that the particle can take. For this discussion we will operate under the assumption that the Higgs boson mass $m_H \sim 125 - 126$ GeV. In later sections, will we present the results of the Higgs boson search upon which these were made.

Armed with this measurement of the natural energy spread of a particle, one can deduce the mean lifetime (τ) of the particle. The lifetime and a particles energy are related by the time–energy formulation of the Heisenberg uncertainty principle. Simply, this states that $\Delta E \Delta t \geq 1/2$. So measuring the spread in energies for an unstable particle one can deduce the lifetime by the simple relation $\Gamma/2 = 1/2 \cdot 1/\tau$.

This width can also illuminate possible new physics. The lifetime of a particle is determined by the rate that it decays into other particles. This rate is determined by the number of possible states it can decay into. So a particle that can only decay into a small number of particles will have a longer lifetime. The lifetime of the Higgs boson will be determined by its rate of decay into SM particles and particles not yet

CHAPTER 3. HIGGS BOSON AT THE LHC: PHENOMENOLOGY

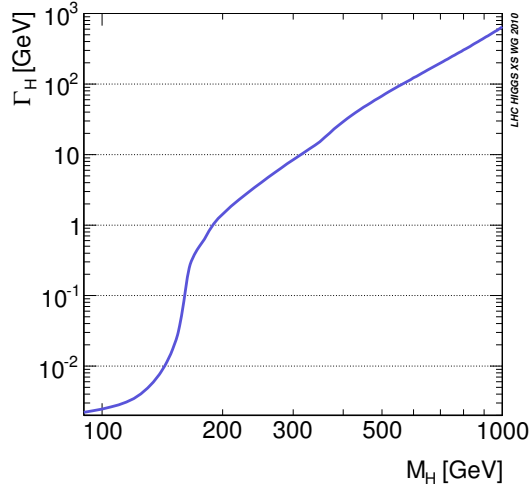


Figure 3.10: Total width of the SM Higgs boson as a function of its mass [54].

described by the SM. So gaining an accurate measurement of the Higgs boson lifetime can be a key into new possible particles that it couples to. The predicted width for a Higgs boson decaying only to SM particles is given in figure 3.10, if you compare this width to the plot of the branching ratios in figure 3.6 (left) you will see that when new decay modes become available the width increases.

As described in section 2.3, CMS has a very fine momentum resolution for both electrons and muons. This allows CMS to accurately measure the mass and width of any new observed resonance very well, on the order of \sim few GeV. However, as shown in figure 3.10 for low mass Higgs bosons the width can be quite small, on the order of \sim MeV. Thus, direct measurement of the natural width of a low-mass Higgs boson will be dominated by the experimental resolution.

To overcome this, recent theoretical work has illuminated a way to measure the

CHAPTER 3. HIGGS BOSON AT THE LHC: PHENOMENOLOGY

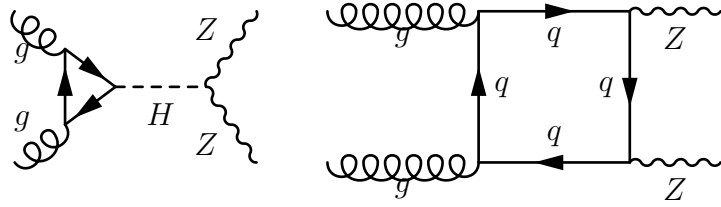


Figure 3.11: (top) Feynman diagram depicting Higgs boson production through gluon-gluon fusion and subsequent decay to two Z bosons $gg \rightarrow H \rightarrow ZZ$. (bottom) Feynman diagram depicting ZZ production through gluon-gluon fusion $gg \rightarrow ZZ$. These two diagrams will interfere with each other having an affect on the final number of events observed in the 4ℓ final state.

total width of a low-mass Higgs boson without looking at the width of the mass resonance directly. This technique relies on the ratio of the on resonance and off resonance production of the new boson. When the new boson is observed on resonance, the mass will be $m_H \sim 125 - 126$ GeV, because this mass $m_H < 2m_Z = 2(91.2 \text{ GeV})$ the Higgs boson will be real and will decay into one or more virtual Z bosons. Virtual particles are particles who's mass is not at the natural resonance, usually denoted Z^* , while real particles which have a mass at the natural resonance. For the dominant production mechanism, we have $gg \rightarrow H \rightarrow Z^{(*)}Z^* \rightarrow 4\ell$.

However, the LHC will produce Higgs bosons far from this mass resonance as well. In this case, the Higgs boson will be virtual while the two Z bosons will both be real, $gg \rightarrow H^* \rightarrow ZZ \rightarrow 4\ell$. In reference [57] the authors point out that $\sim 10\%$ of the total Higgs boson cross section will produce Higgs bosons with a mass $m_{4\ell} > 2m_Z$. A plot of the Higgs boson mass shape is from this reference is shown in figure 3.12 for the ZZ and the WW final states. From this plot one can see the large fraction of the cross section that appears in this high mass window.

CHAPTER 3. HIGGS BOSON AT THE LHC: PHENOMENOLOGY

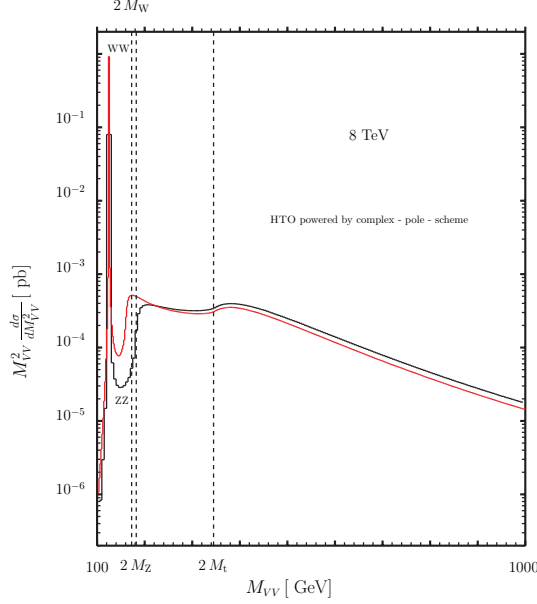


Figure 3.12: The NNLO ZZ (black) and WW (red) invariant mass distributions for $m_H = 125$ GeV [57].

Following [58], we can investigate the total width of the Higgs boson by comparing the on resonance and off resonance cross sections. Generally, the differential cross section of a Higgs boson produced through gluon-gluon fusion decaying into two Z bosons is given by equation (3.1). Where g_{ggH} is the effective coupling of the Higgs boson to gluons, g_{HZZ} is the coupling of the Higgs boson to Z bosons, and Γ_H is the total width of the Higgs boson. Also notice the demarcation of the observed mass of the 4ℓ system, $m_{4\ell}$, is not necessarily the same as the Higgs boson mass m_H .

$$\frac{d\sigma_{gg \rightarrow H \rightarrow ZZ}}{dm_{4\ell}} \sim \frac{g_{ggH}^2 g_{HZZ}^2}{(m_{4\ell}^2 - m_H^2)^2 + m_H^2 \Gamma_H^2} \quad (3.1)$$

When a Higgs boson is produced on the resonance peak $m_{4\ell} \sim m_H$ then the

CHAPTER 3. HIGGS BOSON AT THE LHC: PHENOMENOLOGY

mass integral can be evaluated assuming the second term in the denominator will be larger than the first. Giving the on peak cross section in equation (3.2) note that the cross section is proportional to the couplings and inversely the total width of the Higgs boson. However, if a Higgs boson is produced off of the resonance peak, specifically when $m_{4\ell} - m_H \gg \Gamma_H$, then the cross section becomes independent of the width. Shown in equation (3.3) the off peak cross section becomes proportional to the couplings but the width does not contribute.

$$\sigma_{gg \rightarrow H \rightarrow ZZ}^{\text{on peak}} \sim \frac{g_{ggH}^2 g_{HZZ}^2}{\Gamma_H} \quad (3.2)$$

$$\sigma_{gg \rightarrow H \rightarrow ZZ}^{\text{off peak}} \sim g_{ggH}^2 g_{HZZ}^2 \sim \sigma_{gg \rightarrow H \rightarrow ZZ}^{\text{on peak}} \times \Gamma_H \quad (3.3)$$

From these results we can see that the number of events that are produced on the mass resonance peak is dependent upon the total width of the new boson, while the number of events produced off peak are only dependent upon the couplings to the other SM particles. Thus, as pointed by [58] measuring the ratio of the on peak and off peak Higgs boson production is equivalent to measuring the total width of the new boson.

Complicating this story, is the quantum mechanical interference between the different $gg \rightarrow \dots \rightarrow 4\ell$ processes. While this interference is present for the entire $m_{4\ell}$ range considered in this thesis, at low masses it is a very small and negligible. Above

CHAPTER 3. HIGGS BOSON AT THE LHC: PHENOMENOLOGY

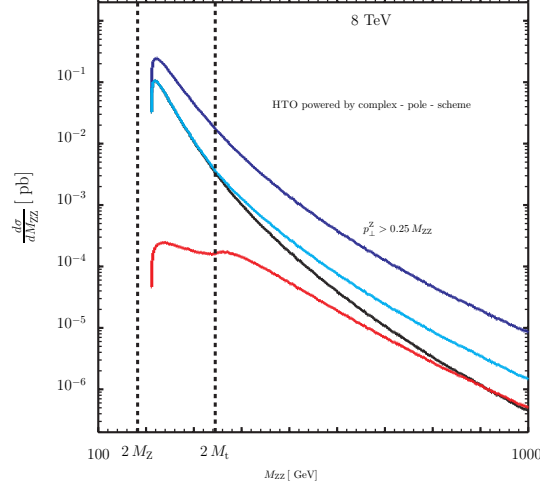


Figure 3.13: The LO ZZ invariant mass distribution $gg \rightarrow ZZ$ for $m_H = 125$ GeV. Black is the total $gg \rightarrow \dots \rightarrow ZZ$ contribution once all interference effects are taken into account. Red is the $gg \rightarrow H^* \rightarrow ZZ$ signal only, and cyan is the $gg \rightarrow \dots \rightarrow ZZ$ contribution ignoring the interference between the two contributions. For scale, the $q\bar{q} \rightarrow ZZ$ contribution is shown in blue [57].

the $2m_Z$ mass, the interference between $gg \rightarrow ZZ \rightarrow 4\ell$ and $gg \rightarrow H^* \rightarrow ZZ \rightarrow 4\ell$, figure 3.11, processes needs to be considered. While the off peak signal contribution will scale by $\sigma_{gg \rightarrow H \rightarrow ZZ}^{\text{on peak}} \times \Gamma_H$ the interference between the signal and background term will scale by $\sqrt{\sigma_{gg \rightarrow H \rightarrow ZZ}^{\text{on peak}} \times \Gamma_H}$.

The impact of these three terms is seen in figure 3.13. Here, one can clearly see the large difference between ignoring (cyan) and correctly accounting (black) for the interference in this region. Neglecting interference one would anticipate a large increase in the yield of the high mass $gg \rightarrow \dots \rightarrow ZZ$ contribution, but since the interference between off resonance Higgs boson production and the $gg \rightarrow ZZ$ continuum background is destructive, the SM actually predicts that the high mass contribution will be lower than otherwise anticipated.

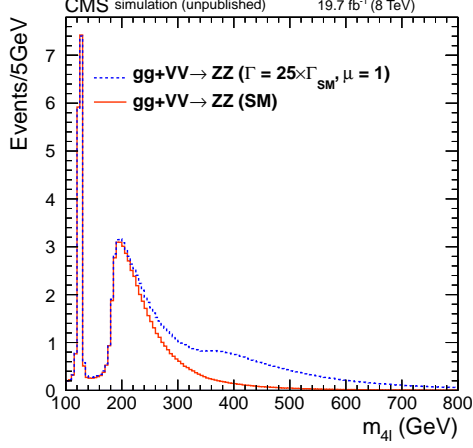


Figure 3.14: Distribution of the expected four-lepton reconstructed mass in full analysis mass range for the sum of the $4e$, 4μ , and $2e2\mu$ channels and for $gg + VV \rightarrow ZZ$ processes for a Higgs boson mass of 125.6 GeV. The expected distribution for a scenario corresponding to a scaling of the width by 25 is also shown. This illustrates the expected change in $gg + VV \rightarrow ZZ$ production when changing the Higgs boson width and at the same time constraining the peak cross section to the SM expectation [59].

The resulting $m_{4\ell}$ distributions for two hypothetical bosons are shown in figure 3.14, they both have the same on peak cross section but different total widths. The result is a change in the total number of events expected in the analysis. Additionally, the shape of the $m_{4\ell}$ distribution and the kinematics of the 4ℓ will be different. A detailed description of how all of these factors are used to determine the width is given in section ???. Also included in this image and analysis is the analogous effect for the VBF production mode.

3.4 Spin and Parity of a Single-Produced Resonance

Using the decay rates and kinematics of a newly observed resonance one can piece together the quantum mechanical properties of the original boson. Once a new particle is observed, its spin and parity quantum numbers need to be determined. This will confirm if the new particle is the Higgs boson that was predicted or something entirely, or partially, different. Using the $H \rightarrow ZZ \rightarrow 4\ell$ decay channel is the best way to study these properties because of the small, well understood background contributions, and because all of the final state particles can be detected by CMS and have excellent precision.

In basic terms, when a new particle is produced in a collision its spin and parity quantum numbers restrict the allowed types of interactions it can have with SM particles. This feature can be observed by investigating the kinematic distributions of the decay products or the particles produced in association with the new resonance. Of particular interest for this thesis work are the $X \rightarrow VV$ couplings (HVV). Where V is any vector boson (Z , W , γ , g), and X is the new resonance. When this new resonance is spin-0, we will use H because the Higgs boson is predicted to be spin-0. While this vertex can be studied by using the production or decay of a new particle we will focus on the properties that can be determined from the decay products.

CHAPTER 3. HIGGS BOSON AT THE LHC: PHENOMENOLOGY

When a new boson is produced it can be either spin-zero, one, or two¹. In this work each is considered as a possibility for a new resonance, and the differences between their kinematics are used to study and classify the newly observed boson. The relevant phenomenology for these interactions is presented below.

3.4.1 Decay of a spin-zero resonance

The scattering amplitude describing the interaction between a spin-zero H boson and two spin-one gauge bosons VV ($ZZ, Z\gamma, \gamma\gamma, WW$ or gg) can be defined as in equation (3.4). Where the coupling parameters a_i^{VV} can have both real and imaginary parts and in general are form factors which can depend on the squared Lorentz invariant four-momenta of V_1 and V_2 , q_{V1}^2 and q_{V2}^2 . In this expression, terms of higher order than q_V^2 have been dropped in the expansion under the assumption that anomalous couplings will only have a small contribution. In this expression, we use a different notation than previous sections and label the field strength tensor of a gauge boson with momentum q_{Vi} and polarization ϵ_{Vi} with $f^{(i)\mu\nu} = \epsilon_{Vi}^\mu q_{Vi}^\nu - \epsilon_{Vi}^\nu q_{Vi}^\mu$. $\tilde{f}_{\mu\nu}^{(i)} = \frac{1}{2}\epsilon_{\mu\nu\rho\sigma}f^{(i)\rho\sigma}$ is the dual field strength tensor, and the superscript * designates a complex conjugate. The masses of the Z or W boson is labeled as m_{V1} , while in the case of massless bosons there is no contribution from this term. To understand the impact form factor will have on the a_1 term, an energy scale Λ_1 for beyond-SM physics that could impact the SM scattering amplitude is also studied [60].

¹Unless, the resonance is actually two particles with a mass difference less than the experimental resolution.

$$A(H \rightarrow VV) \sim \left[a_1^{VV} + \frac{\kappa_1^{VV} q_{V1}^2 + \kappa_2^{VV} q_{V2}^2}{(\Lambda_1^{VV})^2} \right] m_{V1}^2 \epsilon_{V1}^* \epsilon_{V2}^* + a_2^{VV} f_{\mu\nu}^{*(1)} f^{*(2)\mu\nu} + a_3^{VV} f_{\mu\nu}^{*(1)} \tilde{f}^{*(2)\mu\nu} \quad (3.4)$$

In the SM, the tree-level contribution from ZZ (WW) correspond to $a_1^{ZZ(WW)} \neq 0$, while the loop-induced SM contribution for $Z\gamma, \gamma\gamma$, and gg is $a_2^{VV} \neq 0$. Small SM contributions to the higher order a_i terms can come from loop level contributions but, in general, these should be small. Additional restrictions on the allowed values for the κ_i terms arise from symmetry and gauge invariance. For ZZ , they require $\kappa_1^{ZZ} = \kappa_2^{ZZ} = -\exp(-i\phi_{\Lambda 1}^{ZZ})$ where $\phi_{\Lambda 1}^{ZZ}$ is the relative phase between the a_1^{ZZ} and Λ_1 terms.

The parity conserving contribution from a pseudoscalar particle ($0^{+-}, CP\text{-odd}$) would be generated by the a_3 term, while a higher order scalar ($0^{++}, CP\text{-even}$) would be generated by a_2 or Λ_1 contributions. Anomalous contributions for the Λ_1, a_2 , or a_3 terms could be a sign of BSM physics and can in general have be complex, allowing for a relative phase between them and the SM a_1 term. To determine if these anomalous terms contribute to an observed resonance, we parameterize the contribution of one of these terms in an effective cross section fraction. These fractions are given in equation (3.5), where σ_i is the cross section for an $a_i = 1, a_{j \neq i} = 0$ particle decaying to the $2e2\mu$ final state². The phases ϕ_{ai} are used to generalize equation (3.4) so that the

² $\tilde{\sigma}_{\Lambda 1}$ is the effective cross section of the process corresponding to $\Lambda_1 = 1$ TeV, given in units of $\text{fb} \cdot \text{TeV}^4$.

CHAPTER 3. HIGGS BOSON AT THE LHC: PHENOMENOLOGY

anomalous contributions to be complex.

$$\begin{aligned} f_{\Lambda 1} &= \frac{\tilde{\sigma}_{\Lambda 1}/(\Lambda_1)^4}{|a_1|^2\sigma_1 + |a_2|^2\sigma_2 + |a_3|^2\sigma_3 + \tilde{\sigma}_{\Lambda 1}/(\Lambda_1)^4 + \dots}, & \phi_{\Lambda 1}, \\ f_{a2} &= \frac{|a_2|^2\sigma_2}{|a_1|^2\sigma_1 + |a_2|^2\sigma_2 + |a_3|^2\sigma_3 + \tilde{\sigma}_{\Lambda 1}/(\Lambda_1)^4 + \dots}, & \phi_{a2} = \arg\left(\frac{a_2}{a_1}\right), \\ f_{a3} &= \frac{|a_3|^2\sigma_3}{|a_1|^2\sigma_1 + |a_2|^2\sigma_2 + |a_3|^2\sigma_3 + \tilde{\sigma}_{\Lambda 1}/(\Lambda_1)^4 + \dots}, & \phi_{a3} = \arg\left(\frac{a_3}{a_1}\right), \end{aligned} \quad (3.5)$$

These fractions are especially useful because they allow for great flexibility in the measurements. They are independent of the collider energy so they can be used to compare measurements made at different facilities, they are independent of coupling notation so can be used to translate between many different formulations for the spin-0 interactions, and they are bounded between 0 and 1 which allows investigation of the full phase space.

In CMS studies of these results, analogous fractions are created for the WW , $Z\gamma$, $\gamma\gamma$ final states. These fractions can be combined for ZZ and WW under different assumptions about the relationships between the a_i^{VV} terms. These results were a direct consequence of these studies and are left as a reference for the reader [61].

3.4.2 Decay of a spin-one resonance

In the case of a spin-one resonance, the amplitude of its interaction with a pair of massive gauge bosons, ZZ or WW , consists of two independent terms, seen in equation

CHAPTER 3. HIGGS BOSON AT THE LHC: PHENOMENOLOGY

(3.6).

$$A(X_{J=1} \rightarrow VV) \sim b_1^{VV} [(\epsilon_{V1}^* q)(\epsilon_{V2}^* \epsilon_X) + (\epsilon_{V2}^* q)(\epsilon_{V1}^* \epsilon_X)] + b_2^{VV} \epsilon_{\alpha\mu\nu\beta} \epsilon_X^\alpha \epsilon_{V1}^{*\mu} \epsilon_{V2}^{*\nu} \tilde{q}^\beta \quad (3.6)$$

Where ϵ_X is the polarization vector of the boson X with spin one, $q = q_{V1} + q_{V2}$ and $\tilde{q} = q_{V1} - q_{V2}$ [62, 63]. Here the $b_1^{VV} \neq 0$ coupling corresponds to a vector particle, while the $b_2^{VV} \neq 0$ coupling corresponds to a pseudovector. The $Z\gamma$ interactions of the spin-one particle are not considered, while the $\gamma\gamma$ and gg interactions are forbidden by the Landau-Yang theorem [64, 65], where the gg case is justified by the assumption that the state X is color-neutral.

The evidence for a new boson in the ZZ final state will be presented in section 4.5, similar resonances have been seen in the $H \rightarrow \gamma\gamma$ decay channel, preventing the observation from being spin-one [66–68]. In the case that the ZZ resonance is different than the one seen in these references, we test if an observed boson is more consistent with spin-one or the SM predicted Higgs boson.

Pure vector (1^+), pseudovector (1^-), and mixed vector-pseudovector states are tested using the fraction f_{b2}^{VV} given in equation (3.7). This f_{b2}^{VV} parameter is a continuous unique way to define any state that is a mixture of 1^+ and 1^- . Where σ_{bi} is the cross section of the process corresponding to $b_i = 1, b_{j \neq i} = 0$ in the $X \rightarrow ZZ \rightarrow 2e2\mu$ final state.

$$f_{b2}^{VV} = \frac{|b_2^{VV}|^2 \sigma_{b2}}{|b_1^{VV}|^2 \sigma_{b1} + |b_2^{VV}|^2 \sigma_{b2}}, \quad (3.7)$$

3.4.3 Decay of a spin-two resonance

In the case of a general spin-two resonance, we test if a new observation is more consistent with the SM Higgs boson or a spin-two boson. The amplitude to describe the $X \rightarrow ZZ$ production is given in equation (3.8) (This same amplitude describes the $gg \rightarrow X$ production with $m_V = 0$.) where $t^{\mu\nu}$ is the wavefunction of a spin-two particle X given by a symmetric traceless tensor, m_V is the mass of the considered gauge boson, and Λ is the scale of BSM physics [62, 63]. The couplings c_1^{VV} and c_5^{VV} correspond to the parity-conserving interaction of a spin-two tensor with minimal gravity-like couplings. As in the spin-zero case, the couplings c_i^{VV} are in general momentum-dependent form factors. In this analysis it is assumed that the form factors are momentum-independent constants and, thus, only the lowest q_i^2 order terms in the scattering amplitude are considered [61].

CHAPTER 3. HIGGS BOSON AT THE LHC: PHENOMENOLOGY

$$\begin{aligned}
A(X_{J=2} \rightarrow VV) \sim & \Lambda^{-1} \left[2c_1^{VV} t_{\mu\nu} f^{*1,\mu\alpha} f_\alpha^{*2,\nu} + 2c_2^{VV} t_{\mu\nu} \frac{q_\alpha q_\beta}{\Lambda^2} f^{*1,\mu\alpha} f^{*2,\nu\beta} \right. \\
& + c_3^{VV} t_{\beta\nu} \frac{\tilde{q}^\beta \tilde{q}^\alpha}{\Lambda^2} (f^{*1,\mu\nu} f_\mu^{*2} + f^{*2,\mu\nu} f_\mu^{*1}) + c_4^{VV} t_{\mu\nu} \frac{\tilde{q}^\nu \tilde{q}^\mu}{\Lambda^2} f^{*1,\alpha\beta} f_{\alpha\beta}^{*2} \\
& + m_V^2 \left(2c_5^{VV} t_{\mu\nu} \epsilon_{V1}^{*\mu} \epsilon_{V2}^{*\nu} + 2c_6^{VV} t_{\mu\nu} \frac{\tilde{q}^\mu q_\alpha}{\Lambda^2} (\epsilon_{V1}^{*\nu} \epsilon_{V2}^{*\alpha} - \epsilon_{V1}^{*\alpha} \epsilon_{V2}^{*\nu}) + c_7^{VV} t_{\mu\nu} \frac{\tilde{q}^\mu \tilde{q}^\nu}{\Lambda^2} \epsilon_{V1}^* \epsilon_{V2}^* \right. \\
& \quad \left. + c_8^{VV} t_{\mu\nu} \frac{\tilde{q}^\mu \tilde{q}^\nu}{\Lambda^2} f^{*1,\alpha\beta} f_{\alpha\beta}^{*2} \right. \\
& \quad \left. + m_V^2 \left(c_9^{VV} t^{\mu\alpha} \frac{\tilde{q}_\alpha \epsilon_{\mu\nu\rho\sigma} \epsilon_{V1}^{*\nu} \epsilon_{V2}^{*\rho} q^\sigma}{\Lambda^2} + c_{10}^{VV} t^{\mu\alpha} \frac{\tilde{q}_\alpha \epsilon_{\mu\nu\rho\sigma} q^\rho \tilde{q}^\sigma (\epsilon_{V1}^{*\nu} (q \epsilon_{V2}^*) + \epsilon_{V2}^{*\nu} (q \epsilon_{V1}^*))}{\Lambda^4} \right) \right], \\
& \tag{3.8}
\end{aligned}$$

In this work, we study the ten spin-two scenarios listed in table 3.1, under the assumption that the production is via gluon-gluon fusion, $q\bar{q}$ production, or without any assumption about the production mechanism. The 2_m^+ represents a massive graviton-like boson as suggested in models with warped extra dimensions [69, 70]. A modified minimal coupling model 2_b^+ is also considered, where the SM fields are allowed to propagate in the bulk of the extra dimensions [71], corresponding to $c_1^{VV} \ll c_5^{VV}$. Additionally eight spin-two models with higher dimension operators are considered [61].

Table 3.1: List of spin-two models with the decay couplings of an exotic X particle. The subscripts m (minimal couplings), h (couplings with higher-dimension operators), and b (bulk) distinguish different scenarios [61].

J^P	Model	$X \rightarrow VV$ Couplings
2_m^+		$c_1^{VV} = c_5^{VV} \neq 0$
2_{h2}^+		$c_2^{VV} \neq 0$
2_{h3}^+		$c_3^{VV} \neq 0$
2_h^+		$c_4^{VV} \neq 0$
2_b^+		$c_1^{VV} \ll c_5^{VV} \neq 0$
2_{h6}^+		$c_6^{VV} \neq 0$
2_{h7}^+		$c_7^{VV} \neq 0$
2_h^-		$c_8^{VV} \neq 0$
2_{h9}^-		$c_9^{VV} \neq 0$
2_{h10}^-		$c_{10}^{VV} \neq 0$

Chapter 4

$H \rightarrow ZZ \rightarrow 4\ell$ search &

Production/Decay Fractions

In this section we discuss the search for a Higgs boson decaying to the 4 lepton final state at CMS. First, we will provide a general overview of the analysis. Next, we will discuss additional requirements that are made on the physics objects we have already introduced. Using this information we will present the event selection, simulation, and categorization for the search and a summary of the expected signal and background estimations. Next, we will introduce the kinematic distributions that are used to enhance our signal against the background processes. Specifically, the $m_{4\ell}$ mass shape, the *Matrix Element Likelihood Approach* (MELA) kinematic discriminant, the $p_T^{4\ell}$, and the jet kinematic discriminant. Finally we will present the results of this search and first major characterization study: The production

and decay fraction measurements. The studies presented in this section have been published in reference [41].

4.1 General overview of $H \rightarrow ZZ \rightarrow 4\ell$

While some of this information was introduced earlier in order to discuss specific theoretical and phenomenological aspects of this work, here we will summarize the $H \rightarrow ZZ \rightarrow 4\ell$ search. This analysis searches for a scalar Higgs boson which would be the smoking gun that the Higgs Mechanism is responsible for electroweak symmetry breaking. This search covers the range of $m_{4\ell} \in 110\text{--}1000\,\text{GeV}$ because the mass of the Higgs boson (m_H) is a free parameter in the theoretical basis for the theory. General theoretical considerations suggest that m_H should be less than $\approx 1\,\text{TeV}$ [72–75], while precision electroweak measurements imply that $m_H < 152\,\text{GeV}$ [76]. Previously, direct searches for the Higgs boson have been made at the LEP collider setting the limit that $m_H > 114.4\,\text{GeV}$ [77], and the Tevatron collider, excluding $m_H \notin 90\text{--}109\,\text{GeV} \cup 149\text{--}182\,\text{GeV}$ [78, 79].

In this thesis, the analysis of the $H \rightarrow ZZ \rightarrow 4\ell$ channel is presented using the entire dataset collected by the CMS experiment during the 2011-2012 LHC running period. The data correspond to an integrated luminosity of $5.1\,\text{fb}^{-1}$ of proton-proton collisions at a center of mass energy of $\sqrt{s} = 7\,\text{TeV}$, and $19.7\,\text{fb}^{-1}$ at $\sqrt{s} = 8\,\text{TeV}$. The search looks for a signal consisting of two pairs of same-flavor, opposite-charge,

well-identified and isolated leptons compatible with a ZZ -system, appearing as a narrow resonance on top of a smooth background in the four-lepton invariant mass distribution.

4.2 Object Selection

Given the very low branching fraction of the $H \rightarrow ZZ \rightarrow 4\ell$ decay, it is important to maintain a very high lepton selection efficiency in a wide range of momenta, to maximize the sensitivity for a Higgs boson in the full range $m_{4\ell} \in 110\text{--}1000$ GeV. Additionally, because the signal sensitivity depends on the 4ℓ mass resolution it is crucial to calibrate the individual lepton momentum scale and resolution to a level such that the systematic uncertainties are small. A summary of the lepton identification, scale, and resolution is presented in section 2.3. Additional object selections including lepton isolation and vertex compatibility are presented here.

Lepton isolation is used to discriminate leptons originating from high- p_T boson decay, as in the case of the signal, from those arising from hadronic processes, which are typically immersed in a jet of other hadrons. The isolation of individual leptons, measured relative to their transverse momentum p_T^ℓ , is defined by:

$$R_{\text{iso}}^\ell \equiv \left(\sum p_T^{\text{charged}} + \max [0, \sum p_T^{\text{neutral}} + \sum p_T^\gamma - p_T^{\text{PU}}(\ell)] \right) / p_T^\ell, \quad (4.1)$$

where the sums are over the charged, neutral, and photon particle candidates in

CHAPTER 4. $H \rightarrow ZZ \rightarrow 4\ell$ SEARCH & PRODUCTION/DECAY FRACTIONS

a cone $\Delta R = \sqrt{(\Delta\eta)^2 + (\Delta\phi)^2} < 0.4$ around the lepton direction at the interaction vertex (where $\Delta\eta$ & $\Delta\phi$ quantify the angular distance between the candidate from the lepton). In equation (4.1), the sums are computed for particles that originate from the primary vertex of the event (defined as the vertex with the highest $\sum p_T^2$ of associated tracks). In this expression, the contribution from pileup ($p_T^{PU}(\ell)$) is explicitly subtracted. This pileup contribution is computed separately for electrons and muons and outlined in [41]. In this isolation calculation, photons that qualify for FSR reconstruction are omitted from the p_T^γ sum. FSR is outlined in the muon reconstruction section 2.3.4.

In order to suppress leptons originating from in-flight decays of hadrons and muons from cosmic rays, all leptons are required to come from the same primary vertex. This is achieved by requiring that the significance of the interaction parameter in three dimensions is $SIP_{3D} < 4$, where $SIP_{3D} \equiv IP_{3D}/\sigma_{IP_{3D}}$ is the ratio of the impact parameter of the lepton track in three dimensions, with respect to the chosen primary vertex position, and its uncertainty.

The combined efficiency for the reconstruction, identification, and isolation (and conversion rejection for electrons) of prompt electrons or muons is measured in data using a tag and probe method based on an inclusive sample of Z-boson events, separately for 7 and 8 TeV data. The efficiency is measured by fitting the Z line shape plus a background model to the dilepton mass distributions where the probe lepton passes or fails the selection criteria. This efficiency is calculated in both simulation

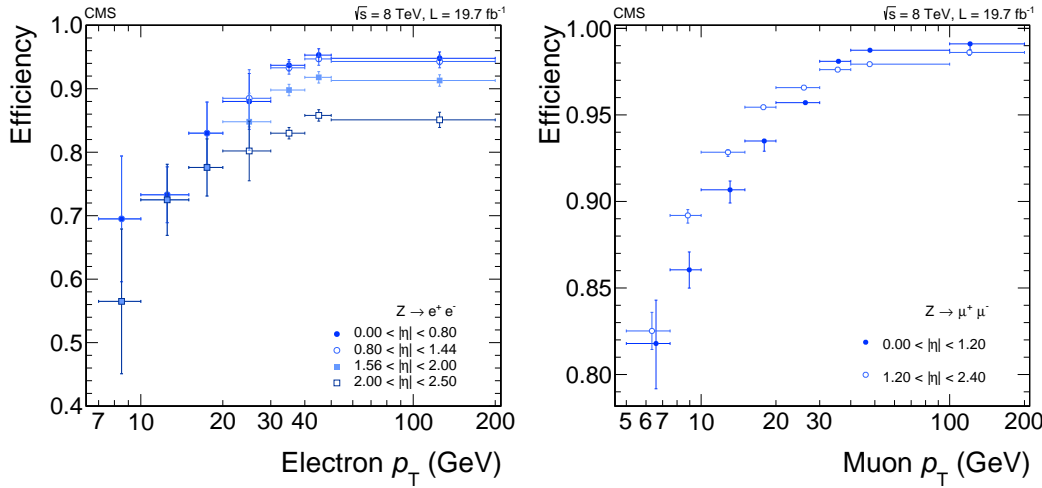


Figure 4.1: Efficiency, as a function of the lepton p_T^ℓ , for reconstructing and selecting (left) electrons and (right) muons, measured with a $Z \rightarrow \ell\ell$ data sample by using a tag-and-probe method [41].

and data and used to correct the simulation accordingly. These efficiencies are shown in figure 4.1 for both electrons and muons.

In the analysis the presence of jets is used as an indication of vector-boson fusion (VBF) or associated production with a weak boson, VH , with $V = W$ or Z , where the V decays hadronically. Jets are reconstructed using the anti- k_T clustering algorithm with distance parameter $D = 0.5$, as discussed in section 2.3.5. Jets are only considered if they have $p_T^{\text{jet}} > 30$ GeV, $|\eta^{\text{jet}}| < 4.7$, originate from the primary vertex, and are required to be separated from the lepton candidates and from identified FSR photons by $\Delta R > 0.5$. Jet energy corrections are applied as a function of the jet p_T^{jet} and η^{jet} [47]. An offset correction is applied to subtract the energy contribution not associated with the high- p_T scattering, such as electronic noise and pileup, based on

the jet-area method [47, 80, 81].

4.3 Event Selection, Simulation, & Categorization

4.3.1 Simulated Data Samples

The Monte Carlo (MC) simulated data samples, generated with state-of-the-art theoretical calculations for both the SM Higgs boson signal and relevant background processes, are used to optimize the event selection and to evaluate the acceptance and systematic uncertainties. For the gluon-gluon fusion and vector-boson fusion Higgs boson signal the simulated events are generated with POWHEG [82–84] at Next-to-leading-order (NLO) QCD accuracy. The Higgs boson decay is modeled with JHUGEN 3.1.8 [60, 62, 63] to include proper treatment of the interference effects associated with permutations of identical leptons in the four-electron and four-muon final states. Samples of WH, ZH, and $t\bar{t}H$ events are generated with PYTHIA 6.4.24 [85]. Higgs boson signal events for all production mechanisms are reweighted to include contributions from gluon fusion up to next-to-next-to-leading-order (NNLO) and next-to-next-to-leading logarithm (NNLL) [54, 86–96], and from the vector-boson fusion contribution computed at NNLO [54, 97–101].

The two dominant irreducible background contributions for this analysis are the

SM $q\bar{q} \rightarrow ZZ$ and $gg \rightarrow ZZ$ events. The $q\bar{q} \rightarrow ZZ$ background is simulated at NLO using the POWHEG [102] program while the $gg \rightarrow ZZ$ contribution is simulated at LO using GG2ZZ [103]. The yields for these SM contributions are calculated with MCFM [104–106]. The reducible backgrounds including, $Zb\bar{b}$, $Zc\bar{c}$, $Z\gamma + \text{jets}$, $WW + \text{jets}$, $WZ + \text{jets}$, etc. (referred to as $Z + \text{jets}$) are simulated with MADGRAPH [107] and used to cross check the data driven methods outlined in the next section (The $t\bar{t}$ contribution to this background is simulated at NLO with POWHEG).

To model the constituents (quarks & gluons) of the colliding protons correctly, parton distributions functions are used (CTEQ6L [108] for LO generators, CT10 [109] for NLO and higher-order generators). To model the underlying event, jet fragmentation, and showering all events are processed with PYTHIA 6.4.24 [85]. The CMS detector is simulated with great detail using a simulation based on GEANT4 [110, 111].

4.3.2 Selection & Categorization

The event selection is designed to give a set of signal candidates in the $H \rightarrow ZZ \rightarrow 4\ell$ final state in three mutually exclusive subchannels: $4e$, 4μ , and $2e2\mu$. Four well-identified and isolated leptons are required to originate from the primary vertex to suppress the $Z + \text{jets}$ and $t\bar{t}$ backgrounds.

Z candidates are formed with a pair of leptons of the same flavor and opposite charge ($\ell^+\ell^-$). When forming the Z -boson candidates, only FSR photons that make

CHAPTER 4. $H \rightarrow ZZ \rightarrow 4\ell$ SEARCH & PRODUCTION/DECAY FRACTIONS

the lepton-pair mass closer to the nominal Z-boson mass are incorporated. If the $m_{\ell\ell\gamma} > 100$ GeV, the photon is not considered, to minimize the fraction of misidentification.

Among all the possible opposite-charge lepton pairs in the event, the one with an invariant mass closest to the nominal Z-boson mass is denoted Z_1 and retained if $40 < m_{Z_1} < 120$ GeV. Then, all remaining leptons are considered and a second same flavor opposite-charge pair $\ell^+\ell^-$ becomes Z_2 when the pair has the highest scalar sum of $p_T^{\ell\ell}$ in the event and $12 < m_{Z_2} < 120$ GeV. This selection procedure results in one or more of the Z-bosons to be off shell for $m_H < 180$ GeV.

Among the four selected leptons forming the Z_1 and the Z_2 , at least one lepton is required to have $p_T^\ell > 20$ GeV, and another one is required to have $p_T^\ell > 10$ GeV. These p_T^ℓ thresholds ensure that the selected events have leptons on the efficiency plateau of the trigger. To further remove events with leptons originating from hadron decays produced by jet fragmentation or from the decay of low-mass hadron resonances, it is required that any opposite-charge pair of leptons chosen among the four selected leptons (irrespective of flavor) satisfy $m_{\ell^+\ell^-} > 4$ GeV. The phase space for the search of the SM Higgs boson is defined by restricting the measured mass range to $m_{4\ell} > 100$ GeV.

The efficiency versus m_H is shown in Fig. 4.2 for the gluon fusion Higgs boson production mode, and it is very similar for other production modes. The efficiency within the geometrical acceptance is $\approx 30\%$ (58%), 43% (71%), and 62% (87%) for

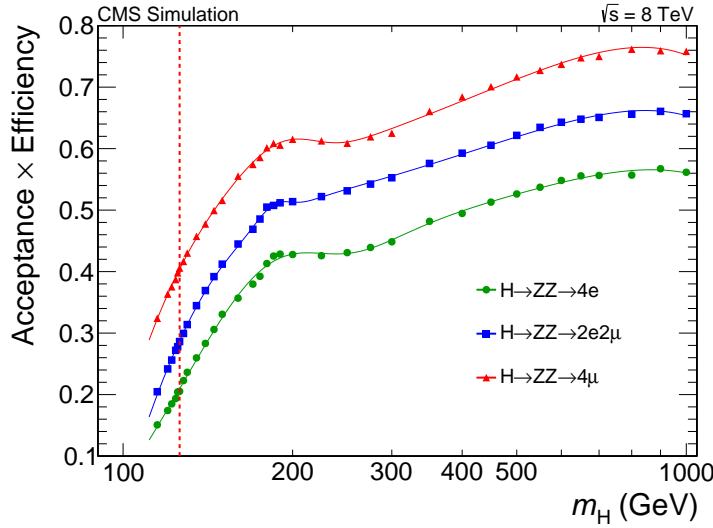


Figure 4.2: Geometrical acceptance times selection efficiency for the SM Higgs boson signal as a function of m_H in the three final states for gluon fusion production. Points represent efficiency estimated from full CMS simulation; lines represent a smooth polynomial curve interpolating the points, used in the analysis. The vertical dashed line represents $m_H = 126$ GeV [41].

the $4e$, $2e2\mu$, and 4μ channels, respectively, for $m_H = 126(200)$ GeV.

In order to improve the sensitivity to the Higgs boson production mechanisms, the event sample is split into two categories based on the jet multiplicity. These categories are defined as the 0/1-jet category, containing events with fewer than two jets, and the dijet category, containing events with at least two jets.

4.3.3 Background estimation

The dominant background contribution in the $H \rightarrow ZZ \rightarrow 4\ell$ search is irreducible and is due to direct ZZ production via $q\bar{q}$ annihilation and gluon fusion. The remaining subleading contributions arise from reducible multilepton sources, $Z + \text{jets}$, $t\bar{t}$,

CHAPTER 4. $H \rightarrow ZZ \rightarrow 4\ell$ SEARCH & PRODUCTION/DECAY FRACTIONS

and $WZ + \text{jets}$.

The expected yield and shape of the $q\bar{q} \rightarrow ZZ$ and $gg \rightarrow ZZ$ background is evaluated using the simulated events discussed above. The $gg \rightarrow ZZ$ contribution with respect to the $q\bar{q} \rightarrow ZZ$ varies from about 2% at $m_{4\ell} = 126$ GeV to 6% at $m_{4\ell} = 1$ TeV. These two background processes make up a huge fraction of the total background in this analysis. In the region $100 < m_{4\ell} < 1000$ GeV is approximately 91%, 94%, and 97% in the $4e, 2e2\mu$, and 4μ decay channels, respectively. Within the smaller range around the observed peak ($121.5 < m_{4\ell} < 130.5$ GeV) these irreducible backgrounds contribute 58%, 71%, and 86%, respectively.

The Reducible background from $Z + \text{jets}$ is estimated using two independent methods. These methods use dedicated control regions in data where there is a dilepton pair satisfying all the requirements of a Z_1 candidate and two additional leptons satisfying certain relaxed identification requirements. In both methods, the extrapolation from the control region to the signal regions is performed using the lepton misidentification probability, $f(\ell, p_T^\ell, |\eta^\ell|)$, which is defined as the fraction of non-signal leptons identified in the analysis selection criteria evaluated on a sample of enriched non-genuine electrons and muons.

The first method uses two control regions that have a Z_1 candidate and two additional leptons with the same flavor and opposite charge. There are two categories of events that satisfy the criteria, 2P2F (composed of two leptons that pass selection and two that fail the selection criteria) and 3P1F (composed of three leptons that

CHAPTER 4. $H \rightarrow ZZ \rightarrow 4\ell$ SEARCH & PRODUCTION/DECAY FRACTIONS

pass selection and one that fails). For each event i that falls into the 2P2F or 3P1F category a weight factor of $\frac{f_3^i}{1-f_3^i} \frac{f_4^i}{1-f_4^i}$ or $\frac{f_a^i}{1-f_a^i}$ for the third and/or fourth leptons. The 3P1F region will also have a contribution from the reducible background and so the contribution is reduced by a factor of $\left(1 - \frac{n_{3P1F}^{ZZ}}{N_{3P1F}}\right)$ where n_{3P1F}^{ZZ} is the estimation of irreducible ZZ events and N_{3P1F} is the total number of events in the 3P1F region. The contribution of the 2P2F to the 3P1F is also accounted for and in the end the reducible background estimation in the signal region, $N_{SR}^{reducible}$, is given by equation (4.2),

$$N_{SR}^{reducible} = \left(1 - \frac{n_{3P1F}^{ZZ}}{N_{3P1F}}\right) \sum_j^{N_{3P1F}} \frac{f_a^j}{1-f_a^j} - \sum_i^{N_{2P2F}} \frac{f_3^i}{1-f_3^i} \frac{f_4^i}{1-f_4^i}. \quad (4.2)$$

The second method uses a control region that has a Z_1 candidate and two additional leptons with the same flavor and the same charge. This method exploits the linear dependence of the $f(\ell, p_T^\ell, |\eta^\ell|)$ probability on the fraction of loose electrons with tracks have one missing hit in the pixel detector $r_{\text{miss}}(p_T^e, |\eta^e|)$, which is indicative of a possible FSR photon conversion. This r_{miss} fraction is estimated using samples with different FSR contributions and the $f(\ell, p_T^\ell, |\eta^\ell|)$ is corrected to $\tilde{f}(\ell, p_T^\ell, |\eta^\ell|)$ using the corresponding r_{miss} fraction. The expected number of reducible background events in the signal region is given by equation (4.3), where $N_{2P2F_{SS}}$ is the number of observed events in the same-sign 2P2F region. The ratio $r_{OS/SS}$ between the number of events in the 2P2F opposite-sign and same-sign control regions is obtained from simulation.

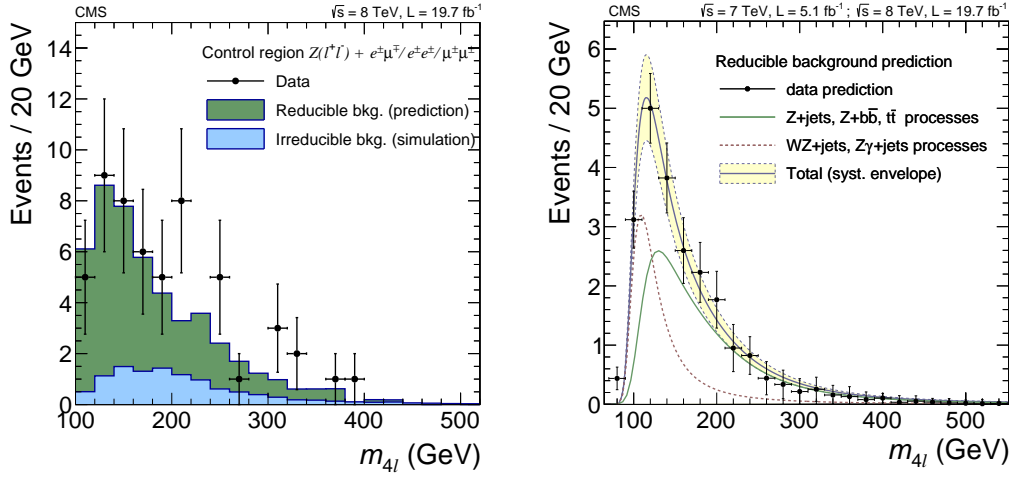


Figure 4.3: (left) Validation of the method using the SS control sample. The observed $m_{4\ell}$ distribution (black dots), prediction of the reducible background (dark green area), and expected contributions from ZZ (light blue area) are shown. (right) Prediction for the reducible background in all three decay channels together (black dots) fitted using an empirical shape (blue curve) with indicated total uncertainty (yellow band). The contributions from the 2P2F-like (solid green) and 3P1F-like (dashed red) processes are fitted separately [41].

$$N_{\text{SR}}^{\text{reducible}} = r_{\text{OS/SS}} \cdot \sum_i^{N_{\text{2P2LSS}}} \tilde{f}_3^i \cdot \tilde{f}_4^i \quad (4.3)$$

Both of these two reducible background estimations agree well within their statistical uncertainties. Such good agreement allows the analysis to combine the two estimations of the background together, assigning a systematic uncertainty of 20%, 25%, and 40% for the $4e$, $2e2\mu$, and 4μ decay channels, respectively. Validations of these two methods are shown in figure 4.3.

After all of this simulation, extrapolation, and calculation we can estimate the number of collision events we would expect to observe for the SM backgrounds and

Table 4.1: The number of observed candidate events compared to the mean expected background and signal rates for each final state. Uncertainties include statistical and systematic sources. The results are given integrated over the full mass measurement range $m_{4\ell} > 100$ GeV and for 7 and 8 TeV data combined [41].

Decay Channel	$4e$	$2e2\mu$	4μ	4ℓ
ZZ background	77 ± 10	191 ± 25	119 ± 15	387 ± 31
$Z + \text{jets}$ background	7.4 ± 1.5	11.5 ± 2.9	3.6 ± 1.5	22.6 ± 3.6
All backgrounds	85 ± 11	202 ± 25	123 ± 15	410 ± 31
$m_H = 500$ GeV	5.2 ± 0.6	12.2 ± 1.4	7.1 ± 0.8	24.5 ± 1.7
$m_H = 800$ GeV	0.7 ± 0.1	1.6 ± 0.2	0.9 ± 0.1	3.1 ± 0.2
Observed	89	247	134	470

for the Higgs boson under different mass hypotheses. In the full analysis region $m_{4\ell} > 100$ GeV these estimations and the statistical and systematic uncertainty on them is shown in table 4.1.

4.4 Kinematic Distributions

Beyond counting the number of observed and expected collision events within the signal region, this analysis utilizes three kinematic distributions to separate potential signal events from background SM production. The first is the $m_{4\ell}$ shape, second is a kinematic discriminant based on the matrix elements of both signal and background processes, the third is either the $p_T^{4\ell}$ or jet kinematic discriminant depending on the

number of jets observed in addition to the four leptons.

4.4.1 4ℓ mass spectrum

The background from ZZ and $Z + \text{jets}$ processes dominates after the event selection. The reconstructed four-lepton invariant mass distribution for the combined $4e$, $2e2\mu$, and 4μ channels is shown in figure 4.4 and compared with the expectations from background processes.

The normalization and shape of the ZZ background are obtained from simulation, while the normalization of the reducible background is estimated from control samples in data, as described in section 4.3.3. The $m_{4\ell}$ shape of the reducible background component is obtained from the opposite-sign method by fitting the $m_{4\ell}$ distributions of 2P2F and 3P1F regions separately with empirical functional forms built from Landau and exponential distributions. The systematic uncertainty in the shape is determined by the envelope that covers alternative functional forms or alternative binning.

The signal $m_{4\ell}$ shapes are also obtained from simulation. For low-mass Higgs boson hypotheses ($m_H < 400$ GeV), the Higgs boson line shape is described with a relativistic Breit-Wigner (BW) convolved with a double-sided Crystal-Ball (CB) distribution to parameterize the reconstructed signal $m_{4\ell}$ distributions. The resulting model for the $m_{4\ell}$ peak can be seen in figure 4.5, where the parameterization for each final state can be seen superimposed on simulated data events. At high

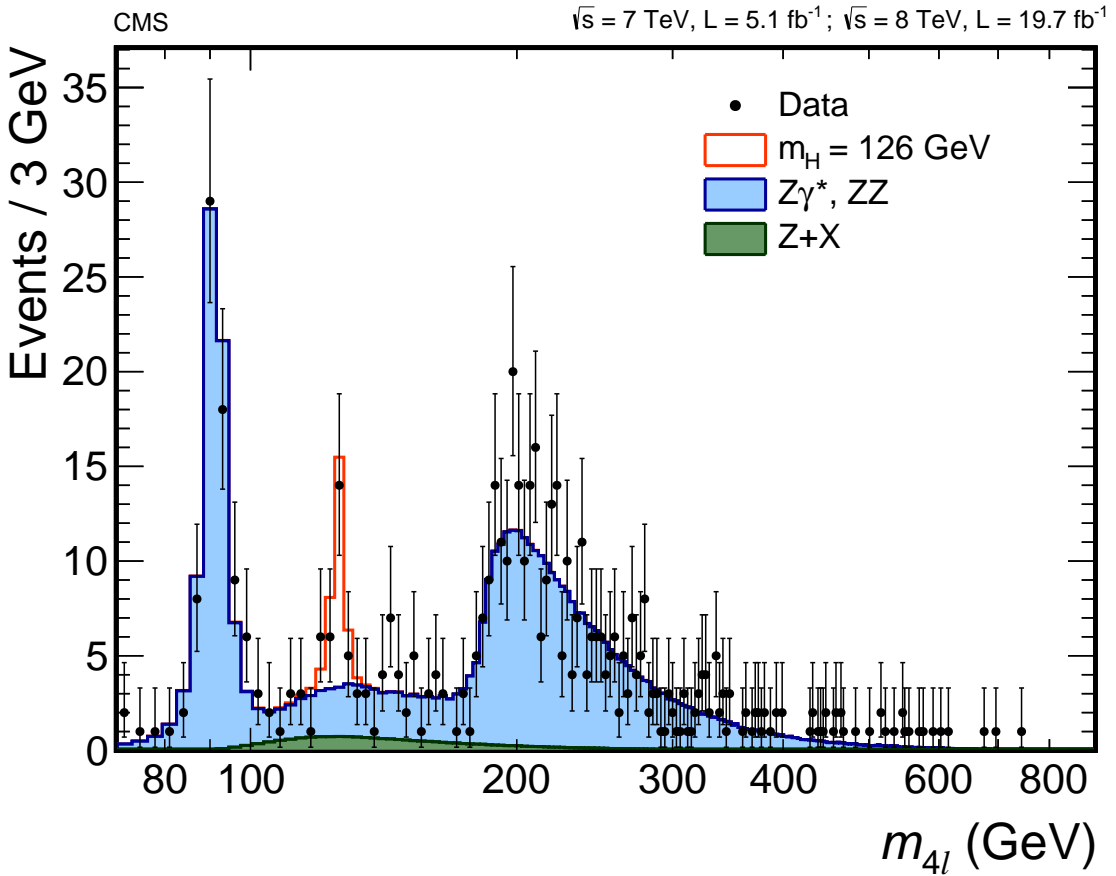


Figure 4.4: Distribution of the four-lepton reconstructed mass in the full mass range $70 < m_{4\ell} < 1000 \text{ GeV}$ for the sum of the $4e$, $2e2\mu$, and 4μ channels. Points with error bars represent the data, shaded histograms represent the backgrounds, and the unshaded histogram represents the signal expectation for a mass hypothesis of $m_H = 126 \text{ GeV}$. Signal and the ZZ background are normalized to the SM expectation; the $Z +$ jets background to the estimation from data. The expected distributions are presented as stacked histograms. No events are observed with $m_{4\ell} > 800 \text{ GeV}$ [41].

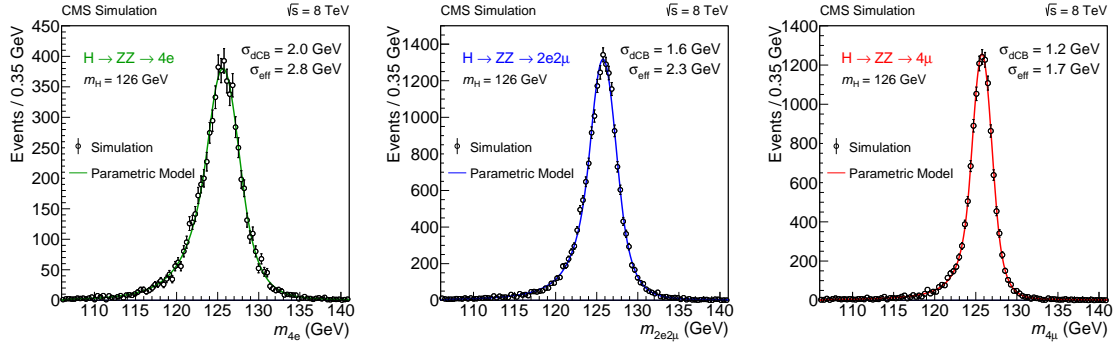


Figure 4.5: The $H \rightarrow ZZ \rightarrow 4\ell$ invariant mass distribution for $m_H = 126$ GeV in the (left) $4e$, (center) $2e2\mu$, and (right) 4μ channels. The distributions are fitted with a double-sided CB function and the fitted values of the CB width σ_{dCB} are indicated. The values of effective resolution, defined as half the smallest width that contains 68.3% of the distribution, are also indicated. The distributions are arbitrarily normalized [41].

mass ($m_H > 400$ GeV), the line shape is described using the complex pole scheme (CPS) [57, 112, 113]. This results in a Higgs boson width much larger than the four-lepton mass resolution. The signal parameterization for these hypotheses are modified according to this increased width instead of using the double CB functions. Systematics on the line shape are incorporated by varying the signal weights as a function of the Higgs boson mass by $\pm 1\sigma$.

4.4.2 Matrix Element Likelihood Approach (MELA)

kinematic discriminant

As we have mentioned the four-lepton decay mode has the advantage that the kinematics of the Higgs boson and its decay products are all visible in the detector,

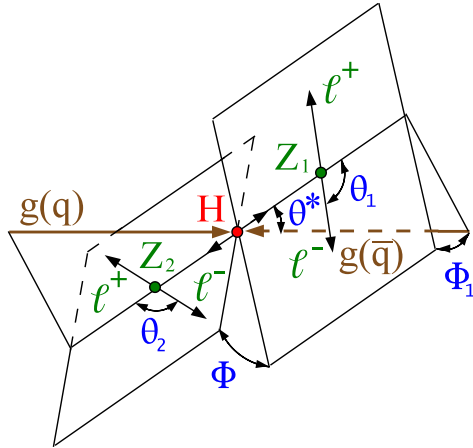


Figure 4.6: Illustration of the production and decay of a particle H , $gg(q\bar{q}) \rightarrow H \rightarrow ZZ \rightarrow 4\ell$, with the two production angles θ^* and Φ_1 shown in the H rest frame and three decay angles θ_1 , θ_2 , and Φ shown in the Z_1 , Z_2 , and H rest frames, respectively [60].

providing many independent observables that can be used for different purposes. In addition to the invariant mass, the angular distributions for the four leptons and the dilepton pairs invariant masses can be used to further discriminate signal from background, increasing the sensitivity and reducing the statistical uncertainty in the observations.

Five angles $\vec{\Omega} \equiv (\theta^*, \Phi_1, \theta_1, \theta_2, \Phi)$ [60, 62, 63, 114] seen in figure 4.6 and the invariant masses of the lepton pairs m_{Z_1} and m_{Z_2} , fully describe the kinematic configuration of a four-lepton system in its center-of-mass frame, up to an arbitrary rotation around the beam axis. These observables provide significant discriminating power between signal and background. A matrix-element likelihood approach (MELA) is used to construct a kinematic discriminant related to the decay observables [68, 115].

Each of these five observables carries some information about how the 4ℓ event

CHAPTER 4. $H \rightarrow ZZ \rightarrow 4\ell$ SEARCH & PRODUCTION/DECAY FRACTIONS

was produced. The distribution of these is shown in figure 4.7. This figure also shows predicted distributions for BSM bosons, which will become relevant in later sections. In principle, with enough computing power and effort one could construct an analysis that uses all of them independently. However, without loss in performance one can use the event probabilities that come from the matrix-element corresponding to a given point in phase space. This way the analysis is simplified and the correlations between these different variables are maintained.

To separate a SM signal ($J^P = 0^+$) from background a kinematic discriminant ($\mathcal{D}_{\text{bkg}}^{\text{kin}}$) is defined based on the event probabilities $\mathcal{P}(m_{Z_1}, m_{Z_1}, \vec{\Omega} | m_{4\ell})$ of the background or signal probability distribution of angular and mass observables computed from the LO matrix element squared for signal or ZZ processes. This discriminant is defined as in equation (4.4), giving the added advantage that to first order acceptance and phase space factors will cancel in the ratio. Thus, one does not need to integrate the matrix elements over the full kinematic range but simply calculate the magnitude of the matrix element squared at the point in phase space where each event appears.

The expected $\mathcal{D}_{\text{bkg}}^{\text{kin}}$ shapes for signal and the $q\bar{q} \rightarrow ZZ$ and $gg \rightarrow ZZ$ backgrounds are taken from simulation of the three decay channels $4e$, $2e2\mu$, and 4μ independently. Given the low statistics and unreliable simulation of the $Z + \text{jets}$ contribution is modeled by collision events in the control regions. The statistics are boosted by merging all decay channels and control regions together using the appropriate weight to map them to the signal region.

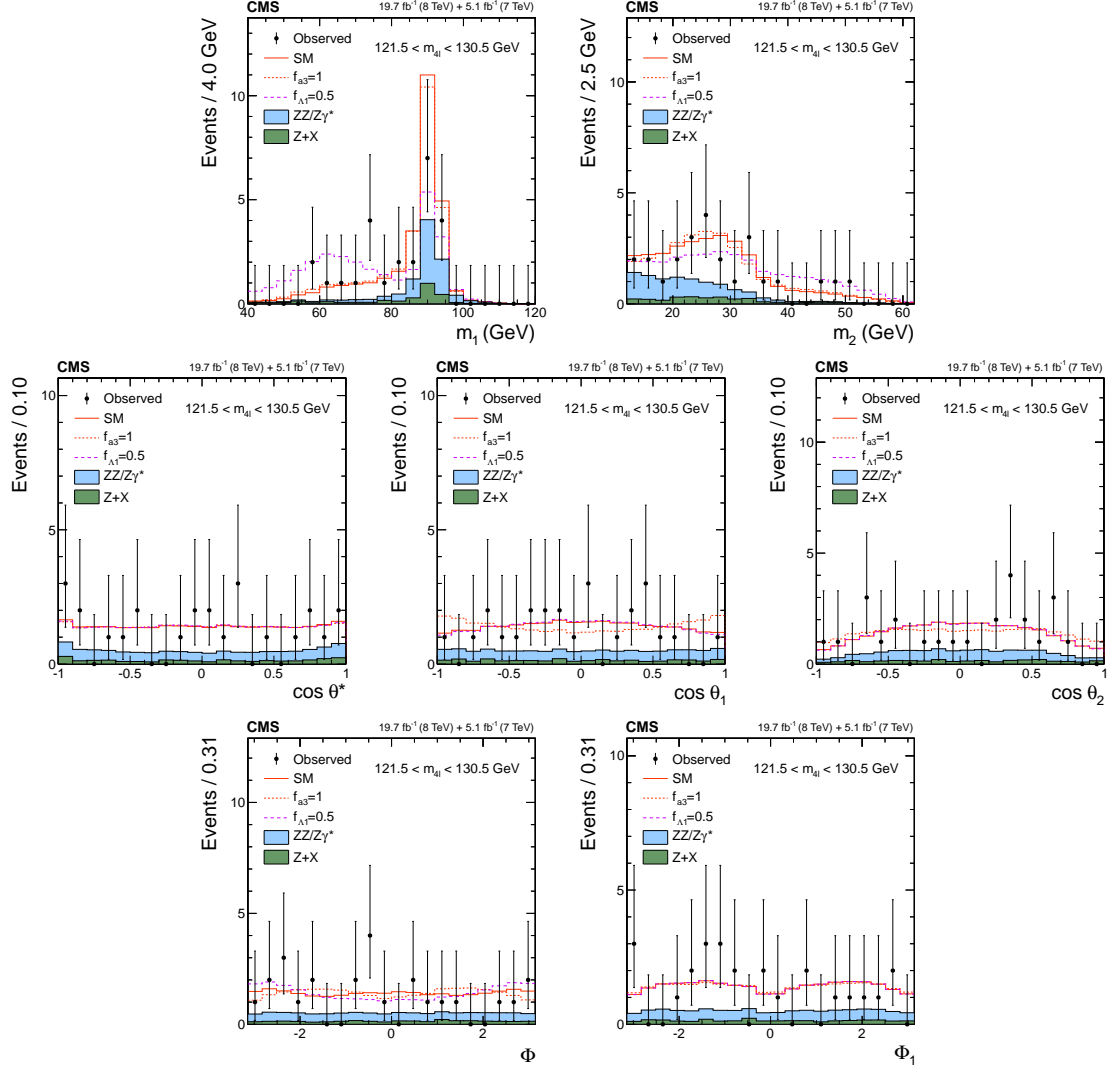


Figure 4.7: Distributions of the eight kinematic observables used in the $H \rightarrow ZZ \rightarrow 4\ell$ analysis: m_{Z_1} , m_{Z_2} , $\cos \theta^*$, $\cos \theta_1$, $\cos \theta_2$, Φ , and Φ_1 . The observed data (points with error bars), the expectations for the SM background (shaded areas), the SM Higgs boson signal (open areas under the solid histogram), and the alternative spin-zero resonances (open areas under the dashed histograms) are shown, as indicated in the legend. The mass of the resonance is taken to be 125.6 GeV and the SM cross section is used. All distributions, with the exception of $m_{4\ell}$, are presented with the requirement $121.5 < m_{4\ell} < 130.5 \text{ GeV}$ [61].

$$\mathcal{D}_{\text{bkg}}^{\text{kin}} = \frac{\mathcal{P}_{0^+}^{\text{kin}}}{\mathcal{P}_{0^+}^{\text{kin}} + \mathcal{P}_{\text{bkg}}^{\text{kin}}} = \left[1 + \frac{\mathcal{P}_{\text{bkg}}^{\text{kin}}(m_{Z_1}, m_{Z_2}, \vec{\Omega} | m_{4\ell})}{\mathcal{P}_{0^+}^{\text{kin}}(m_{Z_1}, m_{Z_2}, \vec{\Omega} | m_{4\ell})} \right]^{-1}. \quad (4.4)$$

Because these discriminant values do not directly carry $m_{4\ell}$ discrimination power they are used as a second dimensions for discrimination between signal and background. The distributions of the $\mathcal{D}_{\text{bkg}}^{\text{kin}}$ versus $m_{4\ell}$ are shown for the selected events and compared to the SM background expectation in figure 4.8. The distribution of events in the $(m_{4\ell}, \mathcal{D}_{\text{bkg}}^{\text{kin}})$ plane agrees well with the SM background expectation in the high-mass range, figure 4.8 (right), while discrepancies in the two-dimensional plane are observed in the low-mass range $110 < m_{4\ell} < 180$ GeV, figure 4.8 (left), indicative of the presence of a signal.

Figure 4.9 (left) shows the same data points as in figure 4.8 (left), but compared with the expected distribution from SM backgrounds plus the contribution of a Higgs boson with $m_H = 126$ GeV. A signal-like clustering of events is apparent at high values of $\mathcal{D}_{\text{bkg}}^{\text{kin}}$ and for $m_{4\ell} \approx 126$ GeV. Figure 4.9 (right) shows the distribution of the kinematic discriminant $\mathcal{D}_{\text{bkg}}^{\text{kin}}$ in the mass region $121.5 < m_{4\ell} < 130.5$ GeV.

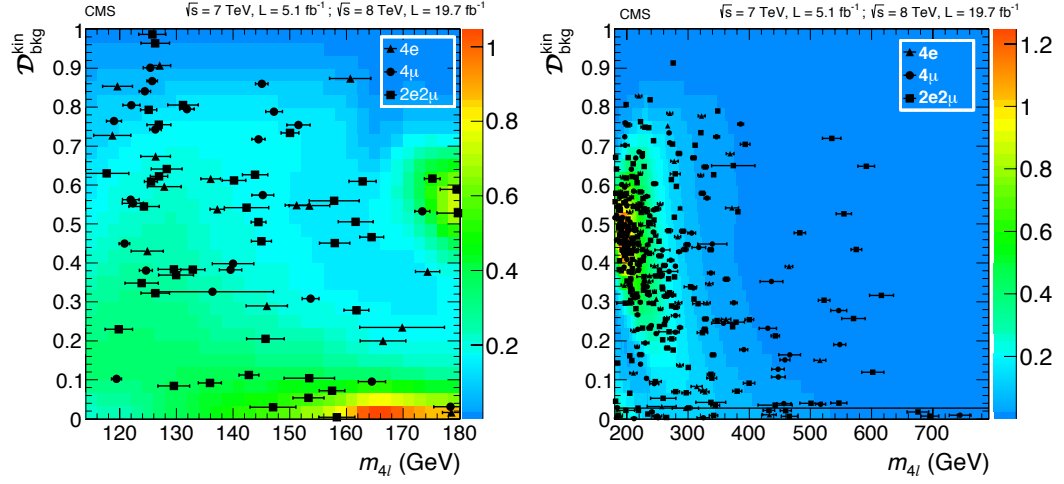


Figure 4.8: Distribution of the kinematic discriminant $D_{\text{bkg}}^{\text{kin}}$ versus the four-lepton reconstructed mass $m_{4\ell}$ in the (left) low-mass and (right) high-mass regions. The color scale represents the expected relative density in linear scale (in arbitrary units) of background events. The points show the data and the measured per-event invariant mass uncertainties as horizontal bars. One $2e2\mu$ event with $m_{4\ell} \approx 220 \text{ GeV}$ and small $D_{\text{bkg}}^{\text{kin}}$ has a huge mass uncertainty, and it is displayed as the horizontal line. No events are observed for $m_{4\ell} > 800 \text{ GeV}$ [41].

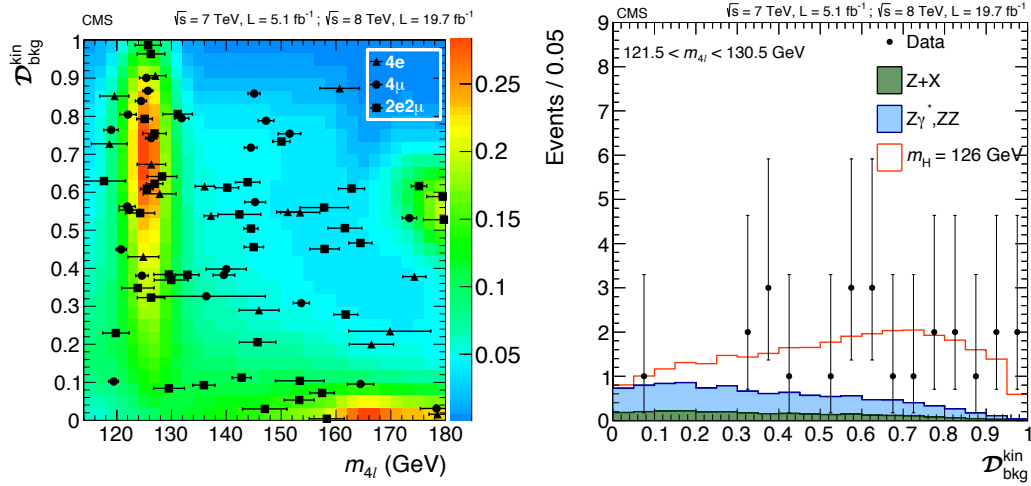


Figure 4.9: (left) Distribution of $\mathcal{D}_{\text{bkg}}^{\text{kin}}$ versus $m_{4\ell}$ in the low-mass range with colors shown for the expected relative density in linear scale (in arbitrary units) of background plus the Higgs boson signal for $m_H = 126$ GeV. The points show the data, and horizontal bars represent the measured mass uncertainties. (right) Distribution of the kinematic discriminant $\mathcal{D}_{\text{bkg}}^{\text{kin}}$ for events in the mass region $121.5 < m_{4\ell} < 130.5$ GeV. Points with error bars represent the data, shaded histograms represent the backgrounds, and the unshaded histogram the signal expectation. Signal and background histograms are stacked [41].

4.4.3 $p_T^{4\ell}$ and Jet Kinematic Discriminant

While in the dominant gluon fusion mechanism the Higgs boson is the most likely way to produce a Higgs boson at the LHC, the cross section for VBF production is only about 1 order of magnitude smaller than that for the gluon fusion process. In the vector-boson scattering process, the two initial-state quarks deviate at a polar angle large enough such that as final-state quarks they create measurable additional jets in the event. These two jets, being remnants of the incoming proton beams, have typically a large separation in η and high momentum. These characteristics are used to distinguish gluon fusion from VBF Higgs boson production in the analysis. Jets in the final state also come from $t\bar{t}H$ and VH production, where the V decays hadronically.

In the 0/1-jet category, the transverse momentum of the four-lepton system ($p_T^{4\ell}$) is used to distinguish VBF production and associated production with a weak boson, VH , from gluon fusion, discrimination power seen in figure 4.10 (top right). In the dijet category, a linear discriminant (\mathcal{D}_{jet}) is formed combining two VBF-sensitive variables, the absolute difference in pseudorapidity ($|\Delta\eta_{jj}|$) and the invariant mass of the two leading jets (m_{jj}). The discriminant maximizes the separation between vector-boson and gluon fusion processes. In the 0/1-jet (dijet) category, about 5% (20%) of the signal events are expected to come from the VBF production mechanism, as estimated from simulation. Simulations of these distributions are shown in figure 4.10.

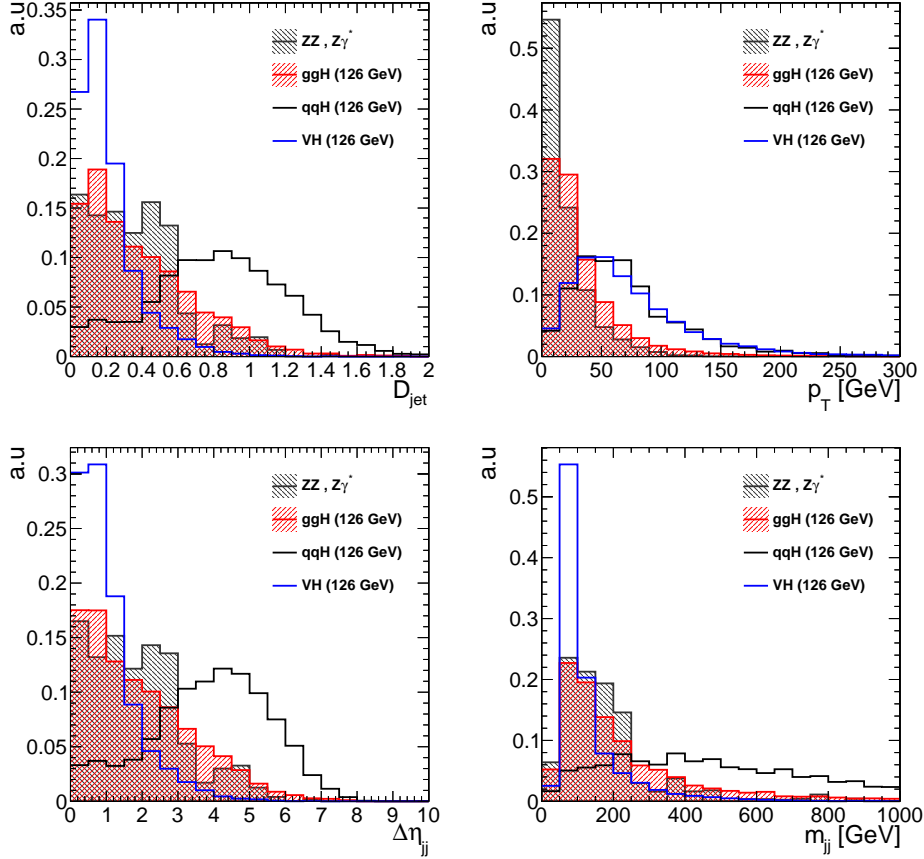


Figure 4.10: Main observables discriminating production mechanisms in 0/1 jet and Dijet categories in arbitrary units. $q\bar{q}H$ is used in these figures for VBF production. (top left) D_{jet} Discriminant combining VBF discrimination variables. (top right) p_T of the four-lepton system. (bottom left) $\Delta\eta$ of the two leading jets. (bottom right) Invariant mass of the two jets.

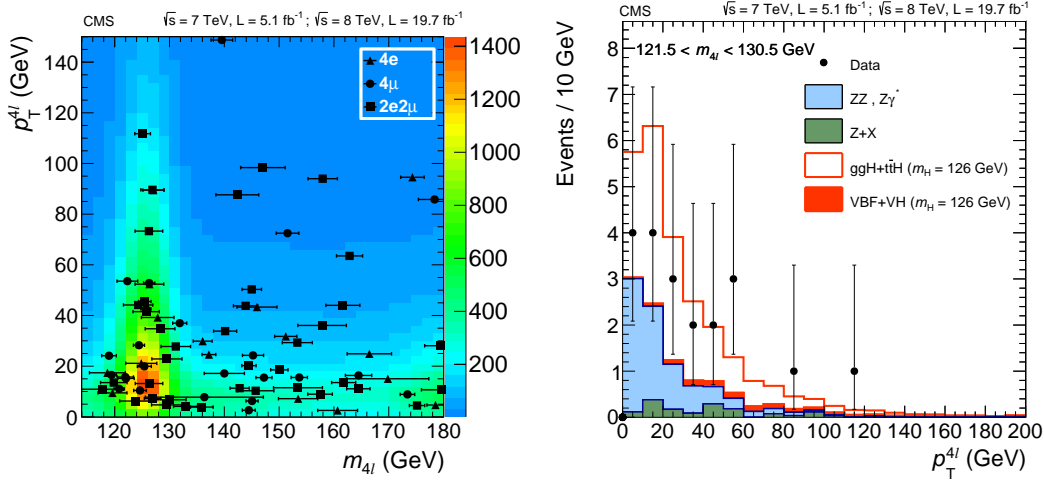


Figure 4.11: (left) Distribution of $p_T^{4\ell}$ versus $m_{4\ell}$ in the low-mass-range 0/1-jet category with colors shown for the expected relative density in linear scale (in arbitrary units) of background plus the Higgs boson signal for $m_H = 126$ GeV. No events are observed for $p_T^{4\ell} > 150$ GeV. The points show the data, and horizontal bars represent the measured mass uncertainties. (right) Distribution of $p_T^{4\ell}$ in the 0/1-jet category for events in the mass region $121.5 < m_{4\ell} < 130.5$ GeV. Points with error bars represent the data, shaded histograms represent the backgrounds, and the red histograms represent the signal expectation, broken down by production mechanism. Signal and background histograms are stacked [41].

For the final analysis, the distribution of the transverse momentum of the 4ℓ system in the 0/1-jet category and its joint distribution with $m_{4\ell}$ are shown in figure 4.11. The p_T spectrum shows good agreement with a SM Higgs boson hypothesis with $m_H = 126$ GeV in the 0/1-jet category with few events having $p_T > 60$ GeV, where VBF and VH production are relatively more relevant.

The distribution of the production mechanism discriminant in the dijet category and its joint distribution with $m_{4\ell}$ are shown in figure 4.12. Good agreement is found with the expectation from simulation, which predicts a negligible background and

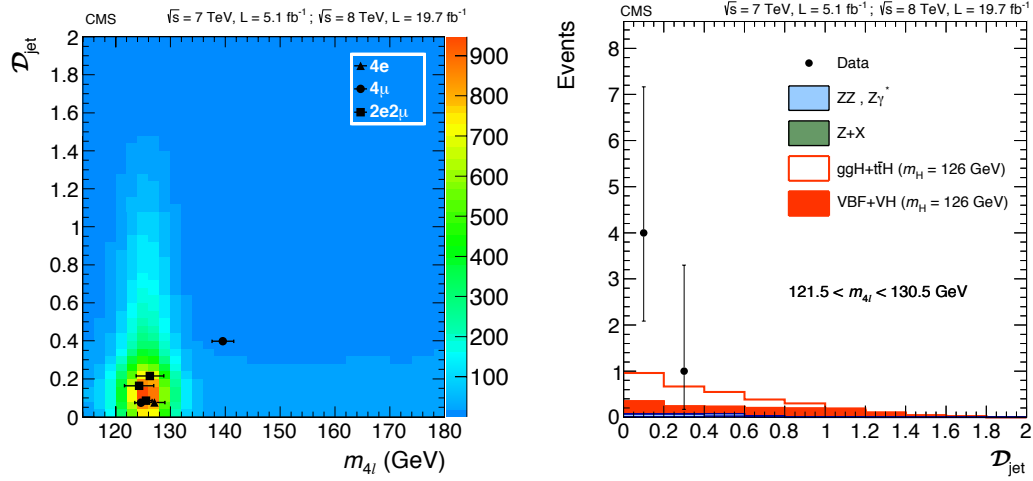


Figure 4.12: (left) Distribution of \mathcal{D}_{jet} versus $m_{4\ell}$ in the low-mass-range dijet category with colors shown for the expected relative density in linear scale (in arbitrary units) of background plus the Higgs boson signal for $m_H = 126$ GeV. The points show the data and horizontal bars represent the measured mass uncertainties. (right) Distribution of \mathcal{D}_{jet} in the dijet category for events in the mass region $121.5 < m_{4\ell} < 130.5$ GeV. Points with error bars represent the data, shaded histograms represent the backgrounds, and the red histograms represent the signal expectation, broken down by production mechanism. Signal and background histograms are stacked [41].

a fraction of 42% of the signal events arising from vector-boson-induced production (VBF and VH). No events with a high rank of the \mathcal{D}_{jet} ($\mathcal{D}_{\text{jet}} > 0.5$) discriminant are observed.

4.5 Search Results

In the low mass region of the analysis, an excess of events observed in the 4ℓ mass spectrum localized in a narrow region in the vicinity of 126 GeV. The $m_{4\ell}$ distribution for the sum of the $4e$, $2e2\mu$, and 4μ channels, in the mass region $70 < m_{4\ell} < 180$ GeV,

CHAPTER 4. $H \rightarrow ZZ \rightarrow 4\ell$ SEARCH & PRODUCTION/DECAY FRACTIONS

Table 4.2: The number of observed candidate events compared to the mean expected background and signal rates for each final state. Uncertainties include statistical and systematic sources. The results are integrated over the mass range from 121.5 to 130.5 GeV and for 7 and 8 TeV data combined [41].

Decay Channel	$4e$	$2e2\mu$	4μ	4ℓ
ZZ background	1.1 ± 0.1	3.2 ± 0.2	2.5 ± 0.2	6.8 ± 0.3
$Z +$ jets background	0.8 ± 0.2	1.3 ± 0.3	0.4 ± 0.2	2.6 ± 0.4
All backgrounds	1.9 ± 0.2	4.6 ± 0.4	2.9 ± 0.2	9.4 ± 0.5
$m_H = 125$ GeV	3.0 ± 0.4	7.9 ± 1.0	6.4 ± 0.7	17.3 ± 1.3
$m_H = 126$ GeV	3.4 ± 0.5	9.0 ± 1.1	7.2 ± 0.8	19.6 ± 1.5
Observed	4	13	8	25

is shown in figure 4.13. Around the observed peak, near $m_{4\ell} = 126$ GeV the expected and observed candidate event yields are given in table 4.2. Split into the categories according to the number of jets in the final state, in addition to the final state leptons, the expected and observed number of collision events is seen in table 4.3.

Experimental systematic uncertainties in the normalization of the signal and the irreducible background processes are evaluated from data for the trigger and the combined lepton reconstruction, identification, and isolation efficiencies. Data is used to validate the absolute momentum scale and resolution resulting in effects of 0.3% ($4e$), 0.1% ($2e2\mu$), and 0.1% (4μ) on the mass scale. The effect of the energy resolution uncertainties is taken into account by introducing a 20% uncertainty in the simulated width of the signal mass peak, according to the maximum deviation between data and

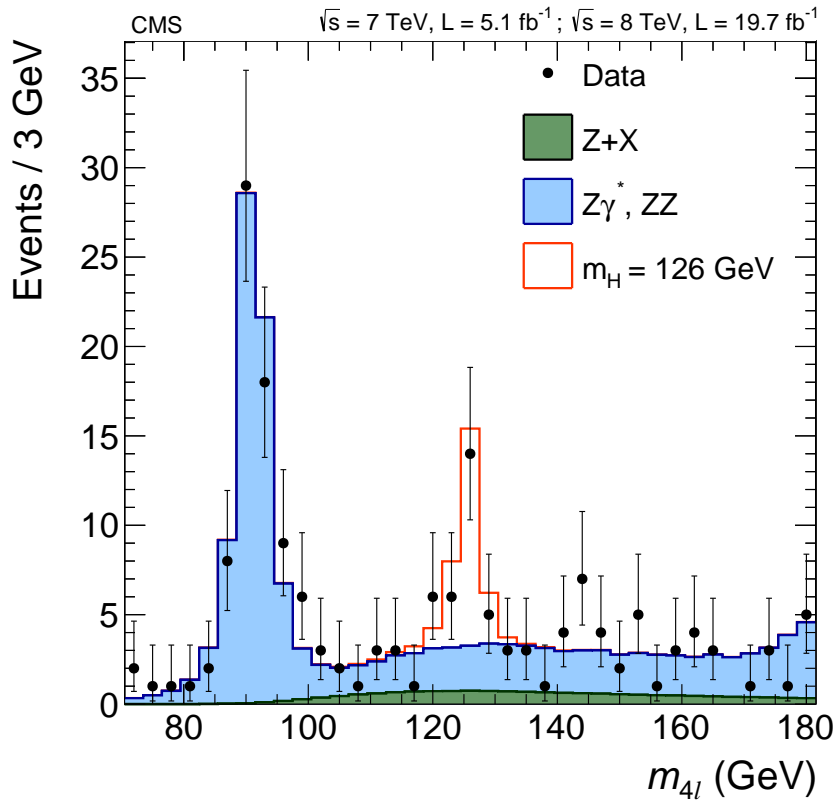


Figure 4.13: Distribution of the four-lepton reconstructed mass for the sum of the $4e$, $2e2\mu$, and 4μ channels for the mass region $70 < m_{4\ell} < 180$ GeV. Points with error bars represent the data, shaded histograms represent the backgrounds, and the unshaded histogram represents the signal expectation for a mass hypothesis of $m_H = 126$ GeV. Signal and the ZZ background are normalized to the SM expectation, the $Z +$ jets background to the estimation from data [41].

Table 4.3: The number of observed candidate events compared to the mean expected background and signal rates for the sum of the three final states for each of the two analysis categories. Uncertainties include statistical and systematic sources. The results are integrated over the mass range from 121.5 to 130.5 GeV and for 7 and 8 TeV data combined. The expected signal yield for a SM Higgs boson with $m_H = 126$ GeV is reported, broken down by the production mechanism [41].

Category	0/1-jet	Dijet
ZZ background	6.4 ± 0.3	0.38 ± 0.02
$Z + \text{jets}$ background	2.0 ± 0.3	0.5 ± 0.1
All backgrounds	8.5 ± 0.5	0.9 ± 0.1
$gg \rightarrow H$	15.4 ± 1.2	1.6 ± 0.3
$t\bar{t} \rightarrow H$	NA	0.08 ± 0.01
VBF	0.70 ± 0.03	0.87 ± 0.07
WH	0.28 ± 0.01	0.21 ± 0.01
ZH	0.21 ± 0.01	0.16 ± 0.01
All signal, $m_H = 126$ GeV	16.6 ± 1.3	3.0 ± 0.4
Observed	20	5

CHAPTER 4. $H \rightarrow ZZ \rightarrow 4\ell$ SEARCH & PRODUCTION/DECAY FRACTIONS

simulation observed in $Z \rightarrow \ell^+\ell^-$ events. Due to low statistics in the control regions systematic uncertainties of 20%, 25%, and 40% are assigned to the normalization of the reducible background for the $4e$, $2e2\mu$, and 4μ final states, respectively. The uncertainty in the luminosity measurement (2.2% at 7 TeV and 2.6% at 8 TeV) [116,117] is also applied to all hypothetical signals and backgrounds.

The theoretical uncertainties in the irreducible background are computed as functions of $m_{4\ell}$, varying both the renormalization and factorization scales and the parton distribution function set. Systematic uncertainties in the Higgs boson cross section and branching fraction are taken from [54,118]. In the 0/1-jet category, an additional background normalization is assigned to account for the differences in Monte Carlo predictions, while an additional signal systematics are assigned in the dijet category to account for cross section uncertainties in $H + \text{jets}$ and VBF production. A summary of the systematic uncertainties in the normalizations of the signal and background processes is given in table 4.4.

Shape uncertainties are applied to all three kinematic distributions used in the analysis. In the $m_{4\ell}$ dimension shape variations are used to account for variations due to the lepton scale and resolution impacts. In the $\mathcal{D}_{\text{bkg}}^{\text{kin}}$ dimension shape variations are used for the uncertainty in the $Z + \text{jets}$ shape. In the 0/1-jet category the $p_T^{4\ell}$ shape is assigned a systematic to account for the theoretical uncertainty in the shape. Both theoretical and experimental (jet energy scale and resolution) shape systematics are assigned to the \mathcal{D}_{jet} distribution.

Table 4.4: Effect of systematic uncertainties on the yields of signal ($m_H = 126$ GeV) and background processes for the 8 TeV data set and 0/1-jet category. Uncertainties appearing on the same line are 100% correlated, with two exceptions: those related to the missing higher orders are not correlated, and those from the α_S + PDF (gg) in $t\bar{t}H$ are 100% anticorrelated. Uncertainties for the 7 TeV data set are similar [41].

Source	Signal ($m_H = 126$ GeV)				Backgrounds		
	$gg \rightarrow H$	VBF	VH	$t\bar{t}H$	$q\bar{q} \rightarrow ZZ$	$gg \rightarrow ZZ$	$Z + \text{jets}$
α_S + PDF (gg)	7.2%	—	—	7.8%	—	7.2%	—
α_S + PDF ($q\bar{q}$)	—	2.7%	3.5%	—	3.4%	—	—
Higher orders	7.5%	0.2%	0.4%, 1.6%	6.6%	2.9%	24%	—
Signal acceptance			2%		—	—	—
$\text{BR}(H \rightarrow ZZ)$			2%		—	—	—
Luminosity				2.6%			—
Electron efficiency				10% (4e), 4.3% (2e2 μ)			—
Muon efficiency				4.3% (4 μ), 2.1% (2e2 μ)			—
Control region	—	—	—	—	—	—	40%

4.5.1 Quantifying the observation

To quantify this observation and to account for all the necessary uncertainties in our analysis procedure a three-dimensional unbinned maximum-likelihood fit is performed on the selected collision events. The fits include probability density functions for five signal components (gluon fusion, VBF, WH , ZH , and $t\bar{t}H$ productions) and three background processes ($q\bar{q} \rightarrow ZZ$, $gg \rightarrow ZZ$, and $Z + \text{jets}$). The normalizations of these components and systematic uncertainties are introduced in the fits as nuisance parameters, assuming log-normal *a priori* probability distributions, and are profiled during the minimization. The shapes of the probability density functions for the event observables are also varied within alternative shapes as experimental or theoretical systematic uncertainties.

The three main questions for the analysis to quantitatively answer are:

- (1) What Higgs boson hypotheses can we exclude?
- (2) What is the statistical significance of any observed deviation from the SM expectations?
- (3) Does the measured cross section times branching ratio match the SM Higgs boson expectation?

The likelihood that is used to address these questions is given in equation (4.5) where m_H, Γ are the Higgs boson mass and width and the other discriminants are defined in the previous section. In total, the selected events are split into twelve subcategories

CHAPTER 4. $H \rightarrow ZZ \rightarrow 4\ell$ SEARCH & PRODUCTION/DECAY FRACTIONS

based on the three final states, two data-taking periods (7 & 8 TeV), and two jet categories. The events are examined for 187 hypothetical SM-like Higgs boson masses in a range between 110 and 1000 GeV.

$$\mathcal{L}_{3D}^\mu \equiv \mathcal{L}_{3D}^{\mu, 0/1\text{-jet}}(m_{4\ell}, \mathcal{D}_{\text{bkg}}^{\text{kin}}, p_T^{4\ell}) = \mathcal{P}(m_{4\ell}|m_H, \Gamma) \mathcal{P}(\mathcal{D}_{\text{bkg}}^{\text{kin}}|m_{4\ell}) \mathcal{P}(p_T^{4\ell}|m_{4\ell}) \quad (4.5)$$

$$\mathcal{L}_{3D}^\mu \equiv \mathcal{L}_{3D}^{\mu, \text{Dijet}}(m_{4\ell}, \mathcal{D}_{\text{bkg}}^{\text{kin}}, \mathcal{D}_{\text{jet}}) = \mathcal{P}(m_{4\ell}|m_H, \Gamma) \mathcal{P}(\mathcal{D}_{\text{bkg}}^{\text{kin}}|m_{4\ell}) \mathcal{P}(\mathcal{D}_{\text{jet}}|m_{4\ell})$$

Question (1) is answered by fitting the data for exclusion limits as a function of the Higgs boson hypothesis mass m_H . Exclusion limits are determined by fitting the data using the CL_s frequentist construction [119, 120] to determine the range of masses that are excluded at 95% confidence level (C.L.). Generally, this is done by fitting both data, under the assumption of a specific Higgs boson mass m_H , and many pseudo-datasets for the *signal strength* ($\mu = \sigma/\sigma_{SM}$), the ratio of the observed and expected SM cross section times branching ratio. Once the fit to data is performed, the 95% confidence level (C.L.) upper limit on μ is determined from the distribution of pseudo-data experiments. When this upper limit gives $\mu > 1$ the data is consistent (within 95%) with both signal+background and background only hypotheses at that mass m_H . The region where the upper limit is at a $\mu < 1$ is the *excluded range* where the data to a 95% C.L. excludes the signal+background hypothesis at that mass.

The result of the 187 fits of the \mathcal{L}_{3D}^μ likelihood are shown in figure 4.14. Here one

CHAPTER 4. $H \rightarrow ZZ \rightarrow 4\ell$ SEARCH & PRODUCTION/DECAY FRACTIONS

can see the observed 95% C.L. upper limit on μ for each mass point. Additionally the median, $\pm 1\sigma$, and $\pm 2\sigma$ expected exclusion for background-only fit are shown as a dashed line, green band, and yellow bands respectively. From this plot, Higgs boson hypotheses with masses $m_H \in [115\text{--}750 \text{ GeV}]$ were expected to be excluded at a 95% C.L. using the four-lepton final state, a large fraction of the 110–1000 GeV analysis range. From the observed number of events, bosons with masses between 114.5–119.0 GeV and 129.5–832.0 GeV can actually be excluded at a 95% C.L. using the four-lepton final state. The unexcluded region between $m_H \in 119.0\text{--}129.5 \text{ GeV}$ corresponds to the excess that is seen in figure 4.13.

Question (2) is answered by computing the local p-value from the \mathcal{L}_{3D}^μ likelihood, these represent the the significance of a local excess relative to the background expectation, are shown for the full mass range as a function m_H in figure 4.15 (left) and near the peak in figure 4.15 (right). The minimum of the local p-value is reached around $m_{4\ell} = 125.7 \text{ GeV}$, and corresponds to a local significance of 6.8σ , consistent with the expected sensitivity of 6.7σ . These values measure the number of standard deviations that the median background distributions would have to fluctuate in order to ‘fake’ the signal that we observe.

As a cross-check, 1D [$\mathcal{L}_{1D}^\mu \equiv \mathcal{L}_{1D}^\mu(m_{4\ell})$] and 2D [$\mathcal{L}_{2D}^\mu \equiv \mathcal{L}_{2D}^\mu(m_{4\ell}, \mathcal{D}_{\text{bkg}}^{\text{kin}})$] models are also studied, as shown in figures 4.15 (left) and (right), resulting in an observed local significance of 5.0σ and 6.9σ , for an expectation of 5.6σ and 6.6σ , respectively. These results are consistent with the 3D model; however, with a systematically lower

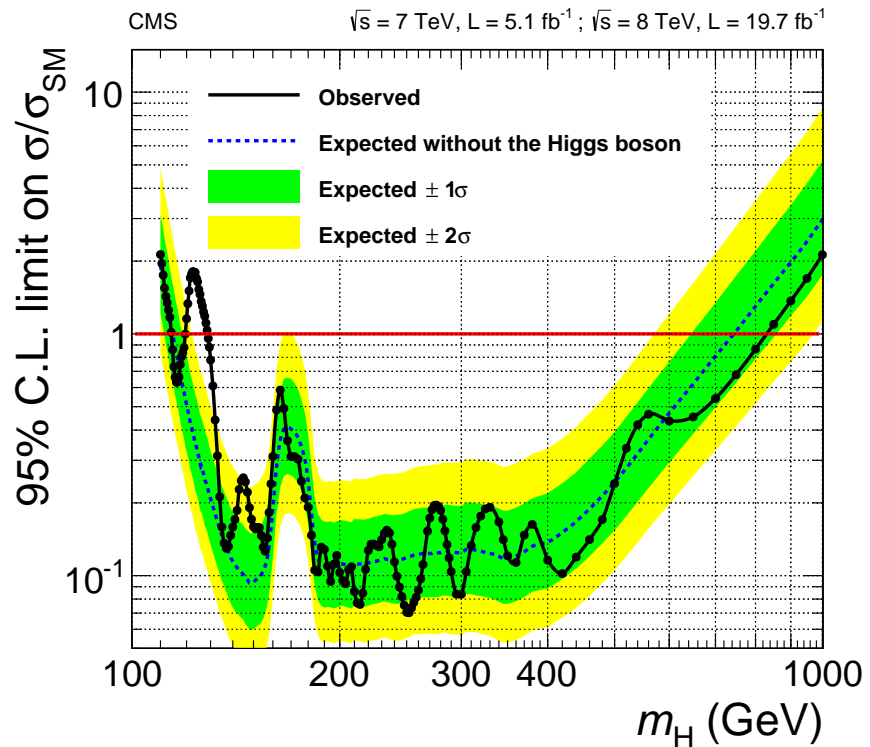


Figure 4.14: Observed and expected 95% C.L. upper limit on the ratio of the production cross section to the SM expectation. The expected $\pm 1\sigma$ and $\pm 2\sigma$ C.L. ranges of expectation for the background-only model are also shown with green and yellow bands, respectively [41].

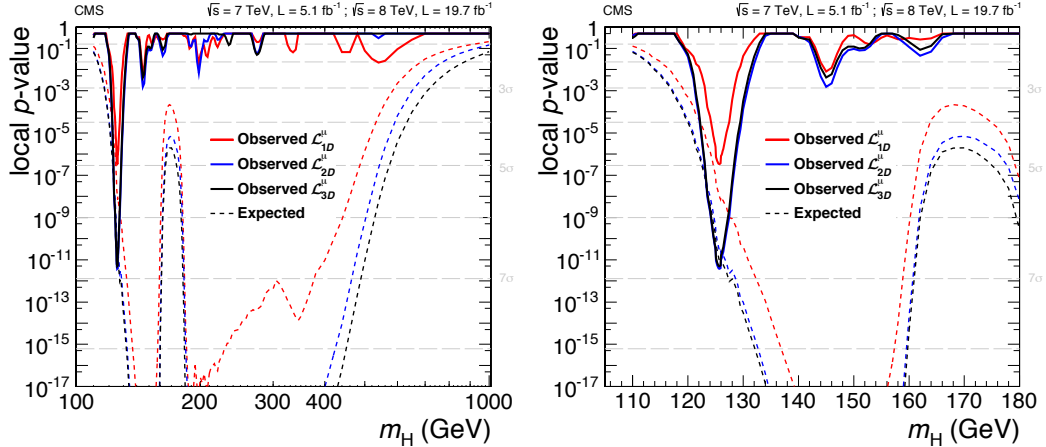


Figure 4.15: (left) Significance of the local excess with respect to the SM background expectation as a function of the Higgs boson mass in the full mass range 110–1000 GeV. Results obtained using the 1D fit, 2D fit, and the nominal 3D fit. (right) Significance of the local excess with respect to the SM background expectation as a function of the Higgs boson mass for the 1D fit, 2D fit, and the nominal 3D fit. Results are shown for the full data sample in the low-mass region only [41].

expected sensitivity to the signal. No other significant deviations with respect to the expectations is found in the mass range 110–1000 GeV. All of these results are consistent with previous CMS and ATLAS publications [66–68], and the second most significant p-value minimum is reached around $m_{4\ell} = 146 \text{ GeV}$, with a local significance of 2.7σ . This computation does not take into account the look-elsewhere effect [121].

As a validation of this thesis work, plots were also made of the signal to background ratio from each of the likelihood models (1D, 2D, 3D). These distributions are shown in figure 4.16 where the background components are given in the filled histograms, the outline provides the expectation for signal, and the observed events are shown

CHAPTER 4. $H \rightarrow ZZ \rightarrow 4\ell$ SEARCH & PRODUCTION/DECAY FRACTIONS

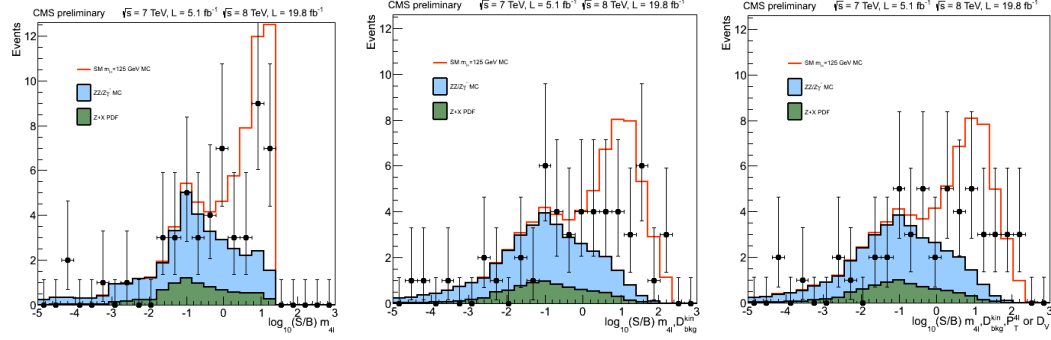


Figure 4.16: Signal to background ratio's for expected and observed events, computed from the 1D (left), 2D (left), and 3D (right) likelihoods. These plots are made from the $m_{4\ell} \in 121.5\text{--}130.5$ GeV region to study the observed peak. The signal used as the Higgs boson hypothesis corresponds to $m_H = 126$ GeV. These plots are preliminary and unpublished.

as data points. A Higgs boson hypothesis of $m_H = 126$ GeV is used and the plots are made from the $m_{4\ell} \in 121.5\text{--}130.5$ GeV region to study the observed peak. One can see that with each additional dimension added to the likelihood the separation between the signal and background increases.

Question (3) asks if the observations we see are consistent with the SM Higgs boson that is predicted. Using the signal strength ($\mu = \sigma/\sigma_{SM}$) we have already defined we can quantify this. If the likelihoods minimize giving $\mu = 1$ then the data is consistent with the Higgs boson. All of these studies are performed at the best fit mass for the Higgs boson using this 4ℓ final state, $m_H = 125.6$ GeV [41]. By fitting the signal expectations we can estimate the sensitivity based on the systematics and statistics currently available. Such a fit of the expected results gives a median expected signal strength of $\mu = 1.00^{+0.31}_{-0.26}$. The fit of the actual data gives

$\mu = 0.93^{+0.26}_{-0.23}(\text{stat.})^{+0.13}_{-0.09}(\text{syst.})$ in very good agreement with the SM Higgs boson expectations. This fit also illuminates that the statistical and systematic uncertainties are of the same order of magnitude, pointing to the need for increased study of systematic uncertainties in future studies.

4.5.2 Search for additional Higgs bosons

Using a preliminary unpublished version of the analysis, where a Higgs boson of $m_H = 126$ GeV is added to the background instead of the signal, this thesis work searched the data in the four-lepton final state for additional bosons that might be observed. In BSM models that have more than one Higgs boson the four-lepton final state may see both of these bosons. In regions far away from the new peak the limits shown in figure 4.14 are valid. Near the peak, we can recreate the likelihoods with the new 126 GeV Higgs background process and perform a search for a second peak (identical to a SM Higgs boson) near or under the observed one. These results can be seen in figure 4.17 where no additional boson is seen. Additionally, the local significance for a (Higgs boson identical) BSM boson is shown and no significant deviation from the background is seen.

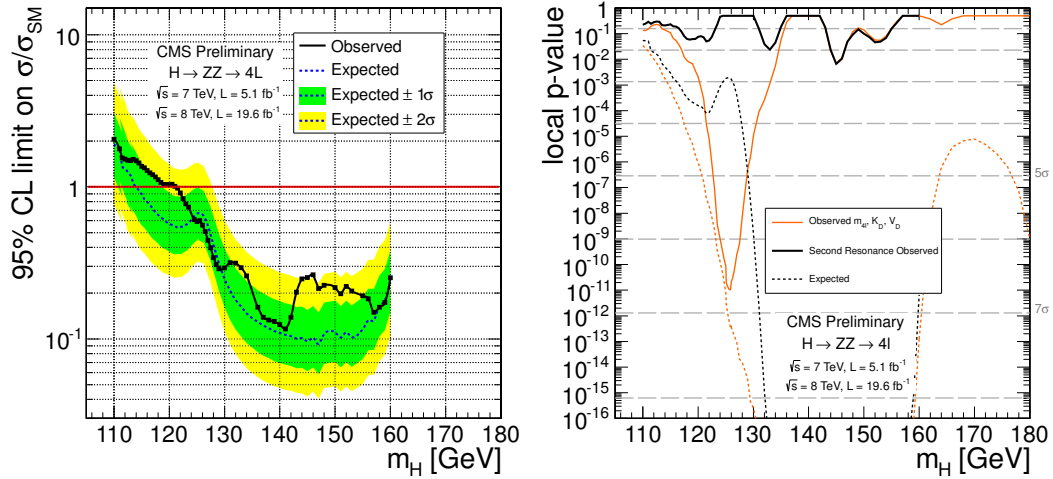


Figure 4.17: (left) Observed and expected 95% C.L. upper limit on the ratio of the production cross section to the SM expectation where a 126 GeV Higgs boson is added as background. The expected $\pm 1\sigma$ and $\pm 2\sigma$ C.L. ranges of expectation for the background-only model are also shown with green and yellow bands, respectively. (right) Significance of the local excess with respect to the SM background + 126 GeV Higgs boson expectation as a function of the BSM Higgs boson mass and compared to the expected and observed significance of the SM Higgs boson. These results were obtained from a preliminary version of the 4ℓ analysis and are unpublished.

4.6 Production & Decay Fraction Results

Looking at the results presented in the previous section, the addition of the $p_T^{4\ell}$ and \mathcal{D}_{jet} shapes don't add too much to the sensitivity of the search. However these distributions allow the three-dimensional likelihood to be sensitive to the production & decay fractions of the Higgs boson.

To investigate these quantities, modified definitions of the signal strength are used. These modified quantities measure the ratio of the interesting cross section times branching ratio to the SM expectation for this value. In this way, $\mu_X = 1$ is the standard model, while a μ_X inconsistent with 1 would be a sign of non-SM behavior.

The decay fraction results are reported in two categories, 0/1-jet and dijet. These results are presented in figure 4.18 (left). The vertical blue line, and green band shows the combined μ fit presented in the last section, while the black points and red horizontal bars indicate the fit of the signal strength in the two individual categories. The result is $\mu_{0/1\text{-jet}} = 0.83^{+0.31}_{-0.25}$ in the 0/1-jet category and $\mu_{\text{dijet}} = 1.45^{+0.89}_{-0.62}$ in the dijet category. for each category, the signal strength is consistent with SM expectations within the uncertainties, which are dominated by statistical uncertainties.

To disentangle the production mechanisms of the observed new state, the production mechanisms are split into two families depending on whether the production is through couplings to fermions (gluon fusion, $t\bar{t}H$) or vector bosons (VBF, VH). For $m_H = 126$ GeV, about 55% of the VBF events are expected to be included in the dijet category, while only 8% of the gluon fusion events are included in the dijet category.

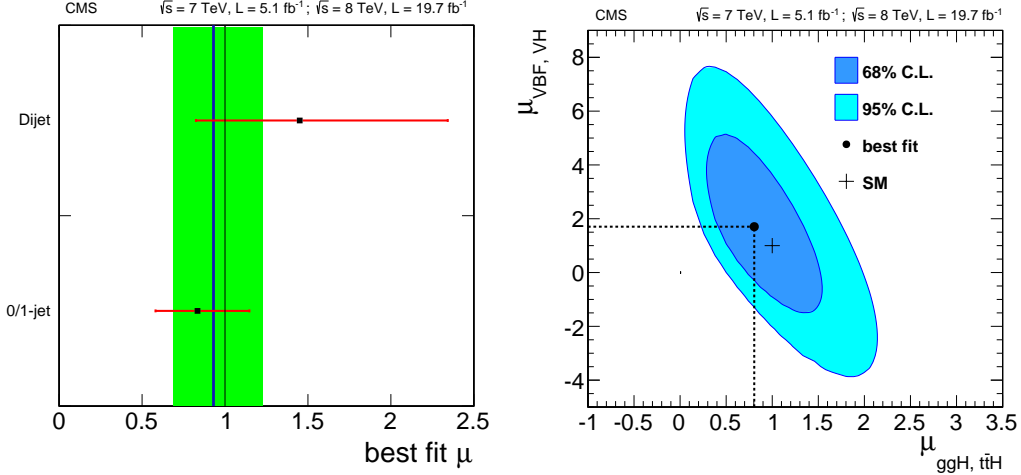


Figure 4.18: (left) Values of μ for the two categories. The vertical line shows the combined μ together with its associated $\pm 1\sigma$ uncertainties, shown as a green band. The horizontal bars indicate the $\pm 1\sigma$ uncertainties in μ for the different categories. The uncertainties include both statistical and systematic sources of uncertainty. (right) Likelihood contours on the signal-strength modifiers associated with fermions ($\mu_{ggH, t\bar{t}H}$) and vector bosons ($\mu_{VBF, VH}$) shown at a 68% and 95% C.L. [41].

As shown in table 4.3, a fraction of 43% of WH and ZH production contributes to the dijet category. Events that contribute are those in which the vector boson decays hadronically.

Two modified signal-strengths ($\mu_{ggH, t\bar{t}H}$ and $\mu_{VBF, VH}$) are introduced as scale factors for the fermion and vector-boson induced contribution to the expected SM cross section. A fit is performed for the two signal-strength modifiers simultaneously, assuming a mass hypothesis of $m_H = 125.6$ GeV. The likelihood is profiled for all nuisance parameters and 68% and 95% C.L. contours in the $(\mu_{ggH, t\bar{t}H}, \mu_{VBF, VH})$ plane are obtained. Figure 4.18 (right) shows the result of the fit leading to the measurements of $\mu_{ggH, t\bar{t}H}$ and $\mu_{VBF, VH}$. The measured values are consistent with the expectations for

CHAPTER 4. $H \rightarrow ZZ \rightarrow 4\ell$ SEARCH & PRODUCTION/DECAY FRACTIONS

the SM Higgs boson, $(\mu_{ggH,t\bar{t}H}, \mu_{VBF,VH}) = (1, 1)$. With the current limited statistics, we cannot establish yet the presence of VBF and VH production, since $\mu_{VBF,VH} = 0$ is also compatible with the data. Since the decay (into ZZ) is vector-boson mediated, it is necessary that such a coupling must exist in the production side and that the SM VBF and SM VH production mechanisms must be present. The fitted value of $\mu_{VBF,VH} = 1.7^{+2.2}_{-2.1}$ is driven partly by the hard \mathcal{D}_{jet} spectrum of the events observed in data when compared to the expectation from the production of the SM Higgs boson (figure 4.11). While the fitted value of $\mu_{ggH,t\bar{t}H} = 0.80^{+0.46}_{-0.36}$ is very close to the SM expectations and dominates the measurement of the total signal strength.

Chapter 5

Conclusions

This is a reference to a previous section: 1

CHAPTER 5. CONCLUSIONS

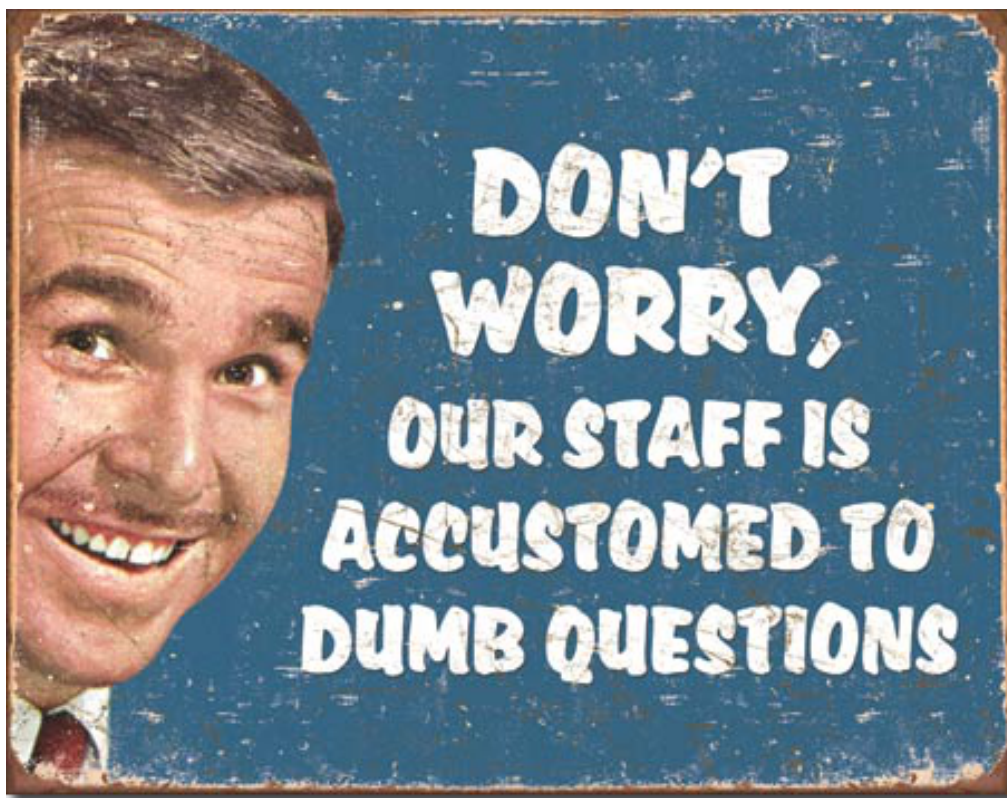


Figure 5.1: This is a sample figure

Bibliography

- [1] E. Noether, “Invariant Variation Problems,” *Gott.Nachr.*, vol. 1918, pp. 235–257, 1918.
- [2] Wikipedia, “Euler angles,” 2015, [Accessed Feb. 9, 2015]. [Online]. Available: http://en.wikipedia.org/wiki/Euler_angles
- [3] M. Maggiore, *A Modern Introduction to Quantum Field Theory*. Oxford University Press, 2005, ch. 5.1.
- [4] F. Schwabl, *Quantum Mechanics*, 3rd ed. Springer, 2002.
- [5] D. P. Hogan, “The Jayhawk Process,” 2007, design for University of Kansas SPS T-shirts.
- [6] S. L. Glashow, “Partial Symmetries of Weak Interactions,” *Nucl. Phys.*, vol. 22, pp. 579–588, 1961.
- [7] S. Weinberg, “A Model of Leptons,” *Phys. Rev. Lett.*, vol. 19, pp. 1264–1266, 1967.

BIBLIOGRAPHY

- [8] A. Salam, “Elementary Particle Physics,” *N. Svartholm ed., Almqvist and Wiksell, Stockholm*, 1968.
- [9] S. L. Glashow, J. Iliopoulos, and L. Maiani, “Weak Interactions with Lepton-Hadron Symmetry,” *Phys. Rev.*, vol. D2, pp. 1285–1292, 1970.
- [10] D. Galbraith and C. Burgard, “UX: Standard Model of the Standard Model,” 2012, CERN Webfest 2012. [Online]. Available: <http://davidgalbraith.org/portfolio/ux-standard-model-of-the-standard-model/>
- [11] R. Aaij *et al.*, “Observation of the resonant character of the $Z(4430)^-$ state,” *Phys. Rev. Lett.*, vol. 112, no. 22, p. 222002, 2014.
- [12] M. A. Armstrong, *Groups and Symmetry*. Springer-Verlag, 1988.
- [13] W. Miller, *Symmetry Groups and their Applications*. Academic Press, Inc., 1972.
- [14] P. Oliver, *Applications of Lie Groups to Differential Equations*, 2nd ed. Springer-Verlag, 1993.
- [15] W. Tung, *Group Theory in Physics*. World Scientific Publishing, 1985.
- [16] D. J. Griffiths, *Introduction to Elementary Particles*. John Wiley & Sons, Inc., 1987, ch. 9 Quantum Chromodynamics.

BIBLIOGRAPHY

- [17] P. W. Higgs, “Broken symmetries, massless particles and gauge fields,” *Phys.Lett.*, vol. 12, pp. 132–133, 1964.
- [18] P. W. Higgs, “Broken Symmetries and the Masses of Gauge Bosons,” *Phys.Rev.Lett.*, vol. 13, pp. 508–509, 1964.
- [19] P. W. Higgs, “Spontaneous Symmetry Breakdown without Massless Bosons,” *Phys.Rev.*, vol. 145, pp. 1156–1163, 1966.
- [20] F. Englert and R. Brout, “Broken Symmetry and the Mass of Gauge Vector Mesons,” *Phys.Rev.Lett.*, vol. 13, pp. 321–322, 1964.
- [21] G. Guralnik, C. Hagen, and T. Kibble, “Global Conservation Laws and Massless Particles,” *Phys.Rev.Lett.*, vol. 13, pp. 585–587, 1964.
- [22] T. Kibble, “Symmetry breaking in nonAbelian gauge theories,” *Phys.Rev.*, vol. 155, pp. 1554–1561, 1967.
- [23] S. Dawson, “Introduction to Electroweak Symmetry Breaking,” *AIP Conf.Proc.*, vol. 1116, pp. 11–34, 2009.
- [24] Wolfram Research, Inc., “Mathematica,” Champaign, Illinois, 2015, Version 10.1.
- [25] M. Maggiore, *A Modern Introduction to Quantum Field Theory*. Oxford University Press, 2005, ch. 11.2.

BIBLIOGRAPHY

- [26] K. Olive *et al.*, “Review of Particle Physics,” *Chin.Phys.*, vol. C38, p. 090001, 2014.
- [27] M. Kobayashi and T. Maskawa, “CP Violation in the Renormalizable Theory of Weak Interaction,” *Prog.Theor.Phys.*, vol. 49, pp. 652–657, 1973.
- [28] O. Klein, “The Atomicity of Electricity as a Quantum Theory Law,” *Nature*, vol. 118, p. 516, 1926.
- [29] S. Weinberg, “The First Three Minutes. A Modern View of the Origin of the Universe,” 1977.
- [30] V. Trimble, “Existence and Nature of Dark Matter in the Universe,” *Ann.Rev.Astron.Astrophys.*, vol. 25, pp. 425–472, 1987.
- [31] Brüning, Oliver Sim and Collier, Paul and Lebrun, P and Myers, Stephen and Ostojic, Ranko and Poole, John and Proudlock, Paul, *LHC Design Report*. Geneva: CERN, 2004. [Online]. Available: <http://cds.cern.ch/record/782076>
- [32] LHC Programme Coordination, “LHC Luminosity Plots for the 2012(2011) Proton Run,” 2011, 2012. [Online]. Available: <http://lpc.web.cern.ch/lpc/>
- [33] O. S. Bruning and P. Collier, “Building a behemoth,” *Nature*, vol. 448, pp. 285–289, 2007.
- [34] Public CMS Luminosity Information, “2012(2011) Proton-Proton Col-

BIBLIOGRAPHY

- lisions, Luminosity versus day,” 2011, 2012. [Online]. Available: <https://twiki.cern.ch/twiki/bin/view/CMSPublic/LumiPublicResults>
- [35] G. L. Bayatian *et al.*, *CMS Physics: Technical Design Report Volume 1: Detector Performance and Software*, ser. Technical Design Report CMS. Geneva: CERN, 2006, there is an error on cover due to a technical problem for some items. [Online]. Available: <https://cds.cern.ch/record/922757>
- [36] T. Sakuma and T. McCauley, “Detector and Event Visualization with SketchUp at the CMS Experiment,” *J.Phys.Conf.Ser.*, vol. 513, p. 022032, 2014.
- [37] S. Chatrchyan *et al.*, “Precise Mapping of the Magnetic Field in the CMS Barrel Yoke using Cosmic Rays,” *JINST*, vol. 5, p. T03021, 2010.
- [38] S. Chatrchyan *et al.*, “Alignment of the CMS tracker with LHC and cosmic ray data,” *JINST*, vol. 9, p. P06009, 2014.
- [39] D. Kotlinski, R. Baur, R. P. Horisberger, R. Schnyder, W. Erdmann, and K. Gabathuler, “Readout of the CMS pixel detector,” *CERN Document Server*, 2000. [Online]. Available: <https://cds.cern.ch/record/478252>
- [40] S. Chatrchyan *et al.*, “The CMS experiment at the CERN LHC. The Compact Muon Solenoid experiment,” *J. Instrum.*, vol. 3, p. S08004. 361 p, 2008, also published by CERN Geneva in 2010. [Online]. Available: <https://cds.cern.ch/record/1129810>

BIBLIOGRAPHY

- [41] S. Chatrchyan *et al.*, “Measurement of the properties of a Higgs boson in the four-lepton final state,” *Phys.Rev.*, vol. D89, no. 9, p. 092007, 2014.
- [42] S. Chatrchyan *et al.*, “Performance of CMS Hadron Calorimeter Timing and Synchronization using Test Beam, Cosmic Ray, and LHC Beam Data,” *JINST*, vol. 5, p. T03013, 2010.
- [43] S. Chatrchyan *et al.*, “Particle-Flow Event Reconstruction in CMS and Performance for Jets, Taus, and MET,” CERN, 2009. Geneva, Tech. Rep. CMS-PAS-PFT-09-001, Apr 2009. [Online]. Available: <https://cds.cern.ch/record/1194487>
- [44] S. Chatrchyan *et al.*, “Electron reconstruction and identification at $\sqrt{s} = 7$ TeV,” CERN, Geneva, Tech. Rep. CMS-PAS-EGM-10-004, 2010. [Online]. Available: <http://cds.cern.ch/record/1299116>
- [45] S. Chatrchyan *et al.*, “Electron performance with 19.6 fb^{-1} of data collected at $\sqrt{s} = 8$ TeV with the CMS detector.” *CERN Document Server*, Mar 2013. [Online]. Available: <http://cds.cern.ch/record/1523273>
- [46] M. Cacciari, G. P. Salam, and G. Soyez, “The Anti- $k(t)$ jet clustering algorithm,” *JHEP*, vol. 0804, p. 063, 2008.
- [47] S. Chatrchyan *et al.*, “Determination of Jet Energy Calibration and Transverse Momentum Resolution in CMS,” *JINST*, vol. 6, p. P11002, 2011.

BIBLIOGRAPHY

- [48] S. Chatrchyan *et al.*, “Alignment of the CMS Silicon Tracker during Commissioning with Cosmic Rays,” *JINST*, vol. 5, p. T03009, 2010.
- [49] V. Blobel and C. Kleinwort, “A New method for the high precision alignment of track detectors,” *eConf*, pp. URL–STR(9), 2002.
- [50] V. Karimaki, T. Lampen, and F. Schilling, “The HIP algorithm for track based alignment and its application to the CMS pixel detector,” *CERN Document Server*, 2006.
- [51] A. Bonato *et al.*, “Application of Survey Measurements in Tracker Alignment,” *CMS Internal Note*, 2009.
- [52] W. Adam *et al.*, “Alignment of the CMS Silicon Strip Tracker during stand-alone Commissioning,” *JINST*, vol. 4, p. T07001, 2009.
- [53] S. Chatrchyan *et al.*, “2012 CMS Tracker Alignment: Performance Plots,” *CERN Document Server*, May 2013. [Online]. Available: <https://cds.cern.ch/record/1552581>
- [54] LHC Higgs Cross Section Working Group, S. Dittmaier, C. Mariotti, G. Passarino, and R. Tanaka (Eds.), “Handbook of LHC Higgs Cross Sections: 1. Inclusive Observables,” *CERN-2011-002*, CERN, Geneva, 2011.
- [55] LHC Higgs Cross Section Working Group, S. Dittmaier, C. Mariotti, G. Passarino, and R. Tanaka (Eds.), “Handbook of LHC Higgs Cross Sections: 2. Production and Decay of Higgs Bosons through Weak Interactions,” *CERN-2011-003*, CERN, Geneva, 2011.

BIBLIOGRAPHY

- sarino, and R. Tanaka (Eds.), “Handbook of LHC Higgs Cross Sections: 2. Differential Distributions,” *CERN-2012-002*, CERN, Geneva, 2012.
- [56] LHC Higgs Cross Section Working Group, S. Heinemeyer, C. Mariotti, G. Passarino, and R. Tanaka (Eds.), “Handbook of LHC Higgs Cross Sections: 3. Higgs Properties,” *CERN-2013-004*, CERN, Geneva, 2013.
- [57] N. Kauer and G. Passarino, “Inadequacy of zero-width approximation for a light Higgs boson signal,” *JHEP*, vol. 1208, p. 116, 2012.
- [58] F. Caola and K. Melnikov, “Constraining the Higgs boson width with ZZ production at the LHC,” *Phys.Rev.*, vol. D88, p. 054024, 2013.
- [59] V. Khachatryan *et al.*, “Constraints on the Higgs boson width from off-shell production and decay to Z-boson pairs,” *Phys.Lett.*, vol. B736, p. 64, 2014.
- [60] I. Anderson, S. Bolognesi, F. Caola, Y. Gao, A. V. Gritsan *et al.*, “Constraining anomalous HVV interactions at proton and lepton colliders,” *Phys.Rev.*, vol. D89, no. 3, p. 035007, 2014.
- [61] V. Khachatryan *et al.*, “Constraints on the spin-parity and anomalous HVV couplings of the Higgs boson in proton collisions at 7 and 8 TeV,” *CERN Document Server*, 2014.
- [62] Y. Gao, A. V. Gritsan, Z. Guo, K. Melnikov, M. Schulze *et al.*, “Spin determi-

BIBLIOGRAPHY

- nation of single-produced resonances at hadron colliders,” *Phys.Rev.*, vol. D81, p. 075022, 2010.
- [63] S. Bolognesi, Y. Gao, A. V. Gritsan, K. Melnikov, M. Schulze *et al.*, “On the spin and parity of a single-produced resonance at the LHC,” *Phys.Rev.*, vol. D86, p. 095031, 2012.
- [64] L. Landau, “On the angular momentum of a two-photon system,” *Dokl.Akad.Nauk Ser.Fiz.*, vol. 60, pp. 207–209, 1948.
- [65] C.-N. Yang, “Selection Rules for the Dematerialization of a Particle Into Two Photons,” *Phys.Rev.*, vol. 77, pp. 242–245, 1950.
- [66] G. Aad *et al.*, “Observation of a new particle in the search for the Standard Model Higgs boson with the ATLAS detector at the LHC,” *Phys.Lett.*, vol. B716, pp. 1–29, 2012.
- [67] S. Chatrchyan *et al.*, “Observation of a new boson at a mass of 125 GeV with the CMS experiment at the LHC,” *Phys.Lett.*, vol. B716, pp. 30–61, 2012.
- [68] S. Chatrchyan *et al.*, “Observation of a new boson with mass near 125 GeV in pp collisions at $\sqrt{s} = 7$ and 8 TeV,” *JHEP*, vol. 1306, p. 081, 2013.
- [69] L. Randall and R. Sundrum, “An Alternative to compactification,” *Phys.Rev.Lett.*, vol. 83, pp. 4690–4693, 1999.

BIBLIOGRAPHY

- [70] L. Randall and R. Sundrum, “A Large mass hierarchy from a small extra dimension,” *Phys.Rev.Lett.*, vol. 83, pp. 3370–3373, 1999.
- [71] K. Agashe, H. Davoudiasl, G. Perez, and A. Soni, “Warped Gravitons at the LHC and Beyond,” *Phys.Rev.*, vol. D76, p. 036006, 2007.
- [72] J. M. Cornwall, D. N. Levin, and G. Tiktopoulos, “Derivation of gauge invariance from high-energy unitarity bounds on the s matrix,” *Phys. Rev. D*, vol. 10, pp. 1145–1167, Aug 1974. [Online]. Available: <http://link.aps.org/doi/10.1103/PhysRevD.10.1145>
- [73] B. W. Lee, C. Quigg, and H. B. Thacker, “Weak interactions at very high energies: The role of the higgs-boson mass,” *Phys. Rev. D*, vol. 16, pp. 1519–1531, Sep 1977. [Online]. Available: <http://link.aps.org/doi/10.1103/PhysRevD.16.1519>
- [74] J. M. Cornwall, D. N. Levin, and G. Tiktopoulos, “Uniqueness of spontaneously broken gauge theories,” *Phys. Rev. Lett.*, vol. 30, pp. 1268–1270, Jun 1973. [Online]. Available: <http://link.aps.org/doi/10.1103/PhysRevLett.30.1268>
- [75] C. L. Smith, “High energy behaviour and gauge symmetry,” *Physics Letters B*, vol. 46, no. 2, pp. 233 – 236, 1973. [Online]. Available: <http://www.sciencedirect.com/science/article/pii/0370269373906928>

BIBLIOGRAPHY

- [76] L. E. W. Group, “Precision Electroweak Measurements and Constraints on the Standard Model,” 2010.
- [77] R. Barate *et al.*, “Search for the standard model Higgs boson at LEP,” *Phys.Lett.*, vol. B565, pp. 61–75, 2003.
- [78] T. Aaltonen *et al.*, “Higgs Boson Studies at the Tevatron,” *Phys.Rev.*, vol. D88, no. 5, p. 052014, 2013.
- [79] T. Aaltonen *et al.*, “Evidence for a particle produced in association with weak bosons and decaying to a bottom-antibottom quark pair in Higgs boson searches at the Tevatron,” *Phys.Rev.Lett.*, vol. 109, p. 071804, 2012.
- [80] M. Cacciari and G. P. Salam, “Pileup subtraction using jet areas,” *Phys.Lett.*, vol. B659, pp. 119–126, 2008.
- [81] M. Cacciari, G. P. Salam, and G. Soyez, “The Catchment Area of Jets,” *JHEP*, vol. 0804, p. 005, 2008.
- [82] P. Nason and C. Oleari, “NLO Higgs boson production via vector-boson fusion matched with shower in POWHEG,” *JHEP*, vol. 1002, p. 037, 2010.
- [83] E. Bagnaschi, G. Degrassi, P. Slavich, and A. Vicini, “Higgs production via gluon fusion in the POWHEG approach in the SM and in the MSSM,” *JHEP*, vol. 1202, p. 088, 2012.

BIBLIOGRAPHY

- [84] S. Frixione, P. Nason, and C. Oleari, “Matching NLO QCD computations with Parton Shower simulations: the POWHEG method,” *JHEP*, vol. 0711, p. 070, 2007.
- [85] T. Sjostrand, S. Mrenna, and P. Z. Skands, “PYTHIA 6.4 Physics and Manual,” *JHEP*, vol. 0605, p. 026, 2006.
- [86] S. Dawson, “Radiative corrections to higgs boson production,” *Nuclear Physics B*, vol. 359, no. 23, pp. 283 – 300, 1991. [Online]. Available: <http://www.sciencedirect.com/science/article/pii/0550321391900612>
- [87] A. Djouadi, M. Spira, and P. Zerwas, “Production of higgs bosons in proton colliders. {QCD} corrections,” *Physics Letters B*, vol. 264, no. 34, pp. 440 – 446, 1991. [Online]. Available: <http://www.sciencedirect.com/science/article/pii/037026939190375Z>
- [88] S. Actis, G. Passarino, C. Sturm, and S. Uccirati, “NLO Electroweak Corrections to Higgs Boson Production at Hadron Colliders,” *Phys.Lett.*, vol. B670, pp. 12–17, 2008.
- [89] S. Catani, D. de Florian, M. Grazzini, and P. Nason, “Soft gluon resummation for Higgs boson production at hadron colliders,” *JHEP*, vol. 0307, p. 028, 2003.
- [90] V. Ravindran, J. Smith, and W. L. van Neerven, “NNLO corrections to the

BIBLIOGRAPHY

- total cross-section for Higgs boson production in hadron hadron collisions,” *Nucl.Phys.*, vol. B665, pp. 325–366, 2003.
- [91] C. Anastasiou and K. Melnikov, “Higgs boson production at hadron colliders in NNLO QCD,” *Nucl.Phys.*, vol. B646, pp. 220–256, 2002.
- [92] R. V. Harlander and W. B. Kilgore, “Next-to-next-to-leading order Higgs production at hadron colliders,” *Phys.Rev.Lett.*, vol. 88, p. 201801, 2002.
- [93] M. Spira, A. Djouadi, D. Graudenz, and P. Zerwas, “Higgs boson production at the LHC,” *Nucl.Phys.*, vol. B453, pp. 17–82, 1995.
- [94] J. Baglio and A. Djouadi, “Higgs production at the IHC,” *JHEP*, vol. 1103, p. 055, 2011.
- [95] C. Anastasiou, R. Boughezal, and F. Petriello, “Mixed QCD-electroweak corrections to Higgs boson production in gluon fusion,” *JHEP*, vol. 0904, p. 003, 2009.
- [96] D. de Florian, G. Ferrera, M. Grazzini, and D. Tommasini, “Higgs boson production at the LHC: transverse momentum resummation effects in the H- γ 2gamma, H- γ WW- γ lnu lnu and H- γ ZZ- γ 4l decay modes,” *JHEP*, vol. 1206, p. 132, 2012.
- [97] M. Ciccolini, A. Denner, and S. Dittmaier, “Strong and electroweak correc-

BIBLIOGRAPHY

- tions to the production of Higgs + 2jets via weak interactions at the LHC,” *Phys.Rev.Lett.*, vol. 99, p. 161803, 2007.
- [98] M. Ciccolini, A. Denner, and S. Dittmaier, “Electroweak and QCD corrections to Higgs production via vector-boson fusion at the LHC,” *Phys.Rev.*, vol. D77, p. 013002, 2008.
- [99] T. Figy, C. Oleari, and D. Zeppenfeld, “Next-to-leading order jet distributions for Higgs boson production via weak boson fusion,” *Phys.Rev.*, vol. D68, p. 073005, 2003.
- [100] K. Arnold, M. Bahr, G. Bozzi, F. Campanario, C. Englert *et al.*, “VBFNLO: A Parton level Monte Carlo for processes with electroweak bosons,” *Comput.Phys.Commun.*, vol. 180, pp. 1661–1670, 2009.
- [101] P. Bolzoni, F. Maltoni, S.-O. Moch, and M. Zaro, “Higgs production via vector-boson fusion at NNLO in QCD,” *Phys.Rev.Lett.*, vol. 105, p. 011801, 2010.
- [102] T. Melia, P. Nason, R. Rontsch, and G. Zanderighi, “W+W-, WZ and ZZ production in the POWHEG BOX,” *JHEP*, vol. 1111, p. 078, 2011.
- [103] T. Binoth, N. Kauer, and P. Mertsch, “Gluon-induced QCD corrections to $\pi^- \pi^+ ZZ \rightarrow l^- l^+ l'^- l'^+$,” p. 142, 2008.
- [104] J. M. Campbell, R. K. Ellis, and C. Williams, “Vector boson pair production at the LHC,” *JHEP*, vol. 1107, p. 018, 2011.

BIBLIOGRAPHY

- [105] J. M. Campbell and R. K. Ellis, “An Update on vector boson pair production at hadron colliders,” *Phys.Rev.*, vol. D60, p. 113006, 1999.
- [106] J. M. Campbell and R. Ellis, “MCFM for the Tevatron and the LHC,” *Nucl.Phys.Proc.Suppl.*, vol. 205-206, pp. 10–15, 2010.
- [107] J. Alwall, P. Demin, S. de Visscher, R. Frederix, M. Herquet *et al.*, “MadGraph/MadEvent v4: The New Web Generation,” *JHEP*, vol. 0709, p. 028, 2007.
- [108] H.-L. Lai, J. Huston, Z. Li, P. Nadolsky, J. Pumplin *et al.*, “Uncertainty induced by QCD coupling in the CTEQ global analysis of parton distributions,” *Phys.Rev.*, vol. D82, p. 054021, 2010.
- [109] H.-L. Lai, M. Guzzi, J. Huston, Z. Li, P. M. Nadolsky *et al.*, “New parton distributions for collider physics,” *Phys.Rev.*, vol. D82, p. 074024, 2010.
- [110] S. Agostinelli, J. Allison, K. Amako, J. Apostolakis, H. Araujo, P. Arce, M. Asai, D. Axen, S. Banerjee, G. Barrand, F. Behner, L. Bellagamba, J. Boudreau, L. Broglia, A. Brunengo, H. Burkhardt, S. Chauvie, J. Chuma, R. Chytracek, G. Cooperman, G. Cosmo, P. Degtyarenko, A. Dell’Acqua, G. Depaola, D. Dietrich, R. Enami, A. Feliciello, C. Ferguson, H. Fesefeldt, G. Folger, F. Foppiano, A. Forti, S. Garelli, S. Giani, R. Giannitrapani, D. Gibin, J. G. Cadenas, I. Gonzlez, G. G. Abril, G. Greeniaus, W. Greiner, V. Grichine, A. Grossheim, S. Guatelli, P. Gumplinger, R. Hamatsu,

BIBLIOGRAPHY

K. Hashimoto, H. Hasui, A. Heikkinen, A. Howard, V. Ivanchenko, A. Johnson, F. Jones, J. Kallenbach, N. Kanaya, M. Kawabata, Y. Kawabata, M. Kawaguti, S. Kelner, P. Kent, A. Kimura, T. Kodama, R. Kokoulin, M. Kossov, H. Kurashige, E. Lamanna, T. Lampn, V. Lara, V. Lefebure, F. Lei, M. Liendl, W. Lockman, F. Longo, S. Magni, M. Maire, E. Medernach, K. Minamimoto, P. M. de Freitas, Y. Morita, K. Murakami, M. Nagamatu, R. Nartallo, P. Nieminen, T. Nishimura, K. Ohtsubo, M. Okamura, S. O’Neale, Y. Oohata, K. Paech, J. Perl, A. Pfeiffer, M. Pia, F. Ranjard, A. Rybin, S. Sadilov, E. D. Salvo, G. Santin, T. Sasaki, N. Savvas, Y. Sawada, S. Scherer, S. Sei, V. Sirotenko, D. Smith, N. Starkov, H. Stoecker, J. Sulkimo, M. Takahata, S. Tanaka, E. Tcherniaev, E. S. Tehrani, M. Tropeano, P. Truscott, H. Uno, L. Urban, P. Urban, M. Verderi, A. Walkden, W. Wander, H. Weber, J. Wellisch, T. Wenaus, D. Williams, D. Wright, T. Yamada, H. Yoshida, and D. Zschiesche, “Geant4-a simulation toolkit,” *Nuclear Instruments and Methods in Physics Research Section A: Accelerators, Spectrometers, Detectors and Associated Equipment*, vol. 506, no. 3, pp. 250 – 303, 2003. [Online]. Available: <http://www.sciencedirect.com/science/article/pii/S0168900203013688>

[111] J. Allison, K. Amako, J. Apostolakis, H. Araujo, P. Dubois *et al.*, “Geant4 developments and applications,” *IEEE Trans.Nucl.Sci.*, vol. 53, p. 270, 2006.

[112] G. Passarino, C. Sturm, and S. Uccirati, “Higgs Pseudo-Observables, Second

BIBLIOGRAPHY

- Riemann Sheet and All That,” *Nucl.Phys.*, vol. B834, pp. 77–115, 2010.
- [113] S. Goria, G. Passarino, and D. Rosco, “The Higgs Boson Lineshape,” *Nucl.Phys.*, vol. B864, pp. 530–579, 2012.
- [114] N. Cabibbo and A. Maksymowicz, “Angular correlations in K_{e4} decays and determination of low-energy $\pi - \pi$ phase shifts,” *Phys. Rev.*, vol. 168, pp. 1926–1926, Apr 1968. [Online]. Available: <http://link.aps.org/doi/10.1103/PhysRev.168.1926>
- [115] S. Chatrchyan *et al.*, “Study of the Mass and Spin-Parity of the Higgs Boson Candidate Via Its Decays to Z Boson Pairs,” *Phys.Rev.Lett.*, vol. 110, no. 8, p. 081803, 2013.
- [116] “Absolute Calibration of Luminosity Measurement at CMS: Summer 2011 Update,” CERN, Geneva, Tech. Rep. CMS-PAS-EWK-11-001, 2011. [Online]. Available: <http://cds.cern.ch/record/1376102>
- [117] “CMS Luminosity Based on Pixel Cluster Counting - Summer 2013 Update,” CERN, Geneva, Tech. Rep. CMS-PAS-LUM-13-001, 2013. [Online]. Available: <http://cds.cern.ch/record/1598864>
- [118] A. Denner, S. Heinemeyer, I. Puljak, D. Rebuzzi, and M. Spira, “Standard Model Higgs-Boson Branching Ratios with Uncertainties,” *Eur.Phys.J.*, vol. C71, p. 1753, 2011.

BIBLIOGRAPHY

- [119] T. Junk, “Confidence level computation for combining searches with small statistics,” *Nucl.Instrum.Meth.*, vol. A434, pp. 435–443, 1999.
- [120] A. L. Read, “Presentation of search results: The CL(s) technique,” *J.Phys.*, vol. G28, pp. 2693–2704, 2002.
- [121] E. Gross and O. Vitells, “Trial factors or the look elsewhere effect in high energy physics,” *Eur.Phys.J.*, vol. C70, pp. 525–530, 2010.

Vita